TÉCNICO
LISBOA

Twisted bilayer graphene — electronic and optical properties

Gonçalo Filipe Santos Catarina

Thesis to obtain the Master of Science Degree in

Engineering Physics

Supervisors: Prof. Eduardo Filipe Vieira de Castro
Prof. Nuno Miguel Machado Reis Peres

Examination Committee

Chairperson: Prof. Pedro Domingos Santos do Sacramento
Supervisor: Prof. Eduardo Filipe Vieira de Castro
Member of the Committee: Prof. Pedro José Gonçalves Ribeiro

February 2017

To my beloved grandmother, Mariana Braizinha

Acknowledgments

First and foremost, I thank my father, António Catarina, and my grandmother, Mariana Braizinha, for the value they gave to my education. They made an absolute priority that I could pursue my aspirations and that is something for which I will always be grateful and indebted.

From my friends, I appreciate all the support, especially the endless patience and the confidence placed in me over the last 5 years.

I thank prof. João Viana for the helpful discussions and Eduardo Dias for providing me the images from figures 1.6 and 3.10, along with the respective interpretations.

I acknowledge the help of my friend Maria Beira in reading and reviewing my thesis. I am also thankful to my friends Christopher Alves and Pedro Marreiro for helping me with my image editing needs.

Last, but not least, I thank my supervisors, prof. Eduardo Castro and prof. Nuno Peres, for their notable guidance and availability.

Resumo

O estudo das propriedades das heteroestruturas de van der Waals é um tópico de investigação recente em física da matéria condensada, com enorme potencial [1–3] mas ainda numa fase inicial. Nesta dissertação, o foco está na descrição teórica de um dos amontoamentos mais simples, a bicamada de grafeno rodada, que pode ser vista como um dos constituintes fundamentais em empilhamentos mais complexos.

Começa-se por reproduzir uma teoria a uma partícula, baseada num modelo contínuo de baixa energia, para os estados eletrónicos deste material; a determinação dos perfis da densidade de estados e da densidade de portadores de carga segue-se imediatamente. Depois, prossegue-se para o estudo das propriedades óticas, nomeadamente a condutividade ótica (no contexto da teoria da resposta linear) e o espectro dos plasmões-polaritões de superfície no grafeno (usando um tratamento semi-clássico). Por fim, os efeitos das interações eletrão-eletrão são investigados, em particular o termo corretivo de auto-energia para a renormalização das bandas devido ao potencial repulsivo de Coulomb de longo alcance (blindado).

Neste trabalho, alcançou-se um profundo entendimento dos mais recentes modelos efetivos semi-analíticos e das suas particularidades. Quanto aos cálculos da condutividade ótica, verificou-se que os resultados são compatíveis com a literatura e discutiram-se ainda as implementações numéricas, introduzindo-se um novo método eficaz para calcular a condutividade de Drude. Obtiveram-se também resultados originais para a resposta plasmónica deste sistema. Relativamente aos efeitos das interações eletrão-eletrão, embora não se tenha conseguido preencher esta lacuna na literatura, apresentou-se uma discussão sobre como abordar, em trabalhos futuros, as dificuldades encontradas.

Palavras-chave: bicamada de grafeno rodada, modelo contínuo de baixa energia, condutividade ótica, plasmões-polaritões de superfície, auto-energia.

Abstract

The study of the properties of van der Waals heterostructures is a new trending research field in condensed matter physics, with huge potential [1–3] but still in an early stage. In this thesis, we focus on the theoretical description of one of the simplest stackings, the twisted bilayer graphene, which can be seen as one of the fundamental pieces for more complex assemblies.

We reproduce a single-particle theory, based on a low-energy continuum model, for the electronic states in this material; the profile determination of the density of states and the carrier density follows directly. Then, we proceed with the study of the optical properties, namely the optical conductivity (within the linear response theory) and the spectrum of graphene surface plasmon-polaritons (using a semi-classical treatment). Lastly, we address the effects of electron-electron interactions, in particular the self-energy correction term for the band renormalization due to the long range (screened) Coulomb repulsion.

In this work, a profound understanding of the most recent semi-analytical effective models and their features was attained. As for the optical conductivity calculations, our results were compatible with the literature and we also discussed the numerical implementations, introducing a new and improved method for computing the Drude conductivity. Original results for the plasmonic response of this system were achieved. Regarding the electron-electron interaction effects, although we could not fulfill this gap in the literature, we believe we have provided a useful discussion on how to tackle the difficulties in future works.

Keywords: twisted bilayer graphene, low-energy continuum model, optical conductivity, surface plasmon-polaritons, self-energy.

Contents

List of Tables

List of Figures

Nomenclature

Abbreviations

DFT	Density functional theory.
dFT	Discrete Fourier transform.
FT	Fourier transform.
h.c.	Hermitian conjugate.
HF	Hartree-Fock.
IdFT	Inverse discrete Fourier transform.
KK	Kramers-Kronig.
MF	Mean field.
NN	Nearest neighbor(s).
PBC	Periodic boundary conditions.
QED	Quantum electrodynamics.
RPA	Random phase approximation.
TF	Thomas-Fermi.

Physical constants

$\hbar$	Reduced Planck constant. $\hbar \simeq 1.055 \times 10^{-34}\mathrm{m}^2\,\mathrm{kg}\,\mathrm{s}^{-1}$ (SI) $\simeq 6.582 \times 10^{-16}\mathrm{eV}\,\mathrm{s}$.
σ_0	Graphene universal conductivity. $\sigma_0 = e^2/(4\hbar)$.
ε_0	Vacuum permittivity. $\varepsilon_0 \simeq 8.854 \times 10^{-12}\mathrm{F}\,\mathrm{m}^{-1}$ (SI) $\simeq 1.419 \times 10^{-30}\mathrm{C}^2\,\mathrm{eV}^{-1}\,\mathrm{m}^{-1}$.
c	Speed of light. $c \simeq 2.998 \times 10^{8}\mathrm{m}\,\mathrm{s}^{-1}$ (SI).
e	Elementary charge. $e \simeq 1.602 \times 10^{-19}\mathrm{C}$ (SI).

k_B	Boltzmann constant. $k_B \simeq 1.381 \times 10^{-23} \mathrm{m}^2\,\mathrm{kg}\,\mathrm{s}^{-2}\,\mathrm{K}^{-1}$ (SI) $\simeq 8.617 \times 10^{-5} \mathrm{eV}\,\mathrm{K}^{-1}$.

Mathematical operators

$[A, B]$	Commutator.
$\delta(x-a)$	Dirac delta function.
$\delta_{i,j}$	Kronecker delta.
$\mathcal{T}$	Time-ordering operator.
Θ	Heaviside step function.
*	Complex conjugate.
†	Hermitian conjugate (conjugate transpose).
P	Cauchy principal value.

Relevant variables

μ	Fermi level.
ω	Angular frequency.
σ_{ij}^{D}	Drude conductivity tensor.
σ_{ij}^{reg}	Regular conductivity tensor.
σ_{ij}	Conductivity tensor.
θ	Twist angle.
ε^r	Relative permittivity.
D_{ij}	Drude weight tensor.
DOS	Density of states.
f	Frequency.
n	Carrier density (positive for electrons and negative for holes).
T	Absolute temperature.

Glossary

BLG	Bilayer graphene (BLG) is the physical system composed of two graphene sheets on top of each other, with no particular arrangement specified.
BZ	A Brillouin zone (BZ) is a Wigner-Seitz primitive cell in reciprocal space.
DOS	The density of states (DOS) of a system describes the number of states per interval of energy at each energy level that are available to be occupied.
GSPPs	Graphene surface plasmon-polaritons (GSPPs) are SPPs in which graphene is the 2D surface.
SLG	Single layer graphene (SLG) is the physical system composed of one single sheet of graphene only.
SPPs	Surface plasmon-polaritons (SPPs) are collective plasma oscillations, coupled to photons, which propagate in a 2D surface.
SPs	Surface plasmons (SPs) are collective plasma oscillations which propagate in a 2D surface.
TE	In the context of electromagnetic radiation, a transverse electric (TE) mode designates a waveguide where there is no electric field in the direction of propagation.

TM	In the context of electromagnetic radiation, a transverse magnetic (TM) mode designates a waveguide where there is no magnetic field in the direction of propagation.
mSL	Moiré superlattice (mSL) is the emergent large-scale (quasi)periodic structure appearing in tBLG systems.
tBLG	The twisted bilayer graphene (tBLG) is a particular arrangement of a BLG, characterized by a twist angle between the top and the bottom layers.
vdW heterostructure	A van der Waals (vdW) heterostructure is an artificial 3D material made by stacking 2D crystals together.

Chapter 1

Introduction

1.1 Framework and motivation

The developments in materials science are intimately related to technological progress: when a new material with unusual properties is discovered/synthesized, its applicabilities are deeply explored and major technological breakthroughs may hopefully follow. Both experimentalists and theorists have important and complementary roles in the whole process: on the one hand, these new materials need to be synthesized and tested in the laboratory by experimentalists, so that they can ultimately be available for practical purposes; on the other hand, a theoretical description of the unusual features of these new materials is of interest, whether for their quantitative description and consequent understanding of reality or to predict new emerging properties which, then, need to be tested and confirmed in the laboratory.

Two-dimensional (2D) crystals are recent examples of promising new materials, graphene being just the most known example of this large class. Having as principal feature their low dimensionality, these 2D crystals present unique physical properties that already have many technological applications. The continuous refinement and optimization of their manufacturing processes and decreasing production costs are responsible for an increasing impact in industry and are expected to lead these crystals to be more and more present in our lives.

Taking into account that the current fabrication methods of 2D crystals are sufficiently well established (at least for some of them), a new trend in modern materials science is to develop novel three-dimensional (3D) materials by controlled multi-stacking of these 2D structures. The variety of possible heterostructures generated, often referred to as van der Waals (vdW), seems to be practically unlimited but, at the same time, their behavior is expected to be hard to predict due to the huge complexity of each 2D structure involved. Therefore, in order to come up with tailored heterostructures, one is required to have a complete understanding of each of the 2D material properties and their mutual interactions when stacked together. Moreover, since these vdW heterostructures are still very hard to produce experimentally, efforts are only made when a particular heterostructure proves to be really worthy of attention.

In this dissertation, we focus on one of the simplest stackings, the twisted bilayer graphene (tBLG) —a graphene sheet on top of other graphene sheet, with a twist angle. We investigate, in a theoretical frame, the spectrum reconstruction, the optical response and the effect of electron-electron interactions. The motivation follows that, by understanding and modeling the properties of this stacking, we are taking a step into the ultimate goal of understanding and predicting the behavior of arbitrary vdW heterostructures, which will, in principle, allow us to come up with new revolutionary tailored materials. This, allied with the intrinsic desire of a physicist to describe nature, even when the technological potential is not very appealing (which is certainly not the case), motivated all the work that was done in this dissertation.

1.2 State of the art

1.2.1 The rise of graphene and other 2D crystals

Dimension matters! And physicists are very well aware of this. In fact, although it seems, at first sight, that for natural phenomena we are stuck with three spatial dimensions plus one time dimension, physicists have been idealizing, for many years, systems with just two spatial dimensions and the results have been remarkable. For example, layered semiconductors with finite thickness (typically around 10-100 atomic layers) have been accurately described as 2D because of quantum size effects that make the degrees of freedom for electron motion in the short direction irrelevant; indeed, every computer chip today relies on this description, particularly in the properties of the electronic flatland at the interface between silicon and its oxide [4].

2D crystals were already known as integral parts of 3D crystalline structures. However, it took a long time to successfully isolate an ultimate one atom thick flatland for the first time. Indeed, to some extent, monolayers were presumed not to exist without a 3D base due to a divergent contribution of thermal fluctuations in these low-dimensional structures [5–7]. Only in 2004, a research group at the University of Manchester, led by Andre Geim and Konstantin Novoselov, reported for the first time stable “free-standing atomic crystals that are strickly 2D and can be viewed as individual atomic planes pulled out of bulk crystals” [8] —figure (fig.) 1.1(A). For this and other contributions to this field, they were awarded with the Nobel Prize in Physics 2010. The reason why their discovery does not contradict the thermal fluctuation arguments is complex, but, in short, it is related to the fact that 2D crystals are embedded in 3D space, so that they can deform into the third, out-of-plane direction [9, 10].

Since 2004, several experimental procedures have been introduced for synthesizing 2D crystals. This includes mechanical exfoliation, chemical exfoliation and epitaxial growth by thermal decomposition of SiC or by chemical vapor deposition of hydrocarbons on catalytic metallic surfaces [11]. The original one —mechanical exfoliation— is currently refined to the level of art, such that single-layered graphite crystallites isolated this way can be obtained commercially nowadays. This procedure takes advantage of the fact that we are actually surrounded by 2D materials. For example, in a simple trace of pencil there are debris composed mostly of readily visible thick graphite flakes rubbed from the bulk crystal. Yet, thinner, nearly transparent, crystallites —some a single layer thick— are also present: typically, in 1cm^2 of graphite debris, there are already few micron-sized graphene crystallites [4]. Roughly speaking, mechanical exfoliation consists in repeatedly peeling debris of 3D layered structure crystals with adhesive

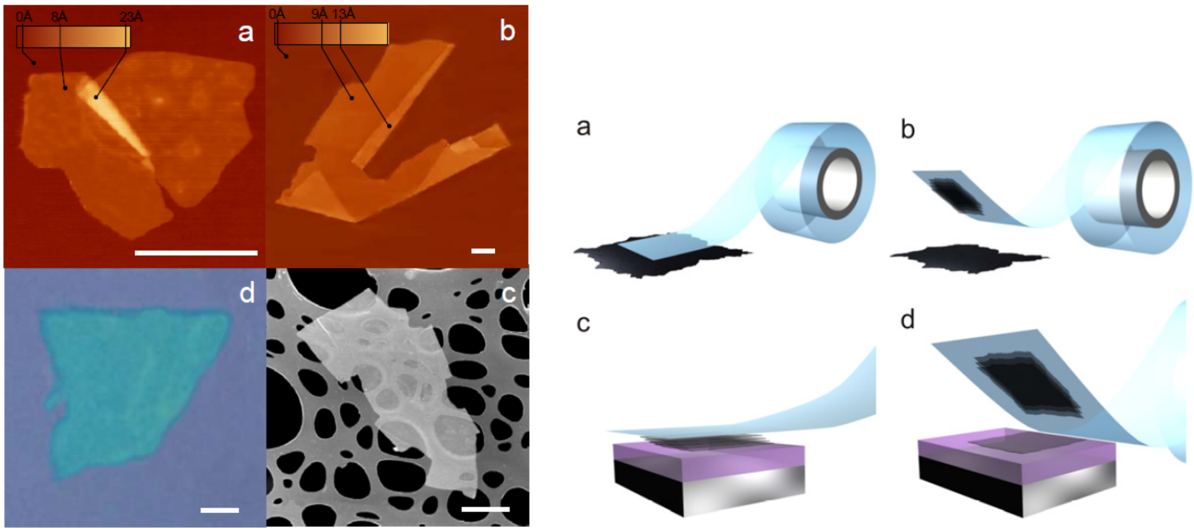

(A) (B)

Figure 1.1: (A) 2D crystal matter. Single layer crystallites of (a) NbSe$_2$, (b) graphite, (c) Bi$_2$Sr$_2$CaCu$_2$O$_X$ and (d) MoS$_2$ visualized by atomic force microscopy (a,b), scanning electron microscopy (c) and in an optical microscope (d). All scale bars are 1µm. Source: reference (ref.) [8]. (B) Mechanical exfoliation of 2D crystals: (a) adhesive tape is pressed against the thin debris of a 3D layered structure crystal, so that the top few layers stay attached to the tape (b); (c) after repeatedly peeling the tape against itself, the part of the tape with the thinnest crystals of layered material is pressed against a surface of choice; (d) upon peeling off, the bottom layer is left on the substrate, ready for microscope inspections. Source: ref. [11].

tape until finding the thinnest flakes (fig. 1.1(B)). The hard part is to find them. The required atomic resolution is attained with atomic-force and scanning-tunneling microscopes, but scanning the entire area of debris with atomic resolution is not viable. Manchester's group managed to find the thinnest flakes by using an oxidized Si wafer as the surface on which the tape is pressed against. This oxide surface reflects a rainbow of colors and the interference pattern produced by the monolayers on the oxide was fortunately shown to provide a faint but visible contrast in rapid optical microscope inspections. This way, atomic resolution is used only after identifying probable 2D crystallites with this faster method.

Nowadays, there is a vast library of existent 2D crystals (fig. 1.2). Amongst them, graphene is an unequivocal champion, exhibiting outstanding properties that have attracted widespread interest from the scientific community all over the world. In fact, it is actually very hard to keep track of all the developments made within this topic in the past few years, even for experienced researchers. So, here, we indicate some refs. [10, 12–15] and give just a brief insight of some of those properties which have triggered so much attention in a wide variety of scientific areas:

- Graphene is a gapless semiconductor: in its band spectrum, the conduction and valence band edges touch. This absence of gap makes this type of materials highly sensitive to external stimuli and adds value to the industry of electronic devices.
- In a quantum mechanical treatment, graphene's electrons follow a Dirac-like equation of motion in the limit of zero rest mass. Thus, graphene provides a way of investigating quantum electrodynamics (QED) phenomena in a benchtop experiment, bringing together issues from both condensed matter and particle physics.

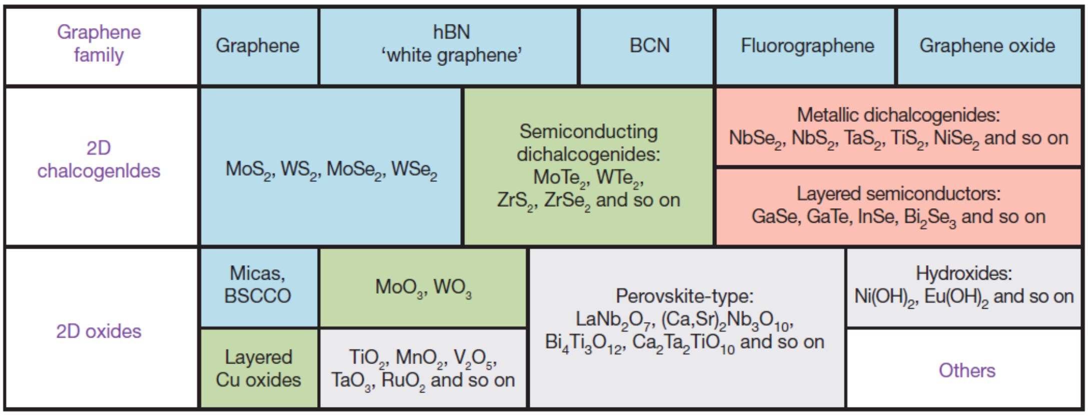

Graphene family	Graphene hBN 'white graphene'	BCN	Fluorographene	Graphene oxide
2D chalcogenides	MoS_2, WS_2, $MoSe_2$, WSe_2	Semiconducting dichalcogenides: $MoTe_2$, WTe_2, ZrS_2, $ZrSe_2$ and so on	Metallic dichalcogenides: $NbSe_2$, NbS_2, TaS_2, TiS_2, $NiSe_2$ and so on Layered semiconductors: GaSe, GaTe, InSe, Bi_2Se_3 and so on	
2D oxides	Micas, BSCCO Layered Cu oxides	MoO_3, WO_3 TiO_2, MnO_2, V_2O_5, TaO_3, RuO_2 and so on	Perovskite-type: $LaNb_2O_7$, $(Ca,Sr)_2Nb_3O_{10}$, $Bi_4Ti_3O_{12}$, $Ca_2Ta_2TiO_{10}$ and so on	Hydroxides: $Ni(OH)_2$, $Eu(OH)_2$ and so on Others

Figure 1.2: Current 2D library: monolayers proved to be stable under ambient conditions are shaded blue; those probably stable are shaded green; the ones unstable in air but that may be stable in inert atmosphere are shaded pink; grey shading indicates 3D compounds that have been successfully exfoliated down to monolayers but for which there is little further information. Source: ref. [1].

- Electron mobility in graphene is remarkable: even at room temperature and in atomically rough substrates, graphene exhibits astonishing electron quality with its electrons covering significant areas with little scattering (this is the Klein paradox —a counterintuitive QED phenomena— in action in graphene).

- Mechanically, graphene is the strongest material ever tested. Experimental measurements (breaking strenght of $\sim 40\mathrm{N\,m}^{-2}$) revealed that graphene is more than 100 times stronger than the strongest steel. As curiosity, the Nobel announcement illustrated this property by stating that a $1\mathrm{m}^2$ graphene hammock would support a 4kg cat but would weigh only as much as one of the cat's whiskers, at 0.77mg (about 0.001% of the weight of $1\mathrm{m}^2$ of paper).

- Chemical modifications in graphene sheets are often explored, in order to put in evidence more pronounced and distinct properties. As an example, graphene-based ultra molecular filters have been designed with an experimental procedure that involves inducing artificial deffects in the sheet (with a gallium ion beam bombardment) and exposing them to adequate etching solutions to ensure that the deffects convert into pores with the desired dimensions.

At the date, most developments in graphene are still at a R&D (research and development) stage, though there is already some market for semiconductor electronics, energy (mainly batteries) and composite material industries. According to a 2015 graphene market report [16], graphene market reached about 20 million dollars in 2014 and is predicted to grow to over 200 million by 2026.

1.2.2 Van der Waals heterostructures — a new trending research field

In parallel with the efforts being made on graphene and other 2D materials, another research field has recently emerged; it deals with vdW heterostructures —artificial structures made by stacking 2D crystals on top of each other (fig. 1.3). The basic principle is simple: we stack monolayers in a chosen sequence, as in building with Lego, and develop artificial materials composed of blocks defined with one-atomic-plane precision; strong covalent bonds provide in-plane stability of 2D crystals, whereas relatively weak

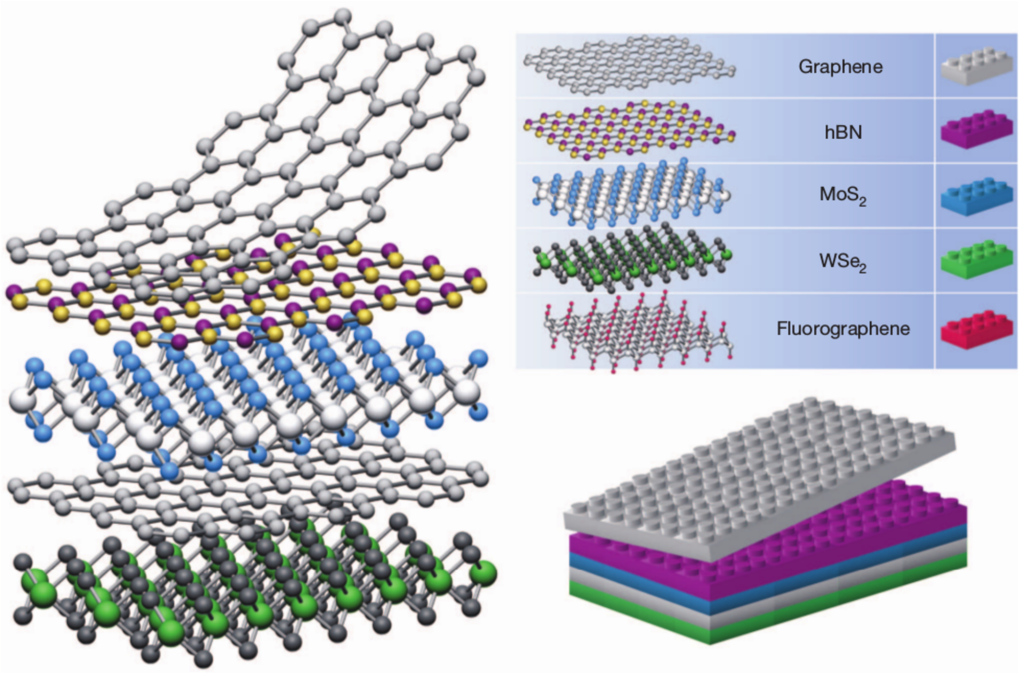

Figure 1.3: Illustration of a vdW heterostructure. Source: ref. [1].

van-der-Waals-like forces are hopefully sufficient to keep the stack together. With the already existing variety of 2D materials presenting unique properties, the aim is to design artificial heterostructures that exhibit tailored properties for technological applications; the real advantage of this approach is that one should be able to synthesize materials that can perform several functions simultaneously. Although this field is still very recent, vdW heterostructures clearly do not lack ambition.

Given the vast library of 2D crystals available, one should be expecting a countless number of possible stacking combinations. However, only few of these assemblies really work. Firstly, as mentioned, not all 2D crystals are stable under the same conditions, so we can't explore all the possible combinations. Secondly, the complexity of these heterostructures is huge, leading many times to unpredictable failures. At the date, only few groups have reported vdW heterostructures made from more than two atomically thin crystals, and only graphene and few-layer BN, MoS_2 and WS_2 were used for those assemblies [1]. A typical stacking procedure [1, 2] starts by isolating micrometer-sized 2D crystals on top of a thin transparent film (a polymer, for example). The resulting 2D crystal can then be put face down onto a chosen target. Finally, the supporting film is removed or dissolved and this process is repeated again and again until the desired stack is assembled. Conceptually, the procedure is simple to understand and requires only basic facilities such as a good optical microscope. In pratice, however, this is still very hard to master, mainly due to contamination effects between the layers. In fig. 1.4, we present the state of the art of the experimental developments: a vdW heterostructure made from six alternating bilayers of graphene and BN —the largest reported so far.

At the moment, this field is still deeply unexplored and potential applications are yet speculative. However, little evolutionary steps with graphene-BN and graphene-graphene heterostructures have been published (a review of some of them can be seen in ref. [1]), making these ones the most appealing for

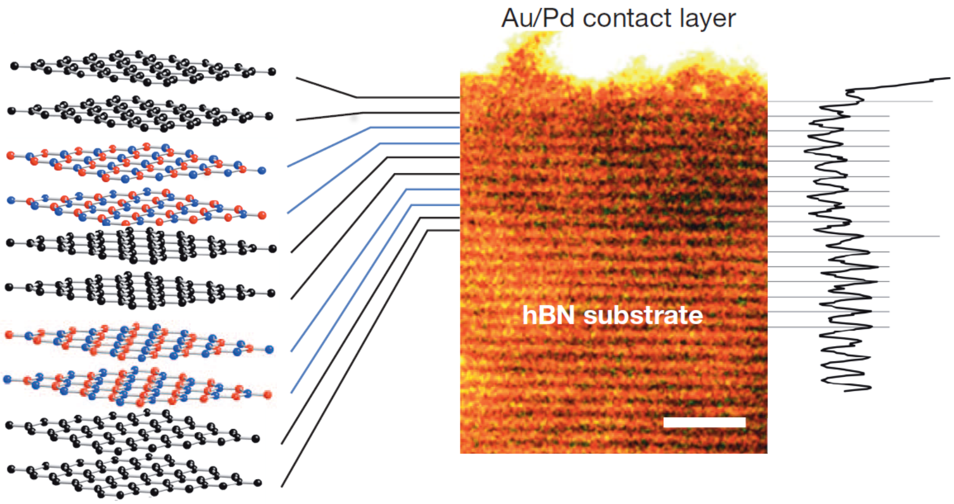

Figure 1.4: Graphene-BN structure consisting of six stacked bilayers: on the left side it is represented a schematic view of the layer sequence; on the right, its cross-section and intensity profile seen by scanning transmission electron microscopy are shown. Scale bar is 2nm. Source: ref. [1].

investigation nowadays. The expectations are that this field should develop into a large field of its own, as was the case for graphene.

1.2.3 Overview on twisted bilayer graphene breakthroughs

In this section, we intend to give a brief review, without going into too much detail, on the latest developments made within tBLG systems. We mainly focus on the theoretical work, since that is the tone of this thesis, but we also try to motivate, as much as possible, the interest regarding its applications and/or promising features. Within this scope, we highlight the work done by Rozhkov et al. [17], which serves as a foundation for the whole section. This recent review paper starts with an introduction to the basics of the single layer graphene (SLG) system and then moves into the bilayers. From the three types of bilayer graphene (BLG) stackings discussed —AA, AB/Bernal and tBLG—, the tBLG is referred to as the most intricate and open to investigation, which leads to a separate discussion of the most commonly studied topics. From those, we address here the ones which are somehow related with the work done in this dissertation. When discussing the particular topic of graphene plasmonics, we also highlight two main references on which we have based our overview: the review paper by Luo et al. [18] and the book by Gonçalves and Peres [19].

Models

The complex geometry of the tBLG affects significantly its electronic properties, making even the single-particle models quite involved. Before moving onto a review of these models, we thus devote some attention to the crystal structure of tBLG systems. The twist angle, θ, between one graphene layer with respect to the other manifests itself in the appearance of a moiré pattern, which can be visualized experimentally (fig. 1.5). This pattern reveals a periodicity (or quasiperiodicity) of the crystal structure, which we call moiré superlattice (mSL). While the moiré exists for any θ, the superstructure,

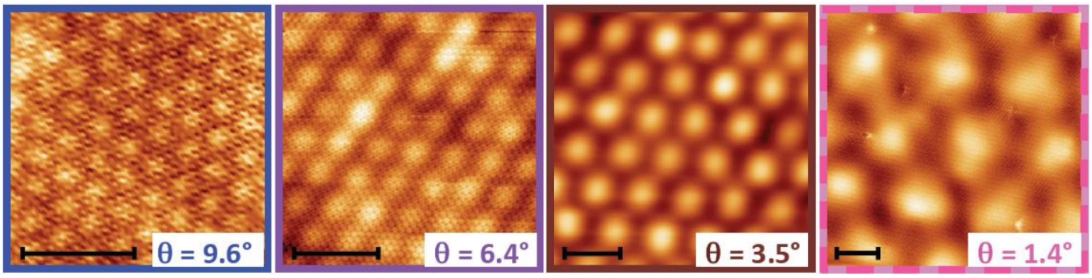

Figure 1.5: Scanning tunneling microscope images of tBLG moiré patterns. All scale bars are 5nm. Source: ref. [21].

that is, strickly periodic repetition of some large multiatomic supercell, occurs only for the so-called commensurate angles. The commensurability relation is given by [20]

$$\cos(\theta) = \frac{3m^2 + 3mr + r^2/2}{3m^2 + 3mr + r^2}, \quad 0^\circ < \theta < 30^\circ \,, \tag{1.1}$$

where m and r are coprime positive integers.

For commensurate structures, numerical studies based on density functional theory (DFT) have been performed [22–24]. However, since the unit cell of the tBLG superlattice contains a large number of sites, especially at small θ, these *ab initio* calculations incur a significant computational cost and are therefore rather unpractical. To avoid this difficulty, semi-analytical theories have been developed in order to describe the low-energy electronic properties of the tBLG. These theories operate mainly on the electronic states near the Dirac cones in a way that the Hamiltonian construction is accomplished by considering Dirac electrons moving in each layer and hybridized by interlayer hopping. The first low-energy theory was proposed by Lopes dos Santos et al. [25], and further developed in ref. [20]. A similar treatment based on a continuum approximation was done by Bistritzer and MacDonald [26]. The construction of this model is slightly different in the sense that it is valid for arbitrary twist angles and not necessarily commensurate ones; therefore, although the approach is very similar, the starting point of this work is more general because there is no geometrical impositions required. In ref. [27], the authors made further simplifications to these low-energy Hamiltonians and derived a simple effective 2×2 Hamiltonian, from which analytical expressions for the electronic spectrum can be obtained. Recently, Weckbecker et al. [28] introduced a model which is identical to that derived by Bistritzer and MacDonald, but with a rescaling in the coupling momentum scale, in better agreement with tight-binding *ab initio* calculations.

Although there is a lot of work based on single-electron theories, papers studying the effects of electron-electron interactions in tBLG are still absent.

Optical response

In general, the study of light-matter interactions is a topic of interest in science, with a wide variety of applications, for example in the field of photonics. For graphene, and in particular for the tBLG system, the response to an applied electromagnetic field is characterized by the optical conductivity, which has been measured experimentally [29–31]. Within the theoretical framework, we highlight the

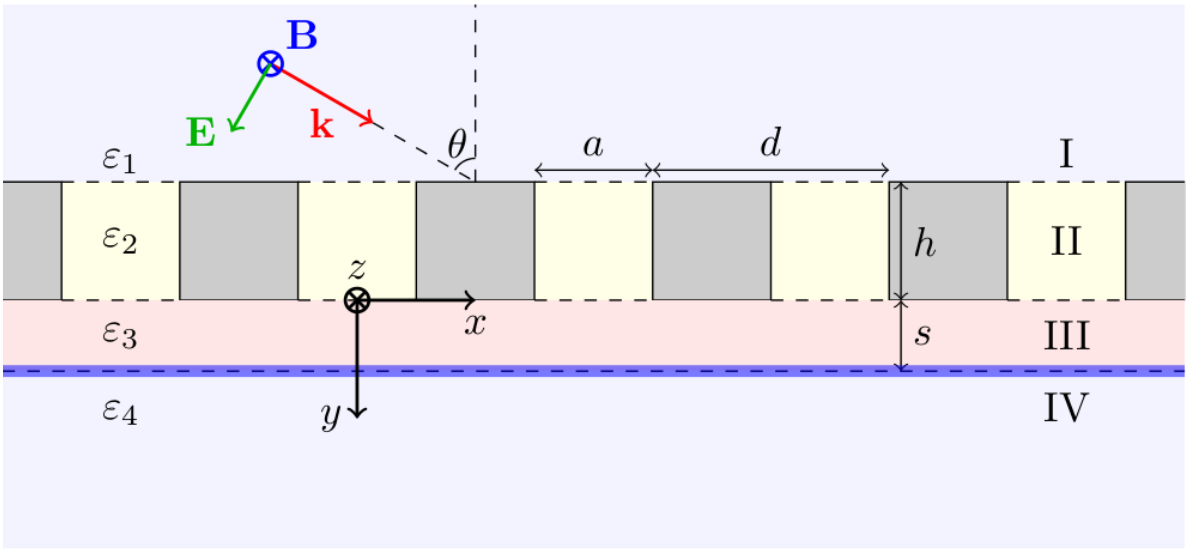

Figure 1.6: Representation of the experimental setup for exciting GSPPs (side view): graphene (blue line) is located between two dielectric media (III and IV), with a periodic grid of graphene micro-ribbons placed on top; the polarized light is shinned from the outside (medium I). Image kindly provided by Eduardo Dias.

following works: Tabert and Nicol [32] used the simplified model from ref. [27] to compute the dynamical (frequency dependent) conductivity at different levels of the chemical potential; tight-binding *ab intio* calculations of the dynamical conductivity were performed by Moon and Koshino [33]; the real and imaginary parts of the dynamical conductivity were calculated by Stauber et al. [34] using a continuum low-energy models based on refs. [25, 26].

Over the last few years, graphene plasmonics has emerged as a new research topic, especially after the experimental realization achieved by the end of 2011, when Ju et al. [35] showed the possibility of exciting graphene surface plasmon-polaritons (GSPPs) in the THz spectral range by shinning electromagnetic radiation onto a periodic grid of graphene micro-ribbons (fig. 1.6); in short, the idea is that the periodic grid provides the momentum which the light lacks for exciting the plasmons. For a complete historical review on the developments following this work, we recommend the reading of sections 1.2 and 7.1 from ref. [19]. Owing to the 2D nature of the collective excitations, surface plasmons (SPs) excited in graphene are confined much more strongly than those in conventional metals (particularly in the THz spectral range), leading it to be a promising alternative in future applications [18, 36, 37]. In addition, perhaps the most important advantage of using graphene is the tunability of the SPs, since carrier densities in graphene can be easily controlled by electrical gating and doping [35, 38–40]. SPs in graphene can also be coupled with photons, leading to the so-called surface plasmon-polaritons (SPPs), which have been observed recently [41, 42]. As we will see, in the semi-classical model, the dispersion relation of these SPPs in graphene depends explicitly on the optical conductivity, wherefore the study of their spectrum follows as a direct application of what we have discussed in the previous paragprah. Within the theoretical framework, using the knowlegde of both the real and imaginary parts of the dynamical conductivity, Stauber et al. [34] were the first to study the plasmon excitation spectrum in tBLG, which is a topic that is still in its infancy.

1.3 Objectives

The primary objective is to obtain a theoretical description for the tBLG, investigating its electronic spectrum, optical response and the effect of electron-electron interactions. In order to achieve this goal, the work was divided into the following parts:

1) Brief revision of the tight-binding model for a SLG. Initiation into the treatment of bilayers, namely by studying the simplest system of BLG, the Bernal stacking.
2) Spectrum reconstruction, within a low-energy continuum model, of tBLG systems.
3) Density of states (DOS) and carrier density profiles determination.
4) Calculation of the optical conductivity (real and imaginary parts).
5) Computation of reflectance, transmittance and absorption.
6) Plasmonic spectrum obtention.
7) Study of electron-electron interaction effects. In particular, the computation of the exchange energy correction to the band structure and the investigation of magnetic instabilities are in the plan of work.

1.4 Thesis Outline

The dissertation is organized as follows: in chapter 2, we begin with the introduction of basic concepts related to the theoretical description of graphene systems and then we derive a low-energy effective model for the tBLG, which is the starting point for the remaining work. In chapter 3, we compute the optical conductivity within the linear response theory and apply this result to the study of the spectrum of GSPPs. Chapter 4 contains a discussion on the effects of electron-electron interactions, in particular the band renormalization. Finally, in chapter 5, we present our main conclusions and proposals for future work. Additionally, we provide auxiliar derivations in the appendixes.

Chapter 2

Low-energy continuum model

In this chapter, we aim at deriving a model for the tBLG system. As starting point, we explain the tight-binding model for SLG, which allow us to introduce general concepts and fix notation. Within the SLG system, we also look into the folded description, since it will provide us a better understanding of the tBLG system. Then, we move to the bilayers. We begin with a particular stacking of BLG, the Bernal stacking, and treat that simpler system first. At last, we study the arbitrary arrangement of BLG, the tBLG. We follow the work done by Bistritzer and MacDonald [26], and construct a continuum low-energy effective Hamiltonian, which is valid for twist angles $\theta \lesssim 10^\circ$ and independent of the structure being commensurate or incommensurate.

2.1 Single layer graphene basics

2.1.1 Geometry

A SLG is a 2D layer made out of carbon atoms arranged into a honeycomb structure. We choose the coordinate system depicted in fig. 2.1 and define the following hexagonal lattice which describes the possible positions for the unit cells of this system:

$$\boldsymbol{R}_{n_1,n_2} = n_1\boldsymbol{a}_1 + n_2\boldsymbol{a}_2, \quad n_1, n_2 \in \mathbb{Z}, \tag{2.1}$$

in which the primitive vectors $\boldsymbol{a}_1$ and $\boldsymbol{a}_2$ are given by

$$\boldsymbol{a}_1 = \left(1/2, \sqrt{3}/2\right) d_{hex}, \quad \boldsymbol{a}_2 = \left(-1/2, \sqrt{3}/2\right) d_{hex}, \tag{2.2}$$

and their length, d_{hex}, is easily shown to be related to the carbon-carbon distance, d, by $d_{hex} = \sqrt{3}d$. Without loss of generality, we set the dimension of our physical system such that

$$n_i = 0, 1, ..., N_i - 1. \tag{2.3}$$

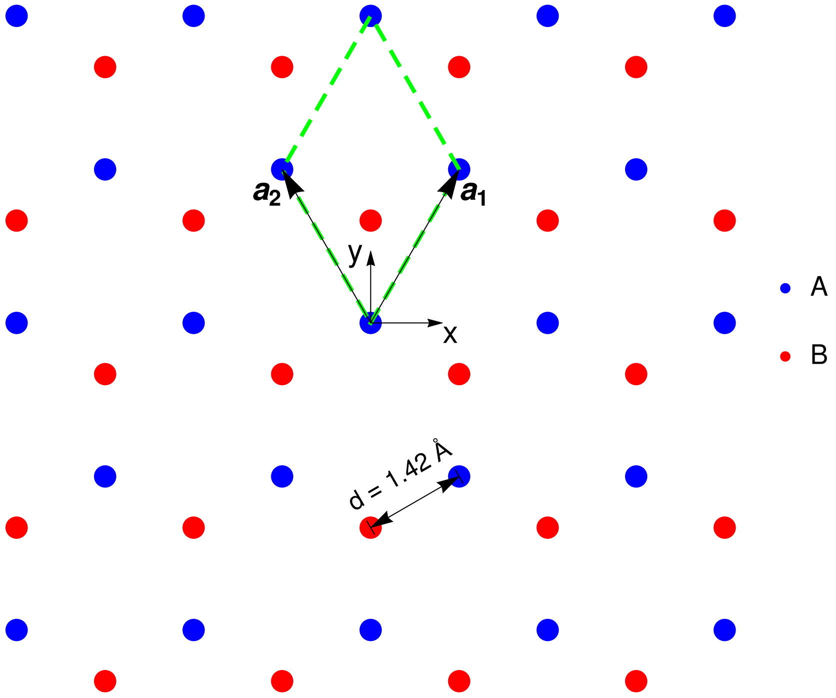

Figure 2.1: SLG geometry. The honeycomb structure can be seen as two interpenetrating hexagonal lattices, A (blue) and B (red). Its experimental structure parameter, the carbon-carbon distance, is $d = 1.42$Å [4]. The dashed green line marks a unit cell of this system, which contains 2 atoms. The coordinate system is centered at a carbon of sublattice A.

2.1.2 Tight-binding model

We intend to describe the physical properties of a SLG. In this material, each carbon has 4 valence electrons, 3 of them localized in covalent bonds between 2 carbon atoms and forming the so-called sp_2 hybrids. The remaining electron is delocalized in a p_z orbital. Most physical properties can be obtained taking into consideration only these delocalized electrons, typically in a tight-binding approximation with hopping between first neighbors. This is the model we shall adopt and detail.

According to Bloch's theorem, the wave function for an electron in a periodic crystal has the form of a Bloch wave,

$$\psi_{\boldsymbol{k}}(\boldsymbol{r}) = e^{i\boldsymbol{k}.\boldsymbol{r}} u_{\boldsymbol{k}}(\boldsymbol{r}), \tag{2.4}$$

where $\boldsymbol{r}$ is the position, $\boldsymbol{k}$ the wave vector and u a periodic function with the same periodicity of the crystal, i.e.,

$$u_{\boldsymbol{k}}(\boldsymbol{r}) = u_{\boldsymbol{k}}(\boldsymbol{r} + \boldsymbol{R}), \tag{2.5}$$

for all crystal lattice vectors $\boldsymbol{R}$. From now on, we will generally refer to $\boldsymbol{k}$ as momentum, due to de Broglie's relation, $\boldsymbol{p} = \hbar\boldsymbol{k}$, which relates the crystal momentum $\boldsymbol{p}$ to the wave vector $\boldsymbol{k}$ by the reduced Planck constant $\hbar$. Combining the previous equations, we obtain an equivalent statement of Bloch's theorem,

$$\psi_{\boldsymbol{k}}(\boldsymbol{r} + \boldsymbol{R}) = e^{i\boldsymbol{k}.\boldsymbol{R}} \psi_{\boldsymbol{k}}(\boldsymbol{r}). \tag{2.6}$$

In the tight-binding approximation, we write the solution of the time-independent single-electron Schrödinger equation as a linear combination of orthonormal atomic orbitals. Using the bra-ket notation, the time-independent single-particle Schrödinger equation reads

$$H\left|\psi\right\rangle = E\left|\psi\right\rangle, \tag{2.7}$$

where H is the time-independent Hamiltonian of the system, which acts on the state $|\psi\rangle$, and E its energy. For the SLG system, we use plane waves as the coefficients in the linear combination and write

$$\left|\psi_{\boldsymbol{k},\alpha}\right\rangle = \frac{1}{\sqrt{N_1 N_2}} \sum_{n_1,n_2} e^{i\boldsymbol{k}\cdot(\boldsymbol{R}_{n_1,n_2}+\boldsymbol{\delta}_\alpha)} \left|\boldsymbol{R}_{n_1,n_2}+\boldsymbol{\delta}_\alpha, \alpha\right\rangle, \tag{2.8}$$

where $|\boldsymbol{R}, \alpha\rangle$ is the ket corresponding to an atomic orbital in position $\boldsymbol{R}$ and sublattice $\alpha = A, B$ and $\boldsymbol{\delta}_\alpha$ is the vector that links the origin of the unit cell to its respective sublattice α atom,

$$\boldsymbol{\delta}_A = \boldsymbol{0}, \quad \boldsymbol{\delta}_B = \boldsymbol{\delta} = (0, d). \tag{2.9}$$

With this choice of normalization, the (approximate) orthonormality of the atomic orbitals (written with the help of the following Kronecker delta functions),

$$\langle \boldsymbol{R}_{n_1,n_2}+\boldsymbol{\delta}_\alpha, \alpha | \boldsymbol{R}_{n_1',n_2'}+\boldsymbol{\delta}_\beta, \beta\rangle = \delta_{n_1,n_1'}\delta_{n_2,n_2'}\delta_{\alpha,\beta}, \tag{2.10}$$

implies orthonormality for the wave functions,

$$\langle \psi_{\boldsymbol{k},\alpha} | \psi_{\boldsymbol{k'},\beta}\rangle = \delta_{\boldsymbol{k},\boldsymbol{k'}}\delta_{\alpha,\beta}, \tag{2.11}$$

as it should be. Moreover, equation (eq.) (2.8) respects Bloch's theorem. Finally, since we have 2 atoms per unit cell, the total wave function should be written as

$$\left|\psi_{\boldsymbol{k}}\right\rangle = \sum_\alpha c_\alpha(\boldsymbol{k}) \left|\psi_{\boldsymbol{k},\alpha}\right\rangle, \tag{2.12}$$

where $c_\alpha(\boldsymbol{k})$ is a complex constant of unit modulus. Note that there is some arbitrariness in these expressions since we can change the phase in (2.8) and include it in the complex constant in (2.12). This corresponds to a change of basis. For convenience, we will stick to this convention.

Assuming an homogeneous nonzero hopping term, $-t$, only between nearest neighbors (NN), which takes into account the possibility of an electron being tranferred ("hopping") from an atom to its NN, and a diagonal term, ϵ_{p_z}, reflecting the atomic energy of an electron in the p_z orbital in the absence of any other nuclei, the tight-binding model yields the following non-null matrix elements:

$$\langle \boldsymbol{R}_{n_1,n_2}, A| H \left|\boldsymbol{R}_{n_1,n_2}+\boldsymbol{\delta}+\boldsymbol{\delta}_{NN}, B\right\rangle = -t, \tag{2.13}$$

$$\langle \boldsymbol{R}_{n_1,n_2}+\boldsymbol{\delta}_\alpha, \alpha| H \left|\boldsymbol{R}_{n_1,n_2}+\boldsymbol{\delta}_\alpha, \alpha\right\rangle = \epsilon_{p_z}, \tag{2.14}$$

where $\boldsymbol{\delta}_{NN}$ are the vectors that, for any carbon of sublattice A, connect its NN from sublattice B,

$$\boldsymbol{\delta}_{NN} = \mathbf{0}, -\boldsymbol{a}_1, -\boldsymbol{a}_2. \tag{2.15}$$

In order to obtain the electronic spectrum, we use the Schrödinger equation (2.7) for the states (2.12) and apply the bras $\langle \boldsymbol{R}_{n_1,n_2}, A|$ and $\langle \boldsymbol{R}_{n_1,n_2} + \boldsymbol{\delta}, B|$ so that we end up with a closed system of equations that we conveniently write in a matrix form,

$$\begin{bmatrix} \epsilon_{p_z} & -tf(\boldsymbol{k}) \\ -tf^*(\boldsymbol{k}) & \epsilon_{p_z} \end{bmatrix} \begin{bmatrix} c_A(\boldsymbol{k}) \\ c_B(\boldsymbol{k}) \end{bmatrix} = E \begin{bmatrix} c_A(\boldsymbol{k}) \\ c_B(\boldsymbol{k}) \end{bmatrix}, \tag{2.16}$$

where

$$f(\boldsymbol{k}) = e^{i\boldsymbol{k}.\boldsymbol{\delta}}(1 + e^{-i\boldsymbol{k}.\boldsymbol{a}_1} + e^{-i\boldsymbol{k}.\boldsymbol{a}_2}) \tag{2.17}$$

and * stands for complex conjugate. In (2.16), we recognize the Hamiltonian matrix. After redefining the zero energy such that it coincides with ϵ_{p_z}, we get

$$H(\boldsymbol{k}) = \begin{bmatrix} 0 & -tf(\boldsymbol{k}) \\ -tf^*(\boldsymbol{k}) & 0 \end{bmatrix}, \tag{2.18}$$

with eigenvalues (energies)

$$E(\boldsymbol{k}) = \pm t \sqrt{4\cos\left(\frac{\sqrt{3}}{2} dk_x\right)\cos\left(\frac{3}{2} dk_y\right) + 2\cos\left(\sqrt{3}\, dk_x\right) + 3}\,. \tag{2.19}$$

As every physical Hamiltonians, (2.18) is hermitian, i.e., $H = H^\dagger$ († stands for hermitian conjugate) and thus has real eigenvalues.

2.1.3 Reciprocal space

Let us take a look into the features of our $\boldsymbol{k}$-space (fig. 2.2(a)). Given the (direct/real space) lattice (2.1), we can define the corresponding reciprocal lattice,

$$\boldsymbol{G}_{m_1,m_2} = m_1\boldsymbol{b}_1 + m_2\boldsymbol{b}_2, \quad m_1, m_2 \in \mathbb{Z}, \tag{2.20}$$

where the reciprocal primitive vectors $\boldsymbol{b}_1$ and $\boldsymbol{b}_2$ obey, by definition, the relation

$$\boldsymbol{a}_i.\boldsymbol{b}_j = 2\pi\delta_{i,j}. \tag{2.21}$$

This leads to

$$\boldsymbol{b}_1 = \left(\sqrt{3}/2, 1/2\right)\frac{4\pi}{3d}, \quad \boldsymbol{b}_2 = \left(-\sqrt{3}/2, 1/2\right)\frac{4\pi}{3d}. \tag{2.22}$$

The concept of periodicity in real space thus extends to momentum space in a way that we need a single BZ to completely characterize the behavior of a Bloch wave in a crystal; in other words, physical waves

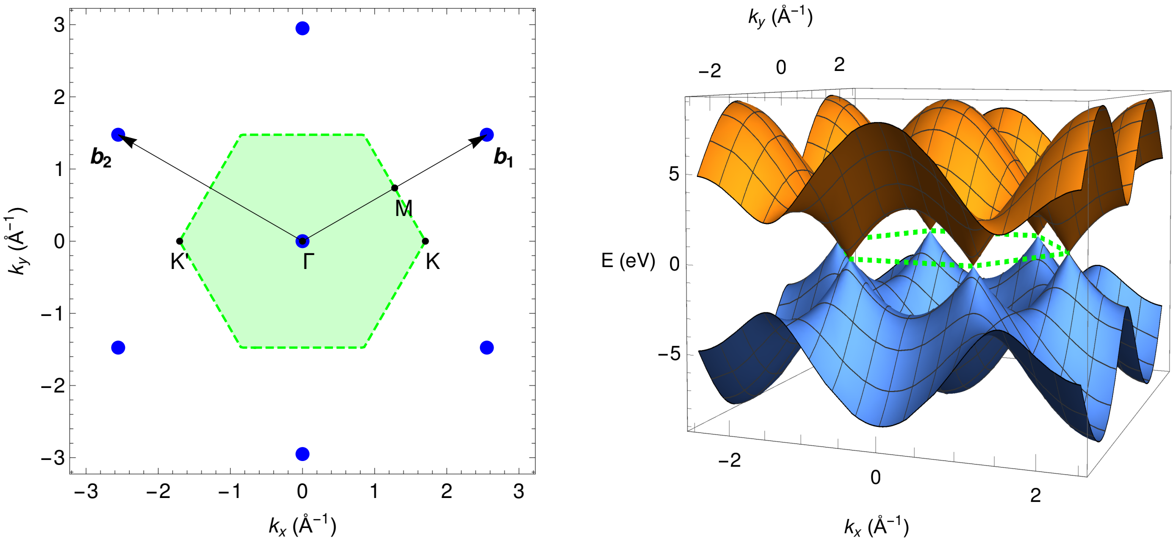

(a) Reciprocal space (b) Electronic spectrum

Figure 2.2: (a) The blue circles represent points in the reciprocal lattice; just like the direct lattice, the reciprocal one is also hexagonal, though rotated and with a different lattice parameter. The green primitive unit cell marks the first Brillouin zone (BZ); some relevant points are plotted in it: $\Gamma = (0,0)$, $M = \left(1, 1/\sqrt{3}\right) \frac{\pi}{d_{hex}}$, $K = (\frac{4\pi}{3d_{hex}}, 0)$, $K' = -K$. (b) The tight-binding parameter was set as $t = 2.97$eV, in agreement with first-principles calculations [10, 43]. The green dashed line marks the first BZ boundaries.

in crystals remain unchanged if their wave vector is shifted by a reciprocal lattice vector, i.e., $\boldsymbol{k} \rightarrow \boldsymbol{k} + \boldsymbol{G}$.

The electronic spectrum, determined in (2.19), is plotted in fig. 2.2(b), where we can explicitly observe this reciprocal space periodicity.

2.1.4 Dirac Hamiltonian

From the whole spectrum (fig. 2.2(b)), we are mainly interested in the low energy range, since that is the regime we can easily access experimentally. This regime is found near the first BZ corners [1]. We choose the two nonequivalent corners K and $K' = -K$ (all others can be reached by adding reciprocal lattice vectors to the former ones) and make a Taylor series expansion of the Hamiltonian (2.18) around them, obtaining, to the first nonvanishing order,

$$H(\boldsymbol{q}) = \hbar v_F \begin{bmatrix} 0 & \pm q_x - i q_y \\ \pm q_x + i q_y & 0 \end{bmatrix} = \pm \hbar v_F \boldsymbol{\sigma} . \boldsymbol{q}, \tag{2.23}$$

where the Fermi velocity, v_F, is identified as $v_F = \frac{3dt}{2\hbar}$, $\boldsymbol{\sigma}$ are the Pauli matrices and $\boldsymbol{k} = \pm K + \boldsymbol{q}$ for small $\boldsymbol{q}$ in this expansion. This low-energy Hamiltonian is recognized as a (massless) Dirac-like Hamiltonian; K and K' are thus called nonequivalent Dirac points.

---

[1] In neutral graphene, we have 1 valence electron, per carbon atom, contributing to the electronic structure. Also, we know that we have as many bands, λ, as atoms in the unit cell and that every state $E_\lambda(\boldsymbol{k})$ gets filled with 2 electrons, due to spin degeneracy. Therefore, the neutral configuration corresponds to the situation where half of the bands are filled, by increasing order of energy. We then see that this half-filling situation is attained at the first BZ corners. In this case, it also corresponds to $E = 0$, but we stress that this is not always necessarily true.

2.1.5 Folded Hamiltonian

It is worth to introduce an equivalent Hamiltonian description for a folded BZ. We start by noticing that, although we have chosen the lattice (2.1), we can opt for larger ones, as long as they still capture the system's periodicity. As we shall see, the simplest cases are when we choose unit cells 3^p ($p \in \mathbb{N}$) times larger than the original one, which corresponds to folding the BZ to $1/3^p$ of its previous size. Let us see some examples:

A) $p = 0$: original 2-atom unit cell

As we saw, the real space basis vectors read

$$\boldsymbol{a}_1^{(0)} = \left(1/2, \sqrt{3}/2\right) \sqrt{3}\, d, \quad \boldsymbol{a}_2^{(0)} = \left(-1/2, \sqrt{3}/2\right) \sqrt{3}\, d, \tag{2.24}$$

while the respective reciprocal space ones are given by

$$\boldsymbol{b}_1^{(0)} = \left(\sqrt{3}/2, 1/2\right) \frac{4\pi}{3d}, \quad \boldsymbol{b}_2^{(0)} = \left(-\sqrt{3}/2, 1/2\right) \frac{4\pi}{3d}. \tag{2.25}$$

B) $p = 1$: 6-atom unit cell

Taking a look at fig. 2.3(a), we observe that

$$\boldsymbol{a}_1^{(1)} = \left(\sqrt{3}/2, 1/2\right) 3d, \quad \boldsymbol{a}_2^{(1)} = \left(-\sqrt{3}/2, 1/2\right) 3d, \tag{2.26}$$

and, therefore, we obtain

$$\boldsymbol{b}_1^{(1)} = \left(1/2, \sqrt{3}/2\right) \frac{4\pi}{3\sqrt{3}\, d}, \quad \boldsymbol{b}_2^{(1)} = \left(-1/2, \sqrt{3}/2\right) \frac{4\pi}{3\sqrt{3}\, d}. \tag{2.27}$$

C) $p = 2$: 18-atom unit cell

In this case (fig. 2.3(b)), we have

$$\boldsymbol{a}_1^{(2)} = \left(1/2, \sqrt{3}/2\right) 3\sqrt{3}\, d, \quad \boldsymbol{a}_2^{(2)} = \left(-1/2, \sqrt{3}/2\right) 3\sqrt{3}\, d, \tag{2.28}$$

and we get

$$\boldsymbol{b}_1^{(2)} = \left(\sqrt{3}/2, 1/2\right) \frac{4\pi}{9d}, \quad \boldsymbol{b}_2^{(2)} = \left(-\sqrt{3}/2, 1/2\right) \frac{4\pi}{9d}. \tag{2.29}$$

We observe a pattern that occurs at all levels: the basis vectors directions interchange with respect to the previous ones, while the parameter rescales as $d \to \sqrt{3}\, d$. We can thus write, for the general case,

$$\boldsymbol{a}_1^{(p)} = \begin{cases} \left(1/2, \sqrt{3}/2\right) \sqrt{3}^{\,p+1} d & \text{if } p \text{ is even} \\ \left(\sqrt{3}/2, 1/2\right) \sqrt{3}^{\,p+1} d & \text{if } p \text{ is odd} \end{cases}, \quad \boldsymbol{a}_2^{(p)} = \begin{cases} \left(-1/2, \sqrt{3}/2\right) \sqrt{3}^{\,p+1} d & \text{if } p \text{ is even} \\ \left(-\sqrt{3}/2, 1/2\right) \sqrt{3}^{\,p+1} d & \text{if } p \text{ is odd} \end{cases}, \tag{2.30}$$

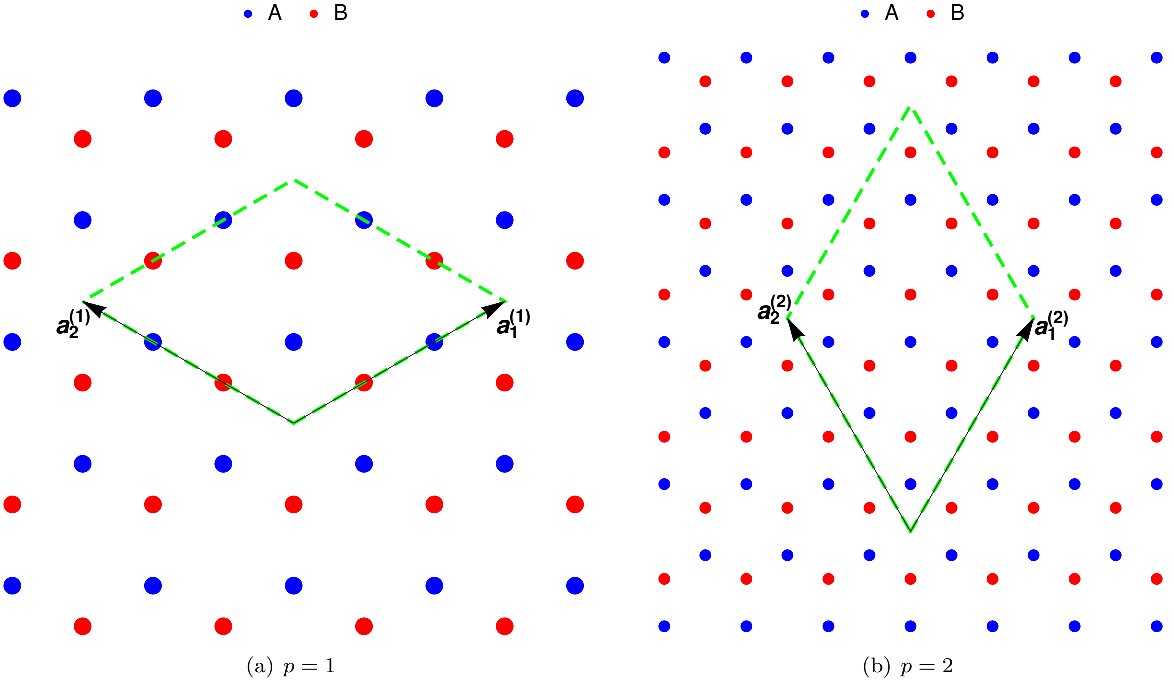

(a) $p = 1$ (b) $p = 2$

Figure 2.3: Basis vectors and unit cells for a folded SLG description with (a) $p = 1$ (6-atom unit cell), (b) $p = 2$ (18-atom unit cell).

$$\boldsymbol{b}_1^{(p)} = \begin{cases} \left(\sqrt{3}/2, 1/2\right) \frac{4\pi}{\sqrt{3}^p 3d} & \text{if } p \text{ is even} \\ \left(1/2, \sqrt{3}/2\right) \frac{4\pi}{\sqrt{3}^p 3d} & \text{if } p \text{ is odd} \end{cases}, \quad \boldsymbol{b}_2^{(p)} = \begin{cases} \left(-\sqrt{3}/2, 1/2\right) \frac{4\pi}{\sqrt{3}^p 3d} & \text{if } p \text{ is even} \\ \left(-1/2, \sqrt{3}/2\right) \frac{4\pi}{\sqrt{3}^p 3d} & \text{if } p \text{ is odd} \end{cases}. \tag{2.31}$$

With this established, we now want to write down the Hamiltonian for the general case. We could always rewrite the Hamiltonian for the new, larger unit cell in direct space and then follow the same procedure as before. But we do not want to do that. We expect that it should be possible to write the new Hamiltonian directly in reciprocal space in terms of the previous unfolded one. The strategy can be figured out by a close inspection on fig. 2.4(a). When using the enlarged unit cell, we are reducing the size of the BZ by 1/3. However, although the description is different, the overall system is the same. Hence, we are basically comprising the information from regions 2 and 3 to the new BZ (labeled 1). Let us now imagine that we already have the Hamiltonian for the folded case. Since we have 6 atoms per unit cell, we must have 3 sets of 2 bands (positive and negative, due to particle-hole symmetry). If we then represent the spectrum using an extended zone scheme —the first 2 bands in the first BZ, the second ones in the second BZ and the third ones in the third BZ— we obtain a spectrum that coincides exactly with the unfolded one. This provides a way of putting the information from regions 2 and 3 into 1. We observe that, for each $\boldsymbol{k}$ in region 1, we can get to regions 2 and 3 (or equivalents) by translations of $\boldsymbol{b}_1^{(1)}$ and $\boldsymbol{b}_2^{(1)}$. Recalling our unfolded original Hamiltonian,

$$H_{\boldsymbol{k}}^{(0)} = \begin{bmatrix} 0 & -tf(\boldsymbol{k}) \\ -tf^*(\boldsymbol{k}) & 0 \end{bmatrix}, \tag{2.32}$$

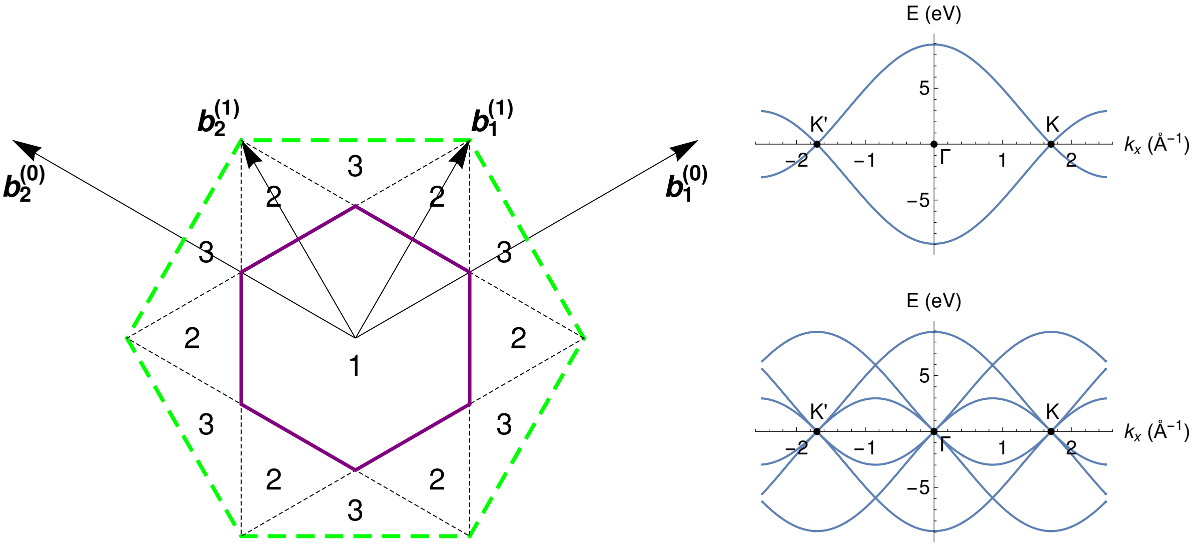

(a)

(b)

Figure 2.4: (a) Reciprocal space folding scheme. The green dashed line marks the original BZ, while the purple line marks the BZ for a $p = 1$ folding. Regions labeled by 1, 2 and 3 correspond to the first, second and third BZs for the folded case. (b) Electronic spectrum for $p = 0$ (top) and $p = 1$ (bottom). Plots with $k_y = 0\text{Å}^{-1}$.

we may now write the folded Hamiltonian in the enlarged basis, $|\boldsymbol{k}\rangle$, $|\boldsymbol{k} + \boldsymbol{b}_1^{(1)}\rangle$, $|\boldsymbol{k} + \boldsymbol{b}_2^{(1)}\rangle$, as

$$H_{\boldsymbol{k}}^{(1)} = \begin{bmatrix} H_{\boldsymbol{k}}^{(0)} & 0 & 0 \\ 0 & H_{\boldsymbol{k}+\boldsymbol{b}_1^{(1)}}^{(0)} & 0 \\ 0 & 0 & H_{\boldsymbol{k}+\boldsymbol{b}_2^{(1)}}^{(0)} \end{bmatrix}. \tag{2.33}$$

For a given p, it is straightforward to generalize and write

$$H_{\boldsymbol{k}}^{(p)} = \begin{bmatrix} H_{\boldsymbol{k}}^{(p-1)} & 0 & 0 \\ 0 & H_{\boldsymbol{k}+\boldsymbol{b}_1^{(p)}}^{(p-1)} & 0 \\ 0 & 0 & H_{\boldsymbol{k}+\boldsymbol{b}_2^{(p)}}^{(p-1)} \end{bmatrix}. \tag{2.34}$$

Note that inside $H^{(p)}$, we have informations of all Hamiltonians back to the original one, $H^{(0)}$.

In fig. 2.4(b), we plot the eigenvalues for both original and $1/3$ folded Hamiltonians. This construction will be useful to understand the tBLG, as we will see in section 2.3.6.

2.1.6 Density of states and carrier density

In appendix A, we briefly introduce general concepts about DOS and carrier density and explain a numerical method to compute them, given the electronic spectrum. Results for the SLG are presented in fig. 2.5. We first address the carrier density. Experimentally, record values up to $|n| \sim 4 \times 10^{14}\text{cm}^{-2}$ have been reported [44]. Nevertheless, under ambient conditions, typical values for doping are one order of magnitude below [45–47]. We will stick within this range, which corresponds to the zoomed region in the plot (fig.2.5(b)). As can be seen from this representation, the corresponding Fermi level is too far

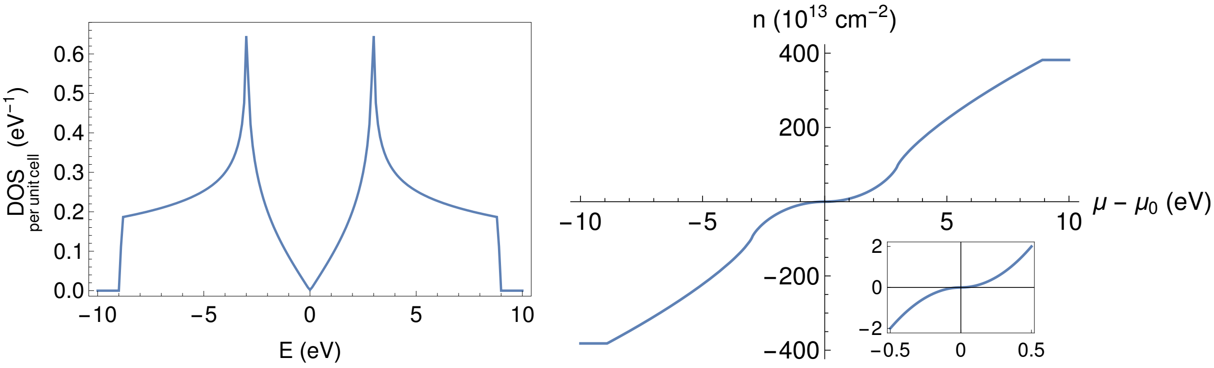

(a) DOS (b) Carrier density

Figure 2.5: DOS and carrier density for SLG.

from what is needed to reach the peaks in the DOS (van Hove singularities), making them inaccessible. This is a big downside since electronic instabilities that can lead to new phases of matter are expected when we cross the Fermi level with a van Hove singularity [48–50]. One of the reasons that motivates the study of tBLG systems is precisely the fact that we can bring van Hove singularities to arbitrarily low energies by varying the rotation angle [51].

2.2 Introduction to bilayers: Bernal-stacked bilayer graphene

2.2.1 Geometry

A BLG is a stacking of two SLGs, where the typical experimental interlayer distance is $d_\perp = 3.35$Å [17]. It can exist in three distinct arrangements: 1) AA stacking, where each carbon atom from the top layer is placed exactly above its correspondent in the lower layer; 2) AB stacking, or Bernal stacking, in which the atoms of sublattice A from one layer are aligned with the atoms of sublattice B from the other layer, implying the remaining to be located in the center of the hexagons; 3) tBLG, where one layer is rotated by some angle θ with respect to the other. Experimentally, the AA stacking is considered metastable, while both AB stacking and tBLG are found to be stable [17]. In this section, we will focus on the AB stacking, whose geometry we show in fig. 2.6.

2.2.2 Tight-binding model

To model this system, we will retain the approximations used before for each individual layer; in addition, we will take into account interlayer hopping, in a transversal tight-binding approximation between NN only. We start by splitting the total Hamiltonian in three terms,

$$H = H_1 + H_2 + H_\perp, \tag{2.35}$$

where H_i is the Hamiltonian for each individual layer i, while $H_\perp$ takes into account interlayer (transversal) hopping terms. In the second quantized formalism, using the former approximations and already

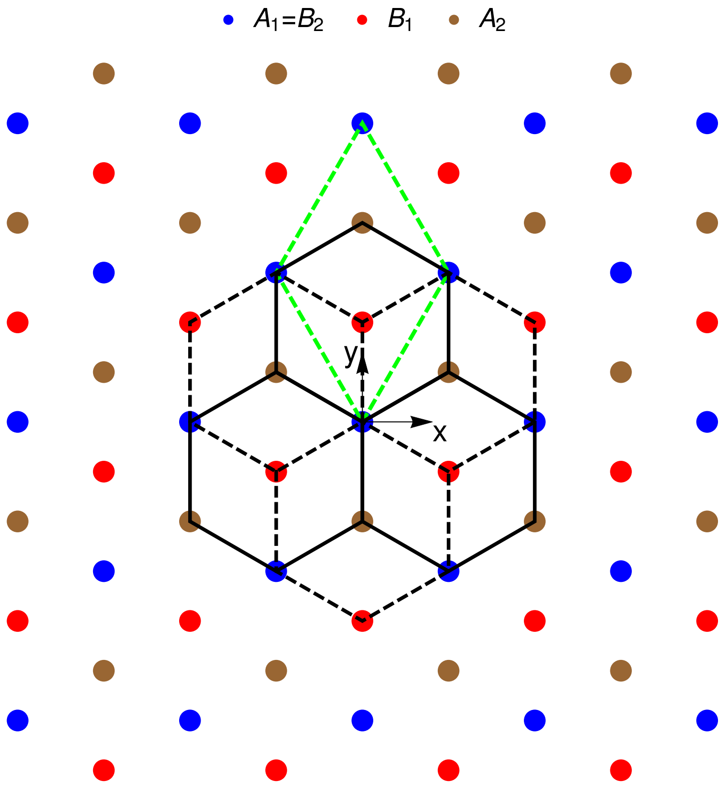

Figure 2.6: AB stacking BLG geometry (top view). We call the bottom layer (dashed black lines) layer 1 and the top layer (filled black lines) layer 2. We maintain the same unit cell used for the SLG (green dashed line), keeping both direct and reciprocal space descriptions identical as before, except that each unit cell now contains 4 atoms.

redefining the zero of energy to ϵ_{p_z}, we can write

$$H_1 = -t \sum_{n_1,n_2} \sum_{\sigma} a^{\dagger}_{1,\sigma}\left(\boldsymbol{R}_{n_1,n_2}\right)\left[b_{1,\sigma}\left(\boldsymbol{R}_{n_1,n_2}\right) + b_{1,\sigma}\left(\boldsymbol{R}_{n_1,n_2} - \boldsymbol{a}_1\right) + b_{1,\sigma}\left(\boldsymbol{R}_{n_1,n_2} - \boldsymbol{a}_2\right)\right] + \text{h.c.}, \tag{2.36}$$

$$H_2 = -t \sum_{n_1,n_2} \sum_{\sigma} a^{\dagger}_{2,\sigma}\left(\boldsymbol{R}_{n_1,n_2}\right)\left[b_{2,\sigma}\left(\boldsymbol{R}_{n_1,n_2}\right) + b_{2,\sigma}\left(\boldsymbol{R}_{n_1,n_2} - \boldsymbol{a}_1\right) + b_{2,\sigma}\left(\boldsymbol{R}_{n_1,n_2} - \boldsymbol{a}_2\right)\right] + \text{h.c.}, \tag{2.37}$$

where $c^{\dagger}_{i,\sigma}\left(\boldsymbol{R}\right)$ $\left(c_{i,\sigma}\left(\boldsymbol{R}\right)\right)$ is the creation (destruction) fermionic operator for an electron of spin σ ($\sigma =\uparrow,\downarrow$) on an atom in layer i, cell $\boldsymbol{R}$ and sublattice C and h.c. stands for hermitian conjugate. For the interlayer hopping terms, we consider an homogeneous interlayer hopping, $t_{\perp}$, between NN only, and obtain the following non-null matrix elements for $H_{\perp}$:

$$\langle \boldsymbol{R}_{n_1,n_2}, A, 1 | H_{\perp} | \boldsymbol{R}_{n_1,n_2}, B, 2 \rangle = t_{\perp}, \tag{2.38}$$

where we added another label to our bra-ket notation to distinguish between layers. In the second quantized formalism, we can thus write

$$H_{\perp} = t_{\perp} \sum_{n_1,n_2} \sum_{\sigma} a^{\dagger}_{1,\sigma}\left(\boldsymbol{R}_{n_1,n_2}\right) b_{2,\sigma}\left(\boldsymbol{R}_{n_1,n_2}\right) + \text{h.c.}. \tag{2.39}$$

Now, we move to the reciprocal space. Since our fermionic operators are only defined in lattice points, we shall perform a discrete Fourier transform (dFT), which is usually defined in the following manner: for a function $g_{\boldsymbol{R_n}}$ defined only in lattice points $\boldsymbol{R_n}$, the dFT and its inverse (IdFT) are, respectively,

$$g(\boldsymbol{k}) = \sum_{\boldsymbol{R_n}} g_{\boldsymbol{R_n}} e^{-i\boldsymbol{k}.\boldsymbol{R_n}}, \tag{2.40}$$

$$g_{\boldsymbol{R_n}} = \frac{1}{V_{BZ}} \int_{BZ} d\boldsymbol{k}\; g(\boldsymbol{k}) e^{i\boldsymbol{k}.\boldsymbol{R_n}}, \tag{2.41}$$

where V_{BZ} is the BZ volume. At this point, we stress that a Fourier transform (FT) always has some arbitrariness in its definition, since normalizations and phases can be changed consistently. According to ref. [52], in order to keep the basis convention we used for the SLG (and the orthonormality), we should have

$$a_{1,\sigma}\left(\boldsymbol{R}_{n_1,n_2}\right) = \frac{1}{\sqrt{A_{BZ}}} \int_{BZ} d\boldsymbol{k}\; a_{1,\sigma}(\boldsymbol{k}) e^{i\boldsymbol{k}.\boldsymbol{R}_{n_1,n_2}}, \tag{2.42}$$

$$b_{1,\sigma}\left(\boldsymbol{R}_{n_1,n_2}\right) = \frac{1}{\sqrt{A_{BZ}}} \int_{BZ} d\boldsymbol{k}\; b_{1,\sigma}(\boldsymbol{k}) e^{i\boldsymbol{k}.(\boldsymbol{R}_{n_1,n_2}+\boldsymbol{\delta})}, \tag{2.43}$$

$$a_{2,\sigma}\left(\boldsymbol{R}_{n_1,n_2}\right) = \frac{1}{\sqrt{A_{BZ}}} \int_{BZ} d\boldsymbol{k}\; a_{2,\sigma}(\boldsymbol{k}) e^{i\boldsymbol{k}.(\boldsymbol{R}_{n_1,n_2}-\boldsymbol{\delta})}, \tag{2.44}$$

$$b_{2,\sigma}\left(\boldsymbol{R}_{n_1,n_2}\right) = \frac{1}{\sqrt{A_{BZ}}} \int_{BZ} d\boldsymbol{k}\; b_{2,\sigma}(\boldsymbol{k}) e^{i\boldsymbol{k}.\boldsymbol{R}_{n_1,n_2}}, \tag{2.45}$$

where we changed notation, from V_{BZ} to A_{BZ} (BZ area), because our system is 2D. Applying these IdFTs, and making use of the orthogonality relation,

$$\sum_{n_1,n_2} e^{\pm i(\boldsymbol{k}-\boldsymbol{k'}).\boldsymbol{R}_{n_1,n_2}} = N_1 N_2 \delta_{\boldsymbol{k},\boldsymbol{k'}}, \quad \boldsymbol{k},\boldsymbol{k'} \in BZ, \tag{2.46}$$

we obtain

$$H_1 = -t\frac{N_1 N_2}{A_{BZ}} \sum_{\sigma} \int_{BZ} d\boldsymbol{k}\; a^{\dagger}_{1,\sigma}(\boldsymbol{k}) b_{1,\sigma}(\boldsymbol{k}) f(\boldsymbol{k}) + \text{h.c.}, \tag{2.47}$$

$$H_2 = -t\frac{N_1 N_2}{A_{BZ}} \sum_{\sigma} \int_{BZ} d\boldsymbol{k}\; a^{\dagger}_{2,\sigma}(\boldsymbol{k}) b_{2,\sigma}(\boldsymbol{k}) f(\boldsymbol{k}) + \text{h.c.}, \tag{2.48}$$

$$H_{\perp} = t_{\perp}\frac{N_1 N_2}{A_{BZ}} \sum_{\sigma} \int_{BZ} d\boldsymbol{k}\; a^{\dagger}_{1,\sigma}(\boldsymbol{k}) b_{2,\sigma}(\boldsymbol{k}) + \text{h.c.}, \tag{2.49}$$

where $f(\boldsymbol{k})$ is given by (2.17). Using that

$$A_{u.c.} = |\boldsymbol{a}_1 \times \boldsymbol{a}_2| = \frac{\sqrt{3}\,d_{hex}^2}{2}, \quad A_{BZ} = |\boldsymbol{b}_1 \times \boldsymbol{b}_2| = (2\pi)^2 \frac{2}{\sqrt{3}\,d_{hex}^2}, \tag{2.50}$$

we obtain the useful relation,

$$A_{BZ} = \frac{(2\pi)^2}{A_{u.c.}}, \tag{2.51}$$

from which we can re-write the total Hamiltonian as

$$H = -t\frac{A_{total}}{(2\pi)^2} \sum_{\sigma} \int_{BZ} d\boldsymbol{k} \left[a^{\dagger}_{1,\sigma}(\boldsymbol{k}) b_{1,\sigma}(\boldsymbol{k}) f(\boldsymbol{k}) + a^{\dagger}_{2,\sigma}(\boldsymbol{k}) b_{2,\sigma}(\boldsymbol{k}) f(\boldsymbol{k}) - a^{\dagger}_{1,\sigma}(\boldsymbol{k}) b_{2,\sigma}(\boldsymbol{k}) \frac{t_{\perp}}{t} + \text{h.c.} \right], \tag{2.52}$$

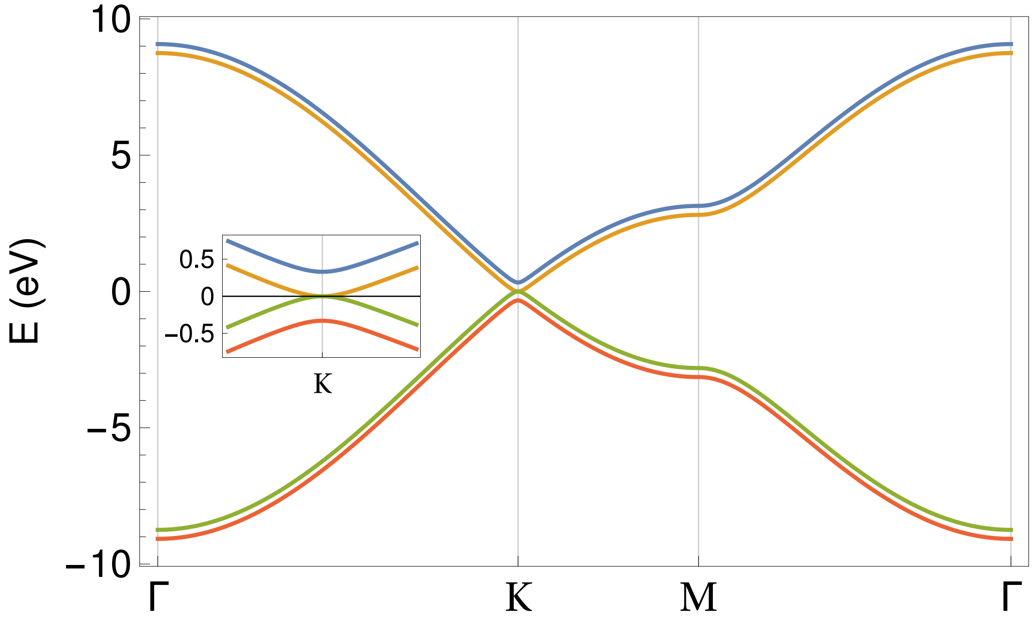

Figure 2.7: Electronic spectrum for AB stacking BLG, along the $\boldsymbol{k}$-space trajectory $\Gamma \to K \to M \to \Gamma$. We set $t_\perp = 0.33\text{eV}$, compatible with the range of estimated values [17].

where $A_{total} = N_1 N_2 A_{u.c.}$ is the total area. Arranging (2.52) in a convenient matrix form,

$$H = \frac{A_{total}}{(2\pi)^2} \sum_\sigma \int_{BZ} d\boldsymbol{k}\ \Psi_\sigma^\dagger(\boldsymbol{k}) H(\boldsymbol{k}) \Psi_\sigma(\boldsymbol{k}), \tag{2.53}$$

where $\Psi_\sigma(\boldsymbol{k})$ is a four component spinor for destruction operators,

$$\Psi_\sigma(\boldsymbol{k}) = \begin{bmatrix} a_{1,\sigma}(\boldsymbol{k}) \\ b_{1,\sigma}(\boldsymbol{k}) \\ a_{2,\sigma}(\boldsymbol{k}) \\ b_{2,\sigma}(\boldsymbol{k}) \end{bmatrix}, \tag{2.54}$$

we recognize $H(\boldsymbol{k})$ as the Hamiltonian in the matrix form,

$$H(\boldsymbol{k}) = -t \begin{bmatrix} 0 & f(\boldsymbol{k}) & 0 & -t_\perp/t \\ f^*(\boldsymbol{k}) & 0 & 0 & 0 \\ 0 & 0 & 0 & f(\boldsymbol{k}) \\ -t_\perp/t & 0 & f^*(\boldsymbol{k}) & 0 \end{bmatrix}. \tag{2.55}$$

Diagonalizing it, we obtain the eigenvalues

$$E(\boldsymbol{k}) = \pm t \sqrt{\left(\frac{t_\perp}{2t}\right)^2 + 4\cos\left(\frac{\sqrt{3}}{2} d k_x\right) \cos\left(\frac{3}{2} d k_y\right) + 2\cos\left(\sqrt{3}\, d k_x\right) + 3} \pm \frac{t_\perp}{2}, \tag{2.56}$$

which we plot for a representative first BZ path in fig. 2.7.

2.2.3 Low-energy Hamiltonian

Once again, we find the low-energy regime near the first BZ corners. We may then expand, as before, the Hamiltonian (2.55) around K and K', obtaining

$$H(\boldsymbol{q}) = \hbar v_F \begin{bmatrix} 0 & \pm q_x - iq_y & 0 & t_\perp/(\hbar v_F) \\ \pm q_x + iq_y & 0 & 0 & 0 \\ 0 & 0 & 0 & \pm q_x - iq_y \\ t_\perp/(\hbar v_F) & 0 & \pm q_x + iq_y & 0 \end{bmatrix}. \tag{2.57}$$

At this point, it is worth introducing a method to simplify this 4×4 Hamiltonian even further. When we are interested in an (even lower) energy scale $E \ll t_\perp$, we may neglect the high energy bands at $E \sim \pm t_\perp$ (see the inset from fig. 2.7) and work with an effective 2×2 matrix Hamiltonian. In order to derive this effective Hamiltonian, we have to eliminate (integrate out) high energy degrees of freedom associated with states living essentially in the coupled sublattices A_1 and B_2. We will perform this elimination using a method based on Green's functions, which we derive in appendix B.

Before applying (B.13) to our matrix Hamiltonian, (2.57), we have to order the basis properly. Given our spinor (2.54), we see that we are currently using the basis A_1, B_1, A_2, B_2. Since we want to eliminate the high energy degrees of freedom associated with sites A_1 and B_2, we should reorder our basis to A_2, B_1, A_1, B_2 (for example). In this basis, (2.57) becomes

$$H(\boldsymbol{q}) = \hbar v_F \begin{bmatrix} 0 & 0 & 0 & \pm q_x - iq_y \\ 0 & 0 & \pm q_x + iq_y & 0 \\ 0 & \pm q_x - iq_y & 0 & t_\perp/(\hbar v_F) \\ \pm q_x + iq_y & 0 & t_\perp/(\hbar v_F) & 0 \end{bmatrix}. \tag{2.58}$$

Applying (B.13) to our reordered Hamiltonian, and using $E \approx 0$ (valid in the limit $E \ll t_\perp$), we finally get:

$$\begin{aligned} H^{eff}(\boldsymbol{q}) &= 0 - \frac{(\hbar v_F)^2}{t_\perp} \begin{bmatrix} 0 & \pm q_x - iq_y \\ \pm q_x + iq_y & 0 \end{bmatrix} \begin{bmatrix} 0 & 1 \\ 1 & 0 \end{bmatrix}^{-1} \begin{bmatrix} 0 & \pm q_x - iq_y \\ \pm q_x + iq_y & 0 \end{bmatrix} \\ &= -\frac{(\hbar v_F)^2}{t_\perp} \begin{bmatrix} 0 & \pm q_x - iq_y \\ \pm q_x + iq_y & 0 \end{bmatrix} \begin{bmatrix} \pm q_x + iq_y & 0 \\ 0 & \pm q_x - iq_y \end{bmatrix} \\ &= -\frac{(\hbar v_F)^2}{t_\perp} \begin{bmatrix} 0 & (\pm q_x - iq_y)^2 \\ (\pm q_x + iq_y)^2 & 0 \end{bmatrix} \\ &= -\frac{\tilde{p}^2}{2m^*} \boldsymbol{\sigma}.\boldsymbol{n}(\pm 2\theta_{\boldsymbol{q}}), \end{aligned} \tag{2.59}$$

where $\tilde{p} = \hbar|\boldsymbol{q}|$ is the momentum measured from the Dirac point, $m^* = t_\perp/(2v_F^2)$ is recognized as the effective mass, $\theta_{\boldsymbol{q}} = \arg(q_x + iq_y)$ is the momentum orientation relative to the x axis and $\boldsymbol{n}(x) = (\cos(x), \sin(x))$ is a unitary vector. This has differences and similarities with both Schrödinger and Dirac Hamiltonians.

2.3 Twisted bilayer graphene

2.3.1 Geometry and moiré pattern

We begin by establishing a general geometry for a tBLG. A completely arbitrary arrangement can be achieved in the following manner: we start with a Bernal stacking, then rotate the second layer by θ (anti-clockwise and about the origin) and finally translate it by $\boldsymbol{\tau}$. This way, each layer is described by the following lattice:

$$\boldsymbol{R}^{(1)}_{n_1,n_2} = n_1\boldsymbol{a}_1 + n_2\boldsymbol{a}_2, \tag{2.60}$$

$$\boldsymbol{R}^{(2)}_{n_1,n_2} = R_\theta\left(n_1\boldsymbol{a}_1 + n_2\boldsymbol{a}_2 - \boldsymbol{\delta}\right) + \boldsymbol{\tau}, \tag{2.61}$$

where R_θ is the rotation matrix that describes an anti-clockwise rotation by θ about the origin of a 2D coordinate system,

$$R_\theta = \begin{bmatrix} \cos(\theta) & -\sin(\theta) \\ \sin(\theta) & \cos(\theta) \end{bmatrix}. \tag{2.62}$$

We stress that, by our convention, each lattice vector takes us to a sublattice A carbon. From (2.60) and (2.61), we retain the useful relation

$$\boldsymbol{R}^{(2)}_{n_1,n_2} = R_\theta\left(\boldsymbol{R}^{(1)}_{n_1,n_2} - \boldsymbol{\delta}\right) + \boldsymbol{\tau}. \tag{2.63}$$

In fig. 2.8, we present a particular case of a tBLG geometry, highlighting the moiré pattern arising from its crystallographic alignment. This moiré pattern can be predicted for any configuration, as we detail below.

Moiré pattern determination

Layer 1 is described by a direct lattice $\boldsymbol{R}^{(1)}$ with basis vectors $\boldsymbol{a}_1$ and $\boldsymbol{a}_2$; by definition, the corresponding reciprocal lattice, $\boldsymbol{G}^{(1)}$, has basis vectors $\boldsymbol{b}_1$ and $\boldsymbol{b}_2$. In the same way, layer 2 is described by a lattice $\boldsymbol{R}^{(2)}$ with basis vectors $\boldsymbol{a}_1^\theta$ and $\boldsymbol{a}_2^\theta$ (introducing the notation $\boldsymbol{v}^\theta \equiv R_\theta \boldsymbol{v}$, where $\boldsymbol{v}$ is an arbitrary 2D vector); its corresponding reciprocal lattice, $\boldsymbol{G}^{(2)}$, has, therefore, basis vectors $\boldsymbol{b}_1^\theta$ and $\boldsymbol{b}_2^\theta$ [2]. Translations in real space do not affect the $\boldsymbol{k}$-space description, wherefore it is valid to keep track of the basis vectors only. For commensurate structures —structures where there are atoms from one layer that exactly overlap atoms from the other— there is a (larger) lattice $\boldsymbol{R'}$ belonging to both original lattices. Using an equivalent definition for the reciprocal lattice (compatible with (2.21)),

$$e^{i\boldsymbol{R}.\boldsymbol{G}} = 1, \tag{2.64}$$

we see that $\boldsymbol{R'}$ must satisfy

$$e^{i\boldsymbol{R'}.\boldsymbol{G}^{(1)}} = 1, \quad e^{i\boldsymbol{R'}.\boldsymbol{G}^{(2)}} = 1. \tag{2.65}$$

---

[2] It is straightforward to check, from definition (2.21), that a rotation in real space implies the same rotation in reciprocal space, and vice versa.

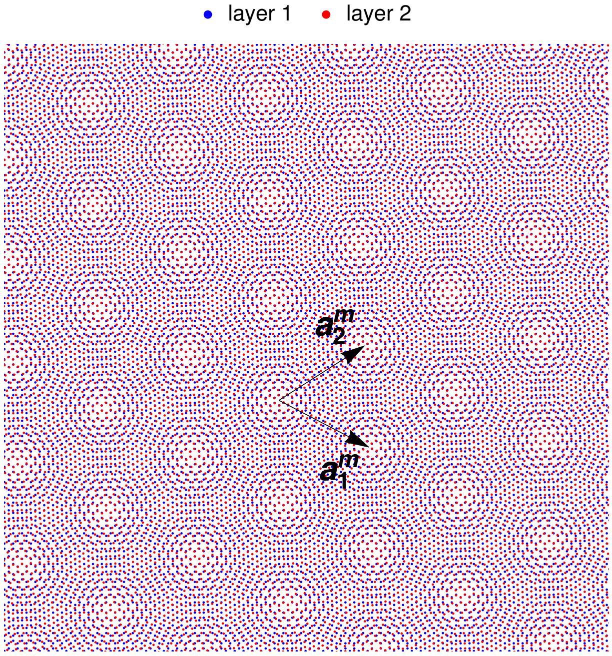

Figure 2.8: tBLG geometry for $\theta = 5^\circ$ and $\boldsymbol{\tau} = \mathbf{0}$ (top view). Vectors $\boldsymbol{a}_1^m$ and $\boldsymbol{a}_2^m$ mark the basis for the (readily visible) large-scale hexagonal moiré pattern.

The reciprocal lattice for our moiré pattern, $\boldsymbol{G}^m$, also satisfies, by definition,

$$e^{i\boldsymbol{R'}.\boldsymbol{G}^m} = 1, \tag{2.66}$$

so we see that

$$\{\boldsymbol{G}^m\} = \{\boldsymbol{G}^{(1)}\} \cup \{\boldsymbol{G}^{(2)}\}. \tag{2.67}$$

From this last result, we conclude that the basis vectors for $\boldsymbol{G}^m$, $\boldsymbol{b}_1^m$ and $\boldsymbol{b}_2^m$, are the smallest vectors obtained by the union of all vectors $\boldsymbol{G}^{(1)}$ and $\boldsymbol{G}^{(2)}$. For $|\theta| \leq 30^\circ$, we choose

$$\boldsymbol{b}_1^m = \boldsymbol{b}_1 - \boldsymbol{b}_1^\theta, \quad \boldsymbol{b}_2^m = \boldsymbol{b}_2 - \boldsymbol{b}_2^\theta, \tag{2.68}$$

which is compatible with an hexagonal mSL. For $|\theta| > 30^\circ$, we can use the SLG $\frac{\pi}{3}$ symmetry and reduce this case to the former one. With this mSL defined in reciprocal space, the corresponding mSL in real space, $\boldsymbol{R}^m$, is trivially obtained by calculating its basis vectors $\boldsymbol{a}_1^m$ and $\boldsymbol{a}_2^m$ from definition,

$$\boldsymbol{a}_i^m.\boldsymbol{b}_j^m = 2\pi\delta_{i,j}. \tag{2.69}$$

For incommensurate structures, these results were verified to hold by our numerical results. In short, we generated a function with the same periodicity of layer 2 (for arbitrary θ and $\boldsymbol{\tau}$); then, we evaluated it in the points that define layer 1; finally, we performed a numerical dFT to this list of points and extracted the maximums, obtaining dominant $\boldsymbol{k}$'s in agreement with the expected ones for an hexagonal mSL with basis vectors $\boldsymbol{b}_1^m$ and $\boldsymbol{b}_2^m$.

2.3.2 Rotated Dirac Hamiltonian

From now on, we closely follow the work done in ref. [26] and explain the model we shall adopt for this material. We begin by obtaining the Dirac Hamiltonian for a rotated SLG. We start with the SLG Dirac Hamiltonian (2.23) and write it as

$$H_{SLG}^{\pm K}(\boldsymbol{q}) = \pm\hbar v_F|\boldsymbol{q}|\begin{bmatrix} 0 & e^{\mp i\theta_{\boldsymbol{q}}} \\ e^{\pm i\theta_{\boldsymbol{q}}} & 0 \end{bmatrix}, \tag{2.70}$$

For a rotated SLG [3], we may argue that, applying the same (passive) transformation to our coordinate system, we obtain the same expression. Then, we can go back to our primary coordinate system and write

$$H_{SLG}^{\pm K}(\boldsymbol{q},\theta) = \pm\hbar v_F|\boldsymbol{q}|\begin{bmatrix} 0 & e^{\mp i(\theta_{\boldsymbol{q}}+\theta)} \\ e^{\pm i(\theta_{\boldsymbol{q}}+\theta)} & 0 \end{bmatrix}, \tag{2.71}$$

where $\boldsymbol{q}$ is now measured from the rotated Dirac points, $\pm K^{\theta}$.

2.3.3 Interlayer hopping term

We proceed to the derivation of an expression for the interlayer hopping term. We start by defining the matrix element,

$$T_{\boldsymbol{k},\boldsymbol{k'}}^{\alpha,\beta} = \langle\psi_{\boldsymbol{k},\alpha}^{(1)}|\, H_{\perp}\, |\psi_{\boldsymbol{k'},\beta}^{(2)}\rangle\,, \tag{2.72}$$

which describes a process where an electron with momentum $\boldsymbol{k'}$ in layer 2, sublattice β, hops to a momentum state $\boldsymbol{k}$ in layer 1, sublattice α. In the tight-binding approximation, we have

$$|\psi_{\boldsymbol{k},\alpha}^{(1)}\rangle = \frac{1}{\sqrt{N_1N_2}}\sum_{n_1,n_2} e^{i\boldsymbol{k}\cdot\left(\boldsymbol{R}_{n_1,n_2}^{(1)}+\boldsymbol{\delta}_{\alpha}^{(1)}\right)}\,|\boldsymbol{R}_{n_1,n_2}^{(1)}+\boldsymbol{\delta}_{\alpha}^{(1)},\alpha\rangle\,, \tag{2.73}$$

$$|\psi_{\boldsymbol{k'},\beta}^{(2)}\rangle = \frac{1}{\sqrt{N_1N_2}}\sum_{n_1,n_2} e^{i\boldsymbol{k'}\cdot\left(\boldsymbol{R}_{n_1,n_2}^{(2)}+\boldsymbol{\delta}_{\beta}^{(2)}\right)}\,|\boldsymbol{R}_{n_1,n_2}^{(2)}+\boldsymbol{\delta}_{\beta}^{(2)},\beta\rangle\,, \tag{2.74}$$

where

$$\boldsymbol{\delta}_{\alpha}^{(1)} = \boldsymbol{\delta}_{\alpha}, \quad \boldsymbol{\delta}_{\beta}^{(2)} = \boldsymbol{\delta}_{\beta}^{\theta}. \tag{2.75}$$

Let us now calculate the following matrix element of interest (which is, for now, completely general):

$$\begin{aligned} T_{K+\boldsymbol{q}_1,K^{\theta}+\boldsymbol{q}_2^{\theta}}^{\alpha,\beta} =& \frac{1}{N_1N_2}\sum_{n_1,n_2}\sum_{n_1',n_2'} e^{-i(K+\boldsymbol{q}_1)\cdot\left(\boldsymbol{R}_{n_1,n_2}^{(1)}+\boldsymbol{\delta}_{\alpha}^{(1)}\right)}\, e^{i(K^{\theta}+\boldsymbol{q}_2^{\theta})\cdot\left(\boldsymbol{R}_{n_1',n_2'}^{(2)}+\boldsymbol{\delta}_{\beta}^{(2)}\right)}\times \\ & \times\langle\boldsymbol{R}_{n_1,n_2}^{(1)}+\boldsymbol{\delta}_{\alpha}^{(1)},\alpha|\, H_{\perp}\, |\boldsymbol{R}_{n_1',n_2'}^{(2)}+\boldsymbol{\delta}_{\beta}^{(2)},\beta\rangle\,. \end{aligned} \tag{2.76}$$

---

[3] From now on, by convention, when we do not specify the rotation, we are always referring to anti-clockwise rotations by θ about the origin. Once again, translations do not affect anything at this point.

Similarly to what we did before, we introduce an interlayer matrix element, $t_\perp$; however, this time, we do not consider it as homogeneus but rather dependent on the distance between both atomic orbitals,

$$\langle \boldsymbol{R}^{(1)}_{n_1,n_2} + \boldsymbol{\delta}^{(1)}_\alpha, \alpha | \, H_\perp \, | \boldsymbol{R}^{(2)}_{n'_1,n'_2} + \boldsymbol{\delta}^{(2)}_\beta, \beta \rangle = t_\perp \left(\boldsymbol{R}^{(1)}_{n_1,n_2} + \boldsymbol{\delta}^{(1)}_\alpha - \boldsymbol{R}^{(2)}_{n'_1,n'_2} - \boldsymbol{\delta}^{(2)}_\beta \right). \tag{2.77}$$

Recalling eq. (2.63), and dropping the index (1) in $\boldsymbol{R}^{(1)}$ in order to simplify the notation, we then write

$$\begin{aligned} T^{\alpha,\beta}_{K+\boldsymbol{q}_1, K^\theta+\boldsymbol{q}^\theta_2} =& \frac{1}{N_1 N_2} \sum_{n_1,n_2} \sum_{n'_1,n'_2} e^{-i(K+\boldsymbol{q}_1).(\boldsymbol{R}_{n_1,n_2}+\boldsymbol{\delta}_\alpha)} \; e^{i(K^\theta+\boldsymbol{q}^\theta_2).(\boldsymbol{R}^\theta_{n'_1,n'_2}-\boldsymbol{\delta}^\theta+\boldsymbol{\tau}+\boldsymbol{\delta}^\theta_\beta)} \times \\ & \times t_\perp \left(\boldsymbol{R}_{n_1,n_2} - \boldsymbol{R}^\theta_{n'_1,n'_2} + \boldsymbol{\delta}_\alpha - \boldsymbol{\delta}^\theta_\beta + \boldsymbol{\delta}^\theta - \boldsymbol{\tau} \right). \end{aligned} \tag{2.78}$$

Applying a FT to $t_\perp$,

$$t_\perp \left(\boldsymbol{R}_{n_1,n_2} - \boldsymbol{R}^\theta_{n'_1,n'_2} + \boldsymbol{\delta}_\alpha - \boldsymbol{\delta}^\theta_\beta + \boldsymbol{\delta}^\theta - \boldsymbol{\tau} \right) = \int_{\mathbb{R}^2} \frac{d\boldsymbol{k}}{(2\pi)^2} \; t_\perp(\boldsymbol{k}) \; e^{i\boldsymbol{k}.\left(\boldsymbol{R}_{n_1,n_2} - \boldsymbol{R}^\theta_{n'_1,n'_2} + \boldsymbol{\delta}_\alpha - \boldsymbol{\delta}^\theta_\beta + \boldsymbol{\delta}^\theta - \boldsymbol{\tau} \right)}, \tag{2.79}$$

and making use of the well-known relation,

$$\sum_{\boldsymbol{k}} \to \frac{A_{total}}{(2\pi)^2} \int_{\mathbb{R}^2} d\boldsymbol{k}, \tag{2.80}$$

which states the way we can alternate from an infinite sum in the quantized $\boldsymbol{k}$'s of a finite system with PBC to an integral in the limit $N_i \to \infty$ (and vice-versa), we obtain

$$\begin{aligned} T^{\alpha,\beta}_{K+\boldsymbol{q}_1, K^\theta+\boldsymbol{q}^\theta_2} =& \frac{1}{(N_1 N_2)^2} \sum_{n_1,n_2} \sum_{n'_1,n'_2} \sum_{\boldsymbol{k}} e^{i[\boldsymbol{k}-(K+\boldsymbol{q}_1)].\boldsymbol{R}_{n_1,n_2}} \; e^{i\left[(K^\theta+\boldsymbol{q}^\theta_2)-\boldsymbol{k}\right].\boldsymbol{R}^\theta_{n'_1,n'_2}} \times \\ & \times e^{i[\boldsymbol{k}-(K+\boldsymbol{q}_1)].\boldsymbol{\delta}_\alpha} \; e^{i\left[(K^\theta+\boldsymbol{q}^\theta_2)-\boldsymbol{k}\right].(\boldsymbol{\delta}^\theta_\beta-\boldsymbol{\delta}^\theta+\boldsymbol{\tau})} \; \frac{t_\perp(\boldsymbol{k})}{A_{u.c.}}. \end{aligned} \tag{2.81}$$

Now, we use the orthogonality relations,

$$\sum_{n_1,n_2} e^{i[\boldsymbol{k}-(K+\boldsymbol{q}_1)].\boldsymbol{R}_{n_1,n_2}} = \begin{cases} N_1 N_2 & \text{if } \boldsymbol{k} - (K+\boldsymbol{q}_1) = \boldsymbol{G}^{(1)}_{k,l} \equiv \boldsymbol{G}_{k,l}, \ \forall k,l \in \mathbb{Z} \\ 0 & \text{otherwise} \end{cases}, \tag{2.82}$$

$$\sum_{n'_1,n'_2} e^{i\left[(K^\theta+\boldsymbol{q}^\theta_2)-\boldsymbol{k}\right].\boldsymbol{R}^\theta_{n'_1,n'_2}} = \begin{cases} N_1 N_2 & \text{if } \boldsymbol{k} - (K^\theta+\boldsymbol{q}^\theta_2) = \boldsymbol{G}^{(2)}_{m,n} \equiv \boldsymbol{G}^\theta_{m,n}, \ \forall m,n \in \mathbb{Z} \\ 0 & \text{otherwise} \end{cases}, \tag{2.83}$$

which imply

$$\boldsymbol{k} = K + \boldsymbol{q}_1 + \boldsymbol{G}_{k,l} = K^\theta + \boldsymbol{q}^\theta_2 + \boldsymbol{G}^\theta_{m,n}, \tag{2.84}$$

to simplify our expression into

$$T^{\alpha,\beta}_{K+\boldsymbol{q}_1, K^\theta+\boldsymbol{q}^\theta_2} = \sum_{k,l,m,n} \frac{t_\perp(K+\boldsymbol{q}_1+\boldsymbol{G}_{k,l})}{A_{u.c.}} \; e^{i\left[\boldsymbol{G}_{k,l}.\boldsymbol{\delta}_\alpha - \boldsymbol{G}_{m,n}.(\boldsymbol{\delta}_\beta-\boldsymbol{\delta}) - \boldsymbol{G}^\theta_{m,n}.\boldsymbol{\tau}\right]} \; \delta_{K+\boldsymbol{q}_1+\boldsymbol{G}_{k,l}, K^\theta+\boldsymbol{q}^\theta_2+\boldsymbol{G}^\theta_{m,n}}. \tag{2.85}$$

Taking a look at this expression, we notice that the moiré pattern reveals itself in the Kronecker delta, $\delta_{K+\boldsymbol{q_1}+\boldsymbol{G}_{k,l},K^\theta+\boldsymbol{q}_2^\theta+\boldsymbol{G}_{m,n}^\theta}$. This delta dictates that the momentum difference in the interlayer hopping must be a vector resulting from the union of all vectors $\boldsymbol{G}$ and $\boldsymbol{G}^\theta$, as expected.

2.3.4 Fourier transform for the two-center interlayer hopping

The continuum low-energy model is obtained by considering wave vectors in both layers relative to their respective Dirac points with small deviations compared to the BZ dimensions: $|\boldsymbol{q}_1|, |\boldsymbol{q}_2| \ll |K|$. Notice that, by doing so, a K expansion is implicit at this point. The model's usefulness rests, as we shall see, on numerical results known for $t_\perp(\boldsymbol{k})$, which indicate that it should fall to zero very rapidly with $|\boldsymbol{k}|$ on the reciprocal lattice scale. Intuitively, since $d_\perp > d$ by more than a factor of 2, the two-center interlayer hopping term, $t_\perp(\boldsymbol{r}^{(1)} - \boldsymbol{r}^{(2)})$, which depends on the three dimensional separation, $\sqrt{|\boldsymbol{r}^{(1)} - \boldsymbol{r}^{(2)}|^2 + d_\perp^2}$, varies with $\boldsymbol{r}^{(1)} - \boldsymbol{r}^{(2)}$ on the scale of $d_\perp$ for the small $\boldsymbol{r}^{(1)} - \boldsymbol{r}^{(2)}$ regime (which describes the dominant interlayer hopping). Therefore, $t_\perp(\boldsymbol{r}^{(1)} - \boldsymbol{r}^{(2)})$ has a broadened distribution and $t_\perp(\boldsymbol{k})$, its FT, is sharp and declines very rapidly for $|\boldsymbol{k}|d_\perp > 1$. Below, we quantitatively show this results.

We start by finding the expression for $t_\perp(\boldsymbol{k})$. Recalling (2.79), we proceed with the following manipulation:

$$\begin{aligned}
&\sum_{n_1,n_2} e^{-i\boldsymbol{k'}.\left(\boldsymbol{R}_{n_1,n_2}-\boldsymbol{R}^\theta_{n_1',n_2'}+\boldsymbol{\delta}_\alpha-\boldsymbol{\delta}^\theta_\beta+\boldsymbol{\delta}^\theta-\boldsymbol{\tau}\right)} t_\perp\left(\boldsymbol{R}_{n_1,n_2}-\boldsymbol{R}^\theta_{n_1',n_2'}+\boldsymbol{\delta}_\alpha-\boldsymbol{\delta}^\theta_\beta+\boldsymbol{\delta}^\theta-\boldsymbol{\tau}\right)\\
&\quad= \sum_{n_1,n_2}\int_{\mathbb{R}^2}\frac{d\boldsymbol{k}}{(2\pi)^2}\; t_\perp(\boldsymbol{k})\; e^{i(\boldsymbol{k}-\boldsymbol{k'}).\left(\boldsymbol{R}_{n_1,n_2}-\boldsymbol{R}^\theta_{n_1',n_2'}+\boldsymbol{\delta}_\alpha-\boldsymbol{\delta}^\theta_\beta+\boldsymbol{\delta}^\theta-\boldsymbol{\tau}\right)}\\
&\quad= N_1N_2\int_{\mathbb{R}^2}\frac{d\boldsymbol{k}}{(2\pi)^2}\; t_\perp(\boldsymbol{k})\delta_{\boldsymbol{k}-\boldsymbol{k'},\boldsymbol{G}}\; e^{i(\boldsymbol{k}-\boldsymbol{k'}).\left(-\boldsymbol{R}^\theta_{n_1',n_2'}+\boldsymbol{\delta}_\alpha-\boldsymbol{\delta}^\theta_\beta+\boldsymbol{\delta}^\theta-\boldsymbol{\tau}\right)}\\
&\quad= \frac{N_1N_2}{A_{total}}\sum_{\boldsymbol{k}}\; t_\perp(\boldsymbol{k})\delta_{\boldsymbol{k}-\boldsymbol{k'},\boldsymbol{G}}\; e^{i(\boldsymbol{k}-\boldsymbol{k'}).\left(-\boldsymbol{R}^\theta_{n_1',n_2'}+\boldsymbol{\delta}_\alpha-\boldsymbol{\delta}^\theta_\beta+\boldsymbol{\delta}^\theta-\boldsymbol{\tau}\right)}\\
&\quad= \frac{1}{A_{u.c.}}\sum_{\boldsymbol{G}}\; t_\perp(\boldsymbol{k'}+\boldsymbol{G})\; e^{i\boldsymbol{G}.\left(-\boldsymbol{R}^\theta_{n_1',n_2'}+\boldsymbol{\delta}_\alpha-\boldsymbol{\delta}^\theta_\beta+\boldsymbol{\delta}^\theta-\boldsymbol{\tau}\right)}.
\end{aligned} \tag{2.86}$$

We now notice that, while $e^{i\boldsymbol{G}.\boldsymbol{R}_{n_1,n_2}} = 1$ holds for any reciprocal lattice vector $\boldsymbol{G}$ of the unrotated lattice, it does not hold in general for the rotated one, $e^{i\boldsymbol{G}.\boldsymbol{R}^\theta_{n_1',n_2'}} \neq 1$, unless $\boldsymbol{G} = \boldsymbol{G}^\theta$. Therefore, if we sum over $\boldsymbol{R}^\theta_{n_1',n_2'}$ on both sides, we arrive at

$$\begin{aligned}
&\sum_{n_1,n_2}\sum_{n_1',n_2'} e^{-i\boldsymbol{k'}.\left(\boldsymbol{R}_{n_1,n_2}-\boldsymbol{R}^\theta_{n_1',n_2'}+\boldsymbol{\delta}_\alpha-\boldsymbol{\delta}^\theta_\beta+\boldsymbol{\delta}^\theta-\boldsymbol{\tau}\right)} t_\perp\left(\boldsymbol{R}_{n_1,n_2}-\boldsymbol{R}^\theta_{n_1',n_2'}+\boldsymbol{\delta}_\alpha-\boldsymbol{\delta}^\theta_\beta+\boldsymbol{\delta}^\theta-\boldsymbol{\tau}\right)\\
&\qquad= \frac{N_1N_2}{A_{u.c.}}\sum_{\substack{\tilde{\boldsymbol{G}}\\(\tilde{\boldsymbol{G}}=\boldsymbol{G}=\boldsymbol{G}^\theta)}} t_\perp(\boldsymbol{k'}+\tilde{\boldsymbol{G}})\; e^{i\tilde{\boldsymbol{G}}.\left(\boldsymbol{\delta}_\alpha-\boldsymbol{\delta}^\theta_\beta+\boldsymbol{\delta}^\theta-\boldsymbol{\tau}\right)}.
\end{aligned} \tag{2.87}$$

If our system is incommensurate, we only have one vector $\tilde{\boldsymbol{G}}$ satisfying $\tilde{\boldsymbol{G}} = \boldsymbol{G} = \boldsymbol{G}^\theta$, which is $\tilde{\boldsymbol{G}} = \boldsymbol{0}$. If not, we have others, but we expect them to be dominated by the smallest one, $\tilde{\boldsymbol{G}} = \boldsymbol{0}$, by our previous intuitive argument. Therefore, we continue retaining only $\tilde{\boldsymbol{G}} = \boldsymbol{0}$ and write

$$t_\perp(\boldsymbol{k'}) = \frac{A_{u.c.}}{N_1 N_2} \sum_{n_1,n_2} \sum_{n'_1,n'_2} e^{-i\boldsymbol{k'}\cdot\left(\boldsymbol{R}_{n_1,n_2} - \boldsymbol{R}^\theta_{n'_1,n'_2} + \boldsymbol{\delta}_\alpha - \boldsymbol{\delta}^\theta_\beta + \boldsymbol{\delta}^\theta - \boldsymbol{\tau}\right)} t_\perp\left(\boldsymbol{R}_{n_1,n_2} - \boldsymbol{R}^\theta_{n'_1,n'_2} + \boldsymbol{\delta}_\alpha - \boldsymbol{\delta}^\theta_\beta + \boldsymbol{\delta}^\theta - \boldsymbol{\tau}\right). \tag{2.88}$$

Summing over the sublattices on both sides,

$$\begin{aligned}
\sum_{\alpha,\beta} t_\perp(\boldsymbol{k'}) &= 4\ t_\perp(\boldsymbol{k'}) \\
&= \frac{A_{u.c.}}{N_1 N_2} \sum_{\alpha,\beta} \sum_{n_1,n_2} \sum_{n'_1,n'_2} e^{-i\boldsymbol{k'}\cdot\left(\boldsymbol{R}_{n_1,n_2} - \boldsymbol{R}^\theta_{n'_1,n'_2} + \boldsymbol{\delta}_\alpha - \boldsymbol{\delta}^\theta_\beta + \boldsymbol{\delta}^\theta - \boldsymbol{\tau}\right)} t_\perp\left(\boldsymbol{R}_{n_1,n_2} - \boldsymbol{R}^\theta_{n'_1,n'_2} + \boldsymbol{\delta}_\alpha - \boldsymbol{\delta}^\theta_\beta + \boldsymbol{\delta}^\theta - \boldsymbol{\tau}\right) \\
&= \frac{A_{u.c.}}{N_1 N_2} \sum_{\boldsymbol{r}^{(1)}} \sum_{\boldsymbol{r}^{(2)}} e^{-i\boldsymbol{k'}\cdot\left(\boldsymbol{r}^{(1)} - \boldsymbol{r}^{(2)}\right)} t_\perp\left(\boldsymbol{r}^{(1)} - \boldsymbol{r}^{(2)}\right),
\end{aligned} \tag{2.89}$$

where $\boldsymbol{r}^{(i)}$ represents all points in the honeycomb structure of layer i, we arrive at

$$t_\perp(\boldsymbol{k'}) = \frac{1}{4} \frac{A_{u.c.}}{N_1 N_2} \sum_{\boldsymbol{r}^{(1)}} \sum_{\boldsymbol{r}^{(2)}} e^{-i\boldsymbol{k'}\cdot\left(\boldsymbol{r}^{(1)} - \boldsymbol{r}^{(2)}\right)} t_\perp\left(\boldsymbol{r}^{(1)} - \boldsymbol{r}^{(2)}\right). \tag{2.90}$$

At this point, we notice that the function $\tilde{t_\perp}(\boldsymbol{r}^{(1)})$, which we write as

$$\tilde{t_\perp}(\boldsymbol{r}^{(1)}) = \sum_{\boldsymbol{r}^{(2)}} e^{-i\boldsymbol{k'}\cdot\left(\boldsymbol{r}^{(1)} - \boldsymbol{r}^{(2)}\right)} t_\perp\left(\boldsymbol{r}^{(1)} - \boldsymbol{r}^{(2)}\right), \tag{2.91}$$

is a periodic function with the periodicity of the moiré pattern, i.e., $\tilde{t_\perp}(\boldsymbol{r}^{(1)} + \boldsymbol{R}^m) = \tilde{t_\perp}(\boldsymbol{r}^{(1)})$. To show this, we invoke that all differences $\boldsymbol{r}^{(1)} - \boldsymbol{r}^{(2)}$ can be obtained by letting $\boldsymbol{r}^{(2)}$ run over all points from layer 2, while $\boldsymbol{r}^{(1)}$ runs over points from layer 1 inside a moiré unit cell only. We may then write

$$t_\perp(\boldsymbol{k'}) = \frac{1}{4} \frac{A_{u.c.}}{N_1 N_2} N_{m.u.c.} \sum_{\boldsymbol{r}^{(1)} \in \text{moiré}} \sum_{\boldsymbol{r}^{(2)}} e^{-i\boldsymbol{k'}\cdot\left(\boldsymbol{r}^{(1)} - \boldsymbol{r}^{(2)}\right)} t_\perp\left(\boldsymbol{r}^{(1)} - \boldsymbol{r}^{(2)}\right), \tag{2.92}$$

where $N_{m.u.c.}$ is the total number of moiré unit cells in our system. Finally, we use the relation

$$\frac{N_1 N_2}{N_{m.u.c.}} = N^m_{u.c.} = \frac{N^m_{sites}}{2}, \tag{2.93}$$

where $N^m_{u.c}$ and N^m_{sites} are, respectively, the number of unit cells and sites in a moiré unit cell, to arrive at our final expression for $t_\perp(\boldsymbol{k})$,

$$t_\perp(\boldsymbol{k}) = \frac{1}{2} \frac{A_{u.c.}}{N^m_{sites}} \sum_{\boldsymbol{r}^{(1)} \in \text{moiré}} \sum_{\boldsymbol{r}^{(2)}} e^{-i\boldsymbol{k}\cdot\left(\boldsymbol{r}^{(1)} - \boldsymbol{r}^{(2)}\right)} t_\perp\left(\boldsymbol{r}^{(1)} - \boldsymbol{r}^{(2)}\right). \tag{2.94}$$

To model $t_\perp\left(\boldsymbol{r}^{(1)} - \boldsymbol{r}^{(2)}\right)$, we begin by expressing it via Slater-Koster parameters [53], $V_{pp\sigma}$ and $V_{pp\pi}$, as follows:

$$t_\perp\left(\boldsymbol{r}^{(1)} - \boldsymbol{r}^{(2)}\right) = \cos^2(\gamma)\ V_{pp\sigma}\left(\sqrt{d_\perp^2 + |\boldsymbol{r}^{(1)} - \boldsymbol{r}^{(2)}|^2}\right) + \sin^2(\gamma)\ V_{pp\pi}\left(\sqrt{d_\perp^2 + |\boldsymbol{r}^{(1)} - \boldsymbol{r}^{(2)}|^2}\right), \tag{2.95}$$

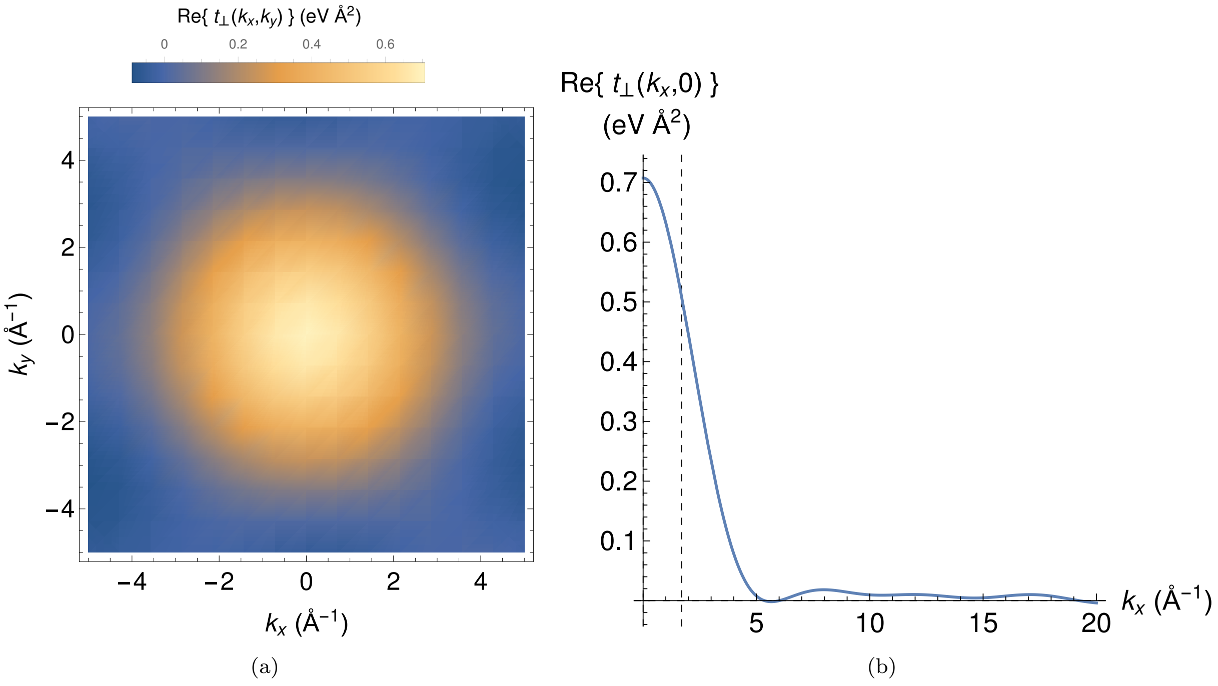

Figure 2.9: FT for the interlayer hopping in tBLG (real part). Although not plotted, the imaginary part was shown to be negligible, as expected. In (a), we show the full 2D FT, where we observe an apparently circular symmetry, $t_\perp(\boldsymbol{k}) \approx t_\perp(|\boldsymbol{k}|)$. In (b), $t_\perp(\boldsymbol{k})$ is plotted along the k_x axis, with the black dashed line crossing it at the Dirac point K.

where $V_{pp\sigma}(r)$ and $V_{pp\pi}(r)$ depend only on the distance between the two sites, and γ is the angle between the z axis and the line connecting $\boldsymbol{r}^{(1)}$ to $\boldsymbol{r}^{(2)}$, which leads to

$$\cos^2(\gamma) = \frac{d_\perp^2}{d_\perp^2 + |\boldsymbol{r}^{(1)} - \boldsymbol{r}^{(2)}|^2}. \tag{2.96}$$

In ref. [22], the authors explored an exponentially-decreasing model for $V_{pp\sigma}$ and $V_{pp\pi}$, which we shall adopt:

$$V_{pp\sigma}(r) = t_\perp \exp\left[q_\sigma(1 - r/d_\perp)\right], \quad V_{pp\pi}(r) = -t \exp\left[q_\pi(1 - r/d)\right]. \tag{2.97}$$

We stress that $V_{pp\pi}(d) = -t$ and $V_{pp\sigma}(d_\perp) = t_\perp$, which is consistent with the previous results for the SLG and the AB stacking BLG. To fix q_π, the authors took the characteristic second NN hopping amplitude in SLG, $t' \approx 0.1t$ [54], and obtained

$$\frac{V_{pp\pi}(d)}{V_{pp\pi}(\sqrt{3}\,d)} = \frac{t}{t'} = 10 = \frac{1}{\exp\left[q_\pi(1-\sqrt{3})\right]} = \exp\left[q_\pi(\sqrt{3}-1)\right] \Leftrightarrow q_\pi = \frac{\log(10)}{\sqrt{3}-1} \simeq 3.15. \tag{2.98}$$

The remaining parameter, q_σ, was fixed assuming equal spatial exponential-decreasing coefficients, i.e.,

$$\frac{q_\pi}{d} = \frac{q_\sigma}{d_\perp} \Leftrightarrow q_\sigma = q_\pi \frac{d_\perp}{d} \simeq 7.42. \tag{2.99}$$

Using this model, we numerically computed the desired FT (2.94). The results (fig. 2.9) are in agreement with what we antecipated. We verified that it suffices to consider only the NN from layer 2 in the sum over all $\boldsymbol{r}^{(2)}$; moreover, it checks out that the obtained results are roughly independent of θ.

2.3.5 Interlayer hopping term: simplifications and picture

Within the continuum low-energy model, we may simplify (2.85) by performing the sum in k, l retaining only the largest values for $t_\perp(K + \boldsymbol{q}_1 + \boldsymbol{G}_{k,l})$. In this approximation, we keep the reciprocal lattice vectors $\boldsymbol{G} = \boldsymbol{0}, \boldsymbol{b}_2, -\boldsymbol{b}_1$, which correspond to interlayer hopping terms with momentum close to the three equivalent Dirac points K. This leads to

$$\begin{aligned} T^{\alpha,\beta}_{K+\boldsymbol{q}_1, K^\theta+\boldsymbol{q}^\theta_2} \simeq & \frac{t_\perp(K)}{A_{u.c.}} \sum_{m,n} \Bigg[e^{-i\left[\boldsymbol{G}_{m,n}\cdot(\boldsymbol{\delta}_\beta - \boldsymbol{\delta}) + \boldsymbol{G}^\theta_{m,n}.\boldsymbol{\tau}\right]} \; \delta_{K+\boldsymbol{q}_1, K^\theta+\boldsymbol{q}^\theta_2+\boldsymbol{G}^\theta_{m,n}} + \\ & + e^{i\left[\boldsymbol{b}_2.\boldsymbol{\delta}_\alpha - \boldsymbol{G}_{m,n}\cdot(\boldsymbol{\delta}_\beta - \boldsymbol{\delta}) - \boldsymbol{G}^\theta_{m,n}.\boldsymbol{\tau}\right]} \; \delta_{K+\boldsymbol{q}_1+\boldsymbol{b}_2, K^\theta+\boldsymbol{q}^\theta_2+\boldsymbol{G}^\theta_{m,n}} + \\ & + e^{-i\left[\boldsymbol{b}_1.\boldsymbol{\delta}_\alpha + \boldsymbol{G}_{m,n}\cdot(\boldsymbol{\delta}_\beta - \boldsymbol{\delta}) + \boldsymbol{G}^\theta_{m,n}.\boldsymbol{\tau}\right]} \; \delta_{K+\boldsymbol{q}_1-\boldsymbol{b}_1, K^\theta+\boldsymbol{q}^\theta_2+\boldsymbol{G}^\theta_{m,n}} \Bigg]. \end{aligned} \tag{2.100}$$

Due to the Kronecker deltas, and recalling our regime $|\boldsymbol{q}_1|, |\boldsymbol{q}_2| \ll |K|$, we observe that the remaining summation necessarily yields just one vector $\boldsymbol{G}^\theta$ for each of the three terms,

$$\begin{aligned} T^{\alpha,\beta}_{K+\boldsymbol{q}_1, K^\theta+\boldsymbol{q}^\theta_2} = & \frac{t_\perp(K)}{A_{u.c.}} \Bigg[\delta_{K+\boldsymbol{q}_1, K^\theta+\boldsymbol{q}^\theta_2} + e^{i\left[\boldsymbol{b}_2.(\boldsymbol{\delta}_\alpha - \boldsymbol{\delta}_\beta + \boldsymbol{\delta}) - \boldsymbol{b}^\theta_2.\boldsymbol{\tau}\right]} \; \delta_{K+\boldsymbol{q}_1+\boldsymbol{b}_2, K^\theta+\boldsymbol{q}^\theta_2+\boldsymbol{b}^\theta_2} + \\ & + e^{-i\left[\boldsymbol{b}_1.(\boldsymbol{\delta}_\alpha - \boldsymbol{\delta}_\beta + \boldsymbol{\delta}) - \boldsymbol{b}^\theta_1.\boldsymbol{\tau}\right]} \; \delta_{K+\boldsymbol{q}_1-\boldsymbol{b}_1, K^\theta+\boldsymbol{q}^\theta_2-\boldsymbol{b}^\theta_1} \Bigg]. \end{aligned} \tag{2.101}$$

In a matrix notation where $T = \begin{bmatrix} T^{A,A} & T^{A,B} \\ T^{B,A} & T^{B,B} \end{bmatrix}$, we re-write the last expression as

$$\begin{aligned} T_{K+\boldsymbol{q}_1, K^\theta+\boldsymbol{q}^\theta_2} &= \frac{t_\perp(K)}{A_{u.c.}} \Big[T_1 \; \delta_{\boldsymbol{q}^\theta_2-\boldsymbol{q}_1, K-K^\theta} + T_2 \; \delta_{\boldsymbol{q}^\theta_2-\boldsymbol{q}_1, (K+\boldsymbol{b}_2)-(K^\theta+\boldsymbol{b}^\theta_2)} + T_3 \; \delta_{\boldsymbol{q}^\theta_2-\boldsymbol{q}_1, (K-\boldsymbol{b}_1)-(K^\theta-\boldsymbol{b}^\theta_1)} \Big] \\ &= T_{\boldsymbol{q}_b} \; \delta_{\boldsymbol{q}^\theta_2-\boldsymbol{q}_1, \boldsymbol{q}_b} + T_{\boldsymbol{q}_{tr}} \; \delta_{\boldsymbol{q}^\theta_2-\boldsymbol{q}_1, \boldsymbol{q}_{tr}} + T_{\boldsymbol{q}_{tl}} \; \delta_{\boldsymbol{q}^\theta_2-\boldsymbol{q}_1, \boldsymbol{q}_{tl}}, \end{aligned} \tag{2.102}$$

where

$$T_{\boldsymbol{q}_b} = \frac{t_\perp(K)}{A_{u.c.}} T_1, \quad T_{\boldsymbol{q}_{tr}} = \frac{t_\perp(K)}{A_{u.c.}} T_2, \quad T_{\boldsymbol{q}_{tl}} = \frac{t_\perp(K)}{A_{u.c.}} T_3, \tag{2.103}$$

$$T_1 = \begin{bmatrix} 1 & 1 \\ 1 & 1 \end{bmatrix}, \quad T_2 = e^{-i\boldsymbol{b}^\theta_2.\boldsymbol{\tau}} \begin{bmatrix} e^{i\phi} & 1 \\ e^{-i\phi} & e^{i\phi} \end{bmatrix}, \quad T_3 = e^{i\boldsymbol{b}^\theta_1.\boldsymbol{\tau}} \begin{bmatrix} e^{-i\phi} & 1 \\ e^{i\phi} & e^{-i\phi} \end{bmatrix}, \quad \phi = \frac{2\pi}{3}, \tag{2.104}$$

and

$$\boldsymbol{q}_b = K - K^\theta, \quad \boldsymbol{q}_{tr} = (K + \boldsymbol{b}_2) - (K^\theta + \boldsymbol{b}^\theta_2), \quad \boldsymbol{q}_{tl} = (K - \boldsymbol{b}_1) - (K^\theta - \boldsymbol{b}^\theta_1). \tag{2.105}$$

Taking the limit $\theta \to 0, \boldsymbol{\tau} = \boldsymbol{0}$, which corresponds to the AB stacking configuration, we obtain

$$\langle \psi^{(1)}_{K+\boldsymbol{q}_1,\alpha} | \, H_\perp \, | \psi^{(2)}_{K+\boldsymbol{q}_2,\beta} \rangle = T^{\alpha,\beta}_{K+\boldsymbol{q}_1, K+\boldsymbol{q}_2} = \frac{t_\perp(K)}{A_{u.c.}} \begin{bmatrix} 0 & 3 \\ 0 & 0 \end{bmatrix} \delta_{\boldsymbol{q}_1,\boldsymbol{q}_2} = 3 \frac{t_\perp(K)}{A_{u.c.}} \delta_{\alpha,A} \delta_{\beta,B} \delta_{\boldsymbol{q}_1,\boldsymbol{q}_2}, \tag{2.106}$$

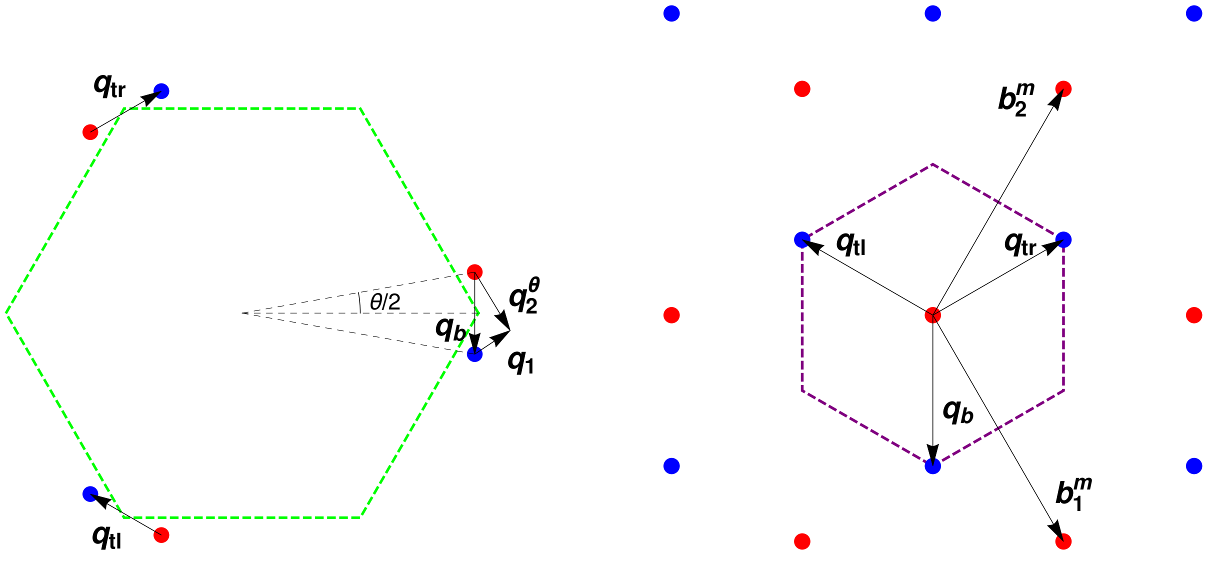

(a)

(b)

Figure 2.10: Momentum-space geometrical picture for the interlayer hopping on a tBLG. (a) The green dashed line marks the first BZ for an unrotated SLG; the red (blue) circles mark the three equivalent Dirac points K for layer 1 (2). Crystal momentum conservation is attained when $\boldsymbol{q}_2^\theta - \boldsymbol{q}_1 = \boldsymbol{q}_b, \boldsymbol{q}_{tr}, \boldsymbol{q}_{tl}$; in this reference frame, the three momentum transfers have modulus $|\boldsymbol{q}_j| = 2|\boldsymbol{K}|\sin(\theta/2)$ and directions $(0,-1)$ for $j = b$ (bottom), $(\sqrt{3}/2, 1/2)$ for $j = tr$ (top right), and $(-\sqrt{3}/2, 1/2)$ for $j = tl$ (top left). (b) The three equivalent Dirac points in the first BZ result in three distinct hopping processes in reciprocal space (matrix elements); when we capture all "orders" of hopping (possible hopping processes after previous ones), we obtain this $\boldsymbol{k}$-space honeycomb structure, which captures the periodicity of the moiré pattern. The purple dashed line marks a moiré unit cell in reciprocal space.

which we can compare with our previous result (2.49) and therefore fix our unknown parameter $t_\perp(K)$ by the relation

$$3\frac{t_\perp(K)}{A_{u.c.}} = t_\perp. \tag{2.107}$$

We highlight that this relation fixes $t_\perp(K)$ such that

$$t_\perp(K) = \frac{A_{u.c.}}{3} t_\perp \simeq 0.58\text{eV}\,\text{Å}^2, \tag{2.108}$$

which is, to a good approximation, consistent with the result obtained by the numerical computation (fig. 2.9(b)).

The interpretation of these results is more elegant when we move to the reference frame where layer 1 is rotated by $-\theta/2$ and layer 2 by $\theta/2$ (it suffices to rotate our previous coordinate system by $\theta/2$). Our demonstration was sufficiently general to allow us to do that, and we will stick to this reference frame from now on. The geometrical picture for this interlayer hopping is shown in fig. 2.10. The following relevant relations are also easily deduced in this reference frame:

$$\boldsymbol{q}_b = \frac{8\pi\sin(\theta/2)}{3\sqrt{3}d}(0,-1), \quad \boldsymbol{q}_{tr} = \frac{8\pi\sin(\theta/2)}{3\sqrt{3}d}(\sqrt{3}/2, 1/2), \quad \boldsymbol{q}_{tl} = \frac{8\pi\sin(\theta/2)}{3\sqrt{3}d}(-\sqrt{3}/2, 1/2), \tag{2.109}$$

$$\boldsymbol{b}_1^m = \boldsymbol{q}_b - \boldsymbol{q}_{tl} = \frac{8\pi\sin(\theta/2)}{3d}(1/2, -\sqrt{3}/2), \quad \boldsymbol{b}_2^m = \boldsymbol{q}_{tr} - \boldsymbol{q}_b = \frac{8\pi\sin(\theta/2)}{3d}(1/2, \sqrt{3}/2), \tag{2.110}$$

$$\boldsymbol{a}_1^m = \frac{\sqrt{3}d}{2\sin(\theta/2)}(\sqrt{3}/2, -1/2), \quad \boldsymbol{a}_2^m = \frac{\sqrt{3}d}{2\sin(\theta/2)}(\sqrt{3}/2, 1/2), \tag{2.111}$$

$$A_{m.u.c.} = |\boldsymbol{a}_1^m \times \boldsymbol{a}_2^m| = \frac{3\sqrt{3}d^2}{8\sin^2(\theta/2)}. \tag{2.112}$$

In the last equation, we introduced the notation $A_{m.u.c.}$ for the moiré unit cell area.

2.3.6 Hamiltonian matrix construction

Let us briefly summarize the results and assumptions we have in our model for the tBLG. The total Hamiltonian for this material is splitted as

$$H = H_1 + H_2 + H_\perp. \tag{2.113}$$

In the tight-binding approximation, the wave functions read

$$|\psi_{\boldsymbol{k}}\rangle = \sum_{\alpha,i} c_\alpha^{(i)}(\boldsymbol{k})\, |\psi_{\boldsymbol{k},\alpha}^{(i)}\rangle\,, \tag{2.114}$$

where $c_\alpha^{(i)}(\boldsymbol{k})$ is a complex constant of unit modulus. In the continuum low-energy model and within a K expansion, we obtained the following non-null matrix elements for the interlayer hopping:

$$\langle\psi_{K+\boldsymbol{q}_1,\alpha}^{(1)}|\, H_\perp\, |\psi_{K^\theta+\boldsymbol{q}_2^\theta,\beta}^{(2)}\rangle = T_{K+\boldsymbol{q}_1,K^\theta+\boldsymbol{q}_2^\theta}^{\alpha,\beta} = T_{\boldsymbol{q}_b}^{\alpha,\beta}\ \delta_{\boldsymbol{q}_2^\theta-\boldsymbol{q}_1,\boldsymbol{q}_b} + T_{\boldsymbol{q}_{tr}}^{\alpha,\beta}\ \delta_{\boldsymbol{q}_2^\theta-\boldsymbol{q}_1,\boldsymbol{q}_{tr}} + T_{\boldsymbol{q}_{tl}}^{\alpha,\beta}\ \delta_{\boldsymbol{q}_2^\theta-\boldsymbol{q}_1,\boldsymbol{q}_{tl}}. \tag{2.115}$$

The remaining non-null matrix elements come from each single layer Dirac Hamiltonian,

$$\langle\psi_{K+\boldsymbol{q}_1,\alpha}^{(1)}|\, H_1\, |\psi_{K+\boldsymbol{p}_1,\beta}^{(1)}\rangle = H_{SLG,K}^{\alpha,\beta}(\boldsymbol{q}_1, -\theta/2)\ \delta_{\boldsymbol{q}_1,\boldsymbol{p}_1}, \tag{2.116}$$

$$\langle\psi_{K^\theta+\boldsymbol{q}_2,\alpha}^{(2)}|\, H_2\, |\psi_{K^\theta+\boldsymbol{p}_2,\beta}^{(2)}\rangle = H_{SLG,K}^{\alpha,\beta}(\boldsymbol{q}_2, \theta/2)\ \delta_{\boldsymbol{q}_2,\boldsymbol{p}_2}, \tag{2.117}$$

where $H_{SLG,K}^{\alpha,\beta}(\boldsymbol{q},\theta)$ is given by (2.71) (using the same matrix notation as we used for T) and $\boldsymbol{q}_i, \boldsymbol{p}_j$ are small enough to make the Dirac K-expansion valid.

In order to determine the electronic spectrum, we use the Schrödinger equation (2.7), which for our system reads

$$(H_1 + H_2 + H_\perp)\, |\psi_{\boldsymbol{k}}\rangle = E\, |\psi_{\boldsymbol{k}}\rangle\,. \tag{2.118}$$

We immediately realize we can never get a closed system of equations by applying bras, $\langle\psi_{\boldsymbol{k},\alpha}^{(i)}| \equiv \langle\boldsymbol{k}, i, \alpha|$, as we did for the SLG. If we start, for example, with the bra $\langle K + \boldsymbol{q}, 1|$ (dropping the index of sublattice), we will have, aside from the diagonal term, reciprocal space hopping terms (matrix elements) with states $|K^\theta + \boldsymbol{q} + \boldsymbol{q}_b, 2\rangle$, $|K^\theta + \boldsymbol{q} + \boldsymbol{q}_{tr}, 2\rangle$ and $|K^\theta + \boldsymbol{q} + \boldsymbol{q}_{tl}, 2\rangle$ (we will call them the first NN in reciprocal space, in lack of better terminology); in turn, each one of these will have hopping terms with the former one and with two new states (second NN), and so on. At this point, the picture drawn in fig. 2.10(b) is really useful to understand this reasoning. We point out that the dimension of the matrix that characterizes our system of equations is always increasing with the number of NN considered; however, it does not increase with constant proportion since there are "repetitions": for example, we can readily see in the figure that both states $|K + \boldsymbol{q} + \boldsymbol{b}_1^m, 1\rangle$ and $|K + \boldsymbol{q} + \boldsymbol{b}_1^m + \boldsymbol{b}_2^m, 1\rangle$ have hopping terms with the same state $|K^\theta + \boldsymbol{q} + \boldsymbol{q}_{tr} + \boldsymbol{b}_1^m, 2\rangle$.

Let us clarify the matrix construction by showing examples. If we start with the bra $\langle K + \boldsymbol{q}, 1|$ and consider just first NN, we obtain

$$H^K(\boldsymbol{q}) \begin{bmatrix} c_A^{(1)}(K+\boldsymbol{q}) \\ c_B^{(1)}(K+\boldsymbol{q}) \\ c_A^{(2)}(K^\theta+\boldsymbol{q}+\boldsymbol{q}_b) \\ c_B^{(2)}(K^\theta+\boldsymbol{q}+\boldsymbol{q}_b) \\ c_A^{(2)}(K^\theta+\boldsymbol{q}+\boldsymbol{q}_{tr}) \\ c_B^{(2)}(K^\theta+\boldsymbol{q}+\boldsymbol{q}_{tr}) \\ c_A^{(2)}(K^\theta+\boldsymbol{q}+\boldsymbol{q}_{tl}) \\ c_B^{(2)}(K^\theta+\boldsymbol{q}+\boldsymbol{q}_{tl}) \end{bmatrix} = E^K(\boldsymbol{q}) \begin{bmatrix} c_A^{(1)}(K+\boldsymbol{q}) \\ c_B^{(1)}(K+\boldsymbol{q}) \\ c_A^{(2)}(K^\theta+\boldsymbol{q}+\boldsymbol{q}_b) \\ c_B^{(2)}(K^\theta+\boldsymbol{q}+\boldsymbol{q}_b) \\ c_A^{(2)}(K^\theta+\boldsymbol{q}+\boldsymbol{q}_{tr}) \\ c_B^{(2)}(K^\theta+\boldsymbol{q}+\boldsymbol{q}_{tr}) \\ c_A^{(2)}(K^\theta+\boldsymbol{q}+\boldsymbol{q}_{tl}) \\ c_B^{(2)}(K^\theta+\boldsymbol{q}+\boldsymbol{q}_{tl}) \end{bmatrix}, \tag{2.119}$$

where

$$H^K(\boldsymbol{q}) = \begin{bmatrix} H_{SLG}^K(\boldsymbol{q}, -\theta/2) & T_{\boldsymbol{q}_b} & T_{\boldsymbol{q}_{tr}} & T_{\boldsymbol{q}_{tl}} \\ T_{\boldsymbol{q}_b}^\dagger & H_{SLG}^K(\boldsymbol{q}+\boldsymbol{q}_b, \theta/2) & 0 & 0 \\ T_{\boldsymbol{q}_{tr}}^\dagger & 0 & H_{SLG}^K(\boldsymbol{q}+\boldsymbol{q}_{tr}, \theta/2) & 0 \\ T_{\boldsymbol{q}_{tl}}^\dagger & 0 & 0 & H_{SLG}^K(\boldsymbol{q}+\boldsymbol{q}_{tl}, \theta/2) \end{bmatrix}. \tag{2.120}$$

Without further low-energy approximations, we thus see that the minimum matrix Hamiltonian for the tBLG is 8 × 8. Instead of writting the whole system of equations, we can compress and interpret it by using the following convenient picture for the K-Hamiltonian matrix elements:

$\lvert K+\boldsymbol{q},1\rangle$	$\lvert K^\theta+\boldsymbol{q}+\boldsymbol{q}_b,2\rangle$	$\lvert K^\theta+\boldsymbol{q}+\boldsymbol{q}_{tr},2\rangle$	$\lvert K^\theta+\boldsymbol{q}+\boldsymbol{q}_{tl},2\rangle$	
$H_{SLG}^K(\boldsymbol{q},-\theta/2)$	$T_{\boldsymbol{q}_b}$	$T_{\boldsymbol{q}_{tr}}$	$T_{\boldsymbol{q}_{tl}}$	$\langle K+\boldsymbol{q},1\rvert$
$T_{\boldsymbol{q}_b}^\dagger$	$H_{SLG}^K(\boldsymbol{q}+\boldsymbol{q}_b,\theta/2)$	0	0	$\langle K^\theta+\boldsymbol{q}+\boldsymbol{q}_b,2\rvert$
$T_{\boldsymbol{q}_{tr}}^\dagger$	0	$H_{SLG}^K(\boldsymbol{q}+\boldsymbol{q}_{tr},\theta/2)$	0	$\langle K^\theta+\boldsymbol{q}+\boldsymbol{q}_{tr},2\rvert$
$T_{\boldsymbol{q}_{tl}}^\dagger$	0	0	$H_{SLG}^K(\boldsymbol{q}+\boldsymbol{q}_{tl},\theta/2)$	$\langle K^\theta+\boldsymbol{q}+\boldsymbol{q}_{tl},2\rvert$

Table 2.1: tBLG K-Hamiltonian matrix elements for $NN = 1$.

Let us now use this picture and extend our previous example to second NN. Introducing the convenient notation,

$$|K + \boldsymbol{q} + m_1\boldsymbol{b}_1^m + m_2\boldsymbol{b}_2^m, 1\rangle \equiv |(m_1, m_2), 1\rangle\,, \tag{2.121}$$

$$|K^\theta + \boldsymbol{q} + \boldsymbol{q}_b + m_1\boldsymbol{b}_1^m + m_2\boldsymbol{b}_2^m, 2\rangle \equiv |(m_1, m_2), 2\rangle\,, \tag{2.122}$$

we obtain the following non-diagonal matrix elements (the diagonal ones are trivial and are hence omitted to save space):

$\vert(0,0),1\rangle$	$\vert(0,0),2\rangle$	$\vert(0,1),2\rangle$	$\vert(-1,0),2\rangle$	$\vert(0,-1),1\rangle$	$\vert(1,0),1\rangle$	$\vert(0,1),1\rangle$	$\vert(1,1),1\rangle$	$\vert(-1,0),1\rangle$	$\vert(-1,-1),1\rangle$	$\langle(0,0),1\vert$
-	$T_{\boldsymbol{q}_b}$	$T_{\boldsymbol{q}_{tr}}$	$T_{\boldsymbol{q}_{tl}}$	0	0	0	0	0	0	$\langle(0,0),1\vert$
$T^\dagger_{\boldsymbol{q}_b}$	-	0	0	$T^\dagger_{\boldsymbol{q}_{tr}}$	$T^\dagger_{\boldsymbol{q}_{tl}}$	0	0	0	0	$\langle(0,0),2\vert$
$T^\dagger_{\boldsymbol{q}_{tr}}$	0	-	0	0	0	$T^\dagger_{\boldsymbol{q}_b}$	$T^\dagger_{\boldsymbol{q}_{tl}}$	0	0	$\langle(0,1),2\vert$
$T^\dagger_{\boldsymbol{q}_{tl}}$	0	0	-	0	0	0	0	$T^\dagger_{\boldsymbol{q}_b}$	$T^\dagger_{\boldsymbol{q}_{tr}}$	$\langle(-1,0),2\vert$
0	$T_{\boldsymbol{q}_{tr}}$	0	0	-	0	0	0	0	0	$\langle(0,-1),1\vert$
0	$T_{\boldsymbol{q}_{tl}}$	0	0	0	-	0	0	0	0	$\langle(1,0),1\vert$
0	0	$T_{\boldsymbol{q}_b}$	0	0	0	-	0	0	0	$\langle(0,1),1\vert$
0	0	$T_{\boldsymbol{q}_{tl}}$	0	0	0	0	-	0	0	$\langle(1,1),1\vert$
0	0	0	$T_{\boldsymbol{q}_b}$	0	0	0	0	-	0	$\langle(-1,0),1\vert$
0	0	0	$T_{\boldsymbol{q}_{tr}}$	0	0	0	0	0	-	$\langle(-1,-1),1\vert$

Table 2.2: tBLG K-Hamiltonian matrix elements for $NN = 2$.

Making use of this convenient notation, it becomes straightforward to show that if we perform the (unitary) change of basis,

$$|(m_1, m_2), i\rangle \to e^{im_1 \boldsymbol{b}_1^\theta \cdot \boldsymbol{\tau}} e^{im_2 \boldsymbol{b}_2^\theta \cdot \boldsymbol{\tau}} \, |(m_1, m_2), i\rangle \, , \tag{2.123}$$

which is equivalent to

$$c_\alpha^{(1)}(K + \boldsymbol{q} + m_1 \boldsymbol{b}_1^m + m_2 \boldsymbol{b}_2^m) \to e^{im_1 \boldsymbol{b}_1^\theta \cdot \boldsymbol{\tau}} e^{im_2 \boldsymbol{b}_2^\theta} \; c_\alpha^{(1)}(K + \boldsymbol{q} + m_1 \boldsymbol{b}_1^m + m_2 \boldsymbol{b}_2^m), \tag{2.124}$$

$$c_\alpha^{(2)}(K^\theta + \boldsymbol{q} + \boldsymbol{q}_b + m_1 \boldsymbol{b}_1^m + m_2 \boldsymbol{b}_2^m) \to e^{im_1 \boldsymbol{b}_1^\theta \cdot \boldsymbol{\tau}} e^{im_2 \boldsymbol{b}_2^\theta} \; c_\alpha^{(2)}(K^\theta + \boldsymbol{q} + \boldsymbol{q}_b + m_1 \boldsymbol{b}_1^m + m_2 \boldsymbol{b}_2^m), \tag{2.125}$$

our Hamiltonian becomes $\boldsymbol{\tau}$-independent and we can therefore set $\boldsymbol{\tau} = \boldsymbol{0}$ without any loss of generality.

In this matrix construction, we point out the similarities with what we have shown for the folded SLG (section 2.1.5). In fact, if we eliminate the hopping terms, we are basically using a folded description that explicitly captures the moiré periodicity to some extent (depending on the truncation). In real space, the interpretation is that we are using an enlarged unit cell with the moiré periodicity, which makes sense. Obviously, this is not as elegant as the case of the $1/3^p$ SLG folding which could always be written as a finite dimension matrix that captured the periodicity for all momenta. The major difference is that we are now using a Dirac approximation. For this reason, we should also be aware that we will obtain high-energy bands lacking physical meaning; however, this should not constitute a major problem since we are not interested in them anyway. When we add the hopping terms, we see that, the more we add, the less important we expect them to be. Nevertheless, we cannot always stick to first NN hopping terms only, because, depending on the angle, the low-energy bands may still depend on high-order NN hopping processes. This is the balance we have to test numerically in order to truncate our (in principle infinite) matrix, whose construction is automatized in our code.

2.3.7 Electronic spectrum — K and K' bands

Before moving to the electronic spectrum determination, we recall that our Hamiltonian was obtained within a low-energy expansion around K. Yet, nothing prevents us to choose the other nonequivalent Dirac point, K'. Therefore, in order to describe the complete electronic properties of this material, we should always consider both contributions, usually called K and K' bands. The deductions for the K' expansion are completely straightforward, so we will just present the final results that differ from what

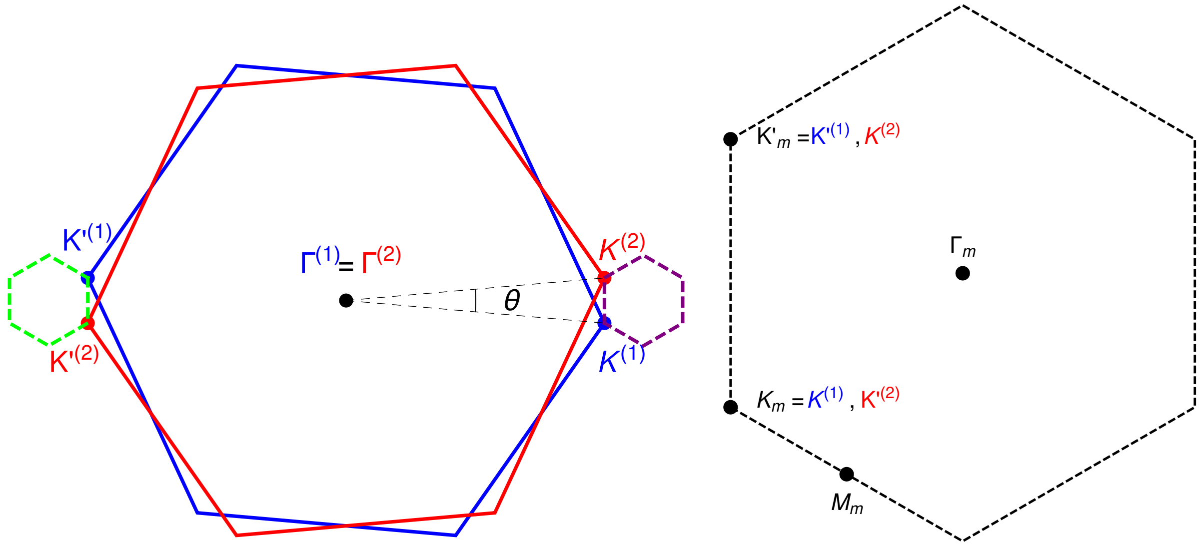

(a) (b)

Figure 2.11: K and K' bands on a tBLG. (a) Blue/red hexagons describe the BZs for layers 1/2. Dashed purple/green hexagons represent moiré unit cells in reciprocal space for K/K' expansions. (b) Moiré BZ with relevant points plotted in it.

we have obtained before:

$$\langle\psi^{(1)}_{K'+\boldsymbol{q}_1,\alpha}|\, H_1\, |\psi^{(1)}_{K'+\boldsymbol{p}_1,\beta}\rangle = H^{\alpha,\beta}_{SLG,-K}(\boldsymbol{q}_1,-\theta/2)\ \delta_{\boldsymbol{q}_1,\boldsymbol{p}_1}, \tag{2.126}$$

$$\langle\psi^{(2)}_{K'^{\theta}+\boldsymbol{q}_2,\alpha}|\, H_2\, |\psi^{(2)}_{K'^{\theta}+\boldsymbol{p}_2,\beta}\rangle = H^{\alpha,\beta}_{SLG,-K}(\boldsymbol{q}_2,\theta/2)\ \delta_{\boldsymbol{q}_2,\boldsymbol{p}_2}, \tag{2.127}$$

$$\langle\psi^{(1)}_{K'+\boldsymbol{q}_1,\alpha}|\, H_\perp\, |\psi^{(2)}_{K'^{\theta}+\boldsymbol{q}_2^{\theta},\beta}\rangle = T^{\alpha,\beta}_{-\boldsymbol{q}_b}\ \delta_{\boldsymbol{q}_2^{\theta}-\boldsymbol{q}_1,-\boldsymbol{q}_b} + T^{\alpha,\beta}_{-\boldsymbol{q}_{tr}}\ \delta_{\boldsymbol{q}_2^{\theta}-\boldsymbol{q}_1,-\boldsymbol{q}_{tr}} + T^{\alpha,\beta}_{-\boldsymbol{q}_{tl}}\ \delta_{\boldsymbol{q}_2^{\theta}-\boldsymbol{q}_1,-\boldsymbol{q}_{tl}}, \tag{2.128}$$

$$T_{-\boldsymbol{q}_b} = \frac{t_\perp}{3}\begin{bmatrix}1 & 1\\ 1 & 1\end{bmatrix},\quad T_{-\boldsymbol{q}_{tr}} = \frac{t_\perp}{3}\begin{bmatrix}e^{i\tilde{\phi}} & 1\\ e^{-i\tilde{\phi}} & e^{i\tilde{\phi}}\end{bmatrix},\quad T_{-\boldsymbol{q}_{tl}} = \frac{t_\perp}{3}\begin{bmatrix}e^{-i\tilde{\phi}} & 1\\ e^{i\tilde{\phi}} & e^{-i\tilde{\phi}}\end{bmatrix},\quad \tilde{\phi} = -\frac{2\pi}{3}. \tag{2.129}$$

The way to represent both K and K' bands in the same BZ is sketched in fig. 2.11. We notice that, in a K expansion, the wave vector $\boldsymbol{q}$ is measured from $K^{(1)}$ ($\boldsymbol{k} = K^{(1)} + \boldsymbol{q}$) while, in a K' expansion, we measure it from $K'^{(1)}$. Therefore, in order to match both moiré unit cells in reciprocal space (purple and green), we identify the points $K^{(1)}$ and $K'^{(2)}$ as the same point in the moiré BZ, such that the path $K_m \to K'_m \to M_m \to K_m$ becomes equivalent. By doing so, we are making a correspondence $H^K(\boldsymbol{q}) \leftrightarrow H^{K'}(\boldsymbol{q}+\boldsymbol{q}_b)$ in the Hamiltonians obtained within K and K' expansions.

Results for electronic spectrum, DOS and carrier density are plotted in figs. 2.12 and 2.13. Looking at the spectrum, we see that a symmetry for positive and negative bands is apparently conserved. This is unexpected *a priori*. We also observe a renormalization of the Fermi velocity, which is explored in more detail in refs. [25, 26]. Magic angles for which the Fermi velocity vanishes will be avoided in our work, due to the huge complexity that arises from describing the emergent flat bands. Addressing fig. 2.13, we confirm that, by varying the twist angle, van Hove singularities can be brought to reachable energies. For the carrier density, we observe that we start to lose the "signature behavior" of the decoupled BLG when we reach small angles. Finally, we finish with a discussion about the validity of the model. The leading

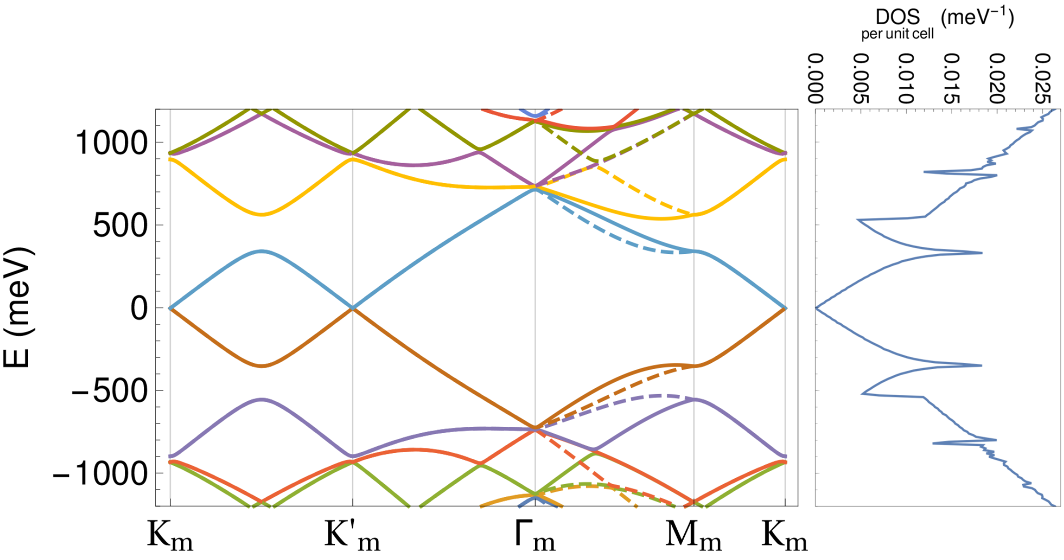

Figure 2.12: Electronic spectrum and DOS for tBLG with $\theta = 5°$. Solid and dashed lines in the spectrum are for K and K' expansions, respectively; the color code clarifies the situation in which both bands are superimposed.

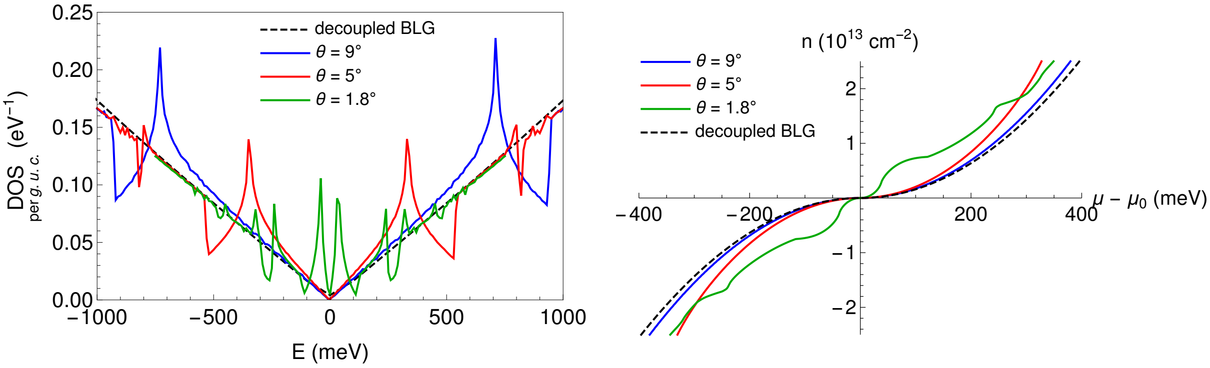

(a) DOS.

(b) Carrier density.

Figure 2.13: DOS and carrier density for different angles of a tBLG. Since the size of the unit cells varies with the angle, the DOS is normalized to the graphene unit cell (g.u.c).

corrections involve hopping amplitudes that, due to the momentum conservation $K + \boldsymbol{q}_1 + \boldsymbol{G} = K^\theta + \boldsymbol{q}_2 + \boldsymbol{G}^\theta$, are negligible when compared to $t_\perp(K)$ (see the approximation done in (2.100)). We should also not forget that we are using a Dirac approximation for the in-plane hopping. Therefore, we expect our model to be very accurate up to energies of ~ 1eV, which can still capture the first low-energy bands for $\theta \lesssim 10°$.

Chapter 3

Optical response

The scope of this chapter consists in studying the response of the tBLG system to electromagnetic stimuli. We begin with the optical conductivity. Using the linear response theory, we derive expressions that can be implemented numerically when an analytical Hamiltonian matrix is known. As benchmark, we compute the results for the SLG and interpret them; then, we apply the same method to the tBLG and compare our results to the ones obtained in the literature. In addition, we aim at determining the dispersion relation of GSPPs. We consider monolayer graphene embedded in dielectric media, and derive the equation that describes the propagation of transverse magnetic (TM) waves in the 2D surface; this equation depends on the dynamical conductivity, wherefore this follows as a direct application. Again, we make the calculations for both the SLG and tBLG.

3.1 Conductivity

3.1.1 Linear response theory

Tight-binding general description

Within a spin-independent tight-binding description of a periodic system, the electrons are described in the most general form by the Hamiltonian

$$H_0 = \sum_{\substack{\boldsymbol{k}\in BZ,\\ \gamma,\gamma',\sigma}} \epsilon_{\gamma,\gamma'}(\boldsymbol{k}) c^{\dagger}_{\boldsymbol{k},\gamma,\sigma} c_{\boldsymbol{k},\gamma',\sigma}, \tag{3.1}$$

where $\epsilon_{\gamma,\gamma'}(\boldsymbol{k}) = \langle \boldsymbol{k},\gamma|H_0(\boldsymbol{k})|\boldsymbol{k},\gamma'\rangle \equiv \langle\gamma|H_0(\boldsymbol{k})|\gamma'\rangle$ are the matrix elements of the (spin-independent) single-electron Hamiltonian matrix, $H_0(\boldsymbol{k})$, and the γ's are indices that label the entries of the states $|\boldsymbol{k},\gamma\rangle$. For SLG, γ is the sublattice index, $\gamma = \alpha = A, B$, whereas, for AB stacked BLG, γ labels sublattice and layer, $\gamma = \{\alpha, i\},\ i = 1, 2$. In the case of tBLG, γ runs over all the entries of the column vectors like the one shown in (2.119), and has therefore information about sublattice and layer. Obviously, in this case, we also have to separate the sum over the momentum $\boldsymbol{k} \in BZ$ into two sums over $\boldsymbol{q}$ in moiré BZs centered around K and K'. Finally, we stress that in this basis, $|\gamma\rangle$, the Hamiltonian is not diagonal.

Perturbative treatment to the minimal coupling

We introduce the interaction with an electromagnetic field via minimal coupling [55],

$$H(t) = \sum_{\substack{\boldsymbol{k}\in BZ,\\ \gamma,\gamma'}} \epsilon_{\gamma,\gamma'}\left(\boldsymbol{k} + \frac{e}{\hbar}\boldsymbol{A}(t)\right) c^{\dagger}_{\boldsymbol{k},\gamma} c_{\boldsymbol{k},\gamma'}, \tag{3.2}$$

where $e > 0$ is the elementary charge and $\boldsymbol{A}$ is the magnetic vector potential (uniform or slowly varying in space, such that $\boldsymbol{k}$ is still a good quantum number). Notice that the summation over spin σ is now omitted. Expanding the Hamiltonian around $\boldsymbol{k}$, we obtain the standard description of the unperturbed Hamiltonian plus a time-dependent perturbation,

$$H(t) = H_0 + V(t), \tag{3.3}$$

with the perturbative potential given by

$$V(t) = \sum_{\substack{\boldsymbol{k}\in BZ,\\ \gamma,\gamma'}} \left(\frac{e}{\hbar}\frac{\partial \epsilon_{\gamma,\gamma'}}{\partial k_{a_1}}(\boldsymbol{k}) A_{a_1}(t) + \frac{1}{2!}\left(\frac{e}{\hbar}\right)^2 \frac{\partial^2 \epsilon_{\gamma,\gamma'}}{\partial k_{a_1}\partial k_{a_2}}(\boldsymbol{k}) A_{a_1}(t) A_{a_2}(t) + ...\right) c^{\dagger}_{\boldsymbol{k},\gamma} c_{\boldsymbol{k},\gamma'}. \tag{3.4}$$

In the equation above, we clarify that we are using Einstein's summation convention for the mute indices $a_j = x, y$.

The current density operator is obtained by the functional derivative of the potential to the magnetic vector potential field, yielding

$$J_{a_1}(t) = -\frac{1}{V_{total}}\frac{\partial V(t)}{\partial A_{a_1}} = -\frac{e}{\hbar A_{total}} \sum_{\substack{\boldsymbol{k}\in BZ,\\ \gamma,\gamma'}} \left(\frac{\partial \epsilon_{\gamma,\gamma'}}{\partial k_{a_1}}(\boldsymbol{k}) + \frac{e}{\hbar}\frac{\partial^2 \epsilon_{\gamma,\gamma'}}{\partial k_{a_1}\partial k_{a_2}}(\boldsymbol{k}) A_{a_2}(t) + ...\right) c^{\dagger}_{\boldsymbol{k},\gamma} c_{\boldsymbol{k},\gamma'}, \tag{3.5}$$

where $V_{total} = A_{total}$ is the total volume of the system (area in 2D systems). Using the time-dependent perturbation theory in the interaction representation (see appendix C), we get, for the average current density,

$$\begin{aligned}\langle J^I_{a_1}(t)\rangle =& \langle J^I_{a_1}(t)\rangle_0 + \left(-\frac{i}{\hbar}\right)\int_{t_0}^{t} dt_1 \left\langle \left[J^I_{a_1}(t), V_I(t_1)\right]\right\rangle_0 + \\ &+ \left(-\frac{i}{\hbar}\right)^2 \int_{t_0}^{t} dt_1 \int_{t_0}^{t_1} dt_2 \left\langle \left[\left[J^I_{a_1}(t), V_I(t_1)\right], V_I(t_2)\right]\right\rangle_0 + ... \quad ,\end{aligned} \tag{3.6}$$

where $\langle\ \rangle_0$ represents a thermal average over unperturbed states[1].

We now want to write (3.4) and (3.5) in the interaction picture. First, we change to the basis $|\lambda\rangle$, where H_0 is diagonal with eigenvalues $\epsilon_\lambda = \hbar\omega_\lambda$ (ω being the angular frequency), and write the creation and annihilation operators in the interaction picture as

$$c_{\boldsymbol{k},\gamma} = \sum_{\lambda} \langle\gamma|\lambda\rangle\, e^{-i\omega_\lambda(t-t_0)} c_{\boldsymbol{k},\lambda}, \quad c^{\dagger}_{\boldsymbol{k},\gamma} = \sum_{\lambda} \langle\lambda|\gamma\rangle\, e^{i\omega_\lambda(t-t_0)} c^{\dagger}_{\boldsymbol{k},\lambda}. \tag{3.7}$$

---

[1] Here, we are assuming that the initial condition of our system is a thermal state of the unperturbed Hamiltonian, H_0.

Then, we plug (3.7) into (3.4) and (3.5) and, using the closure relation, $\sum_{\gamma} |\gamma\rangle \langle\gamma| = 1$, we obtain

$$V_I(t) = \sum_{\substack{\boldsymbol{k}\in BZ,\\ \lambda,\lambda'}} \langle\lambda| \left(\frac{e}{\hbar}\frac{\partial H_0(\boldsymbol{k})}{\partial k_{a_1}} A_{a_1}(t) + \frac{1}{2!}\left(\frac{e}{\hbar}\right)^2 \frac{\partial^2 H_0(\boldsymbol{k})}{\partial k_{a_1}\partial k_{a_2}} A_{a_1}(t)A_{a_2}(t) + ... \right) |\lambda'\rangle \, e^{i\omega_{\lambda\lambda'}(t-t_0)} c^{\dagger}_{\boldsymbol{k},\lambda} c_{\boldsymbol{k},\lambda'}, \tag{3.8}$$

$$J^I_{a_1}(t) = -\frac{e}{\hbar A_{total}} \sum_{\substack{\boldsymbol{k}\in BZ,\\ \lambda,\lambda'}} \langle\lambda| \left(\frac{\partial H_0(\boldsymbol{k})}{\partial k_{a_1}} + \frac{e}{\hbar}\frac{\partial^2 H_0(\boldsymbol{k})}{\partial k_{a_1}\partial k_{a_2}} A_{a_2}(t) + ... \right) |\lambda'\rangle \, e^{i\omega_{\lambda\lambda'}(t-t_0)} c^{\dagger}_{\boldsymbol{k},\lambda} c_{\boldsymbol{k},\lambda'}, \tag{3.9}$$

where $\omega_{\lambda\lambda'} = \omega_{\lambda} - \omega_{\lambda'}$.

Equilibrium curent

Collecting the zeroth-order terms (in the fields) from the average current (3.6), we obtain the so-called equilibrium current,

$$\begin{aligned} J^0_{a_1}(t) &= -\frac{e}{\hbar A_{total}} \sum_{\substack{\boldsymbol{k}\in BZ,\\ \lambda,\lambda'}} \langle\lambda| \frac{\partial H_0(\boldsymbol{k})}{\partial k_{a_1}} |\lambda'\rangle \, e^{i\omega_{\lambda\lambda'}(t-t_0)} \left\langle c^{\dagger}_{\boldsymbol{k},\lambda} c_{\boldsymbol{k},\lambda'} \right\rangle_0 \\ &= -\frac{e}{\hbar(2\pi)^2} \sum_{\lambda} \int_{BZ} d\boldsymbol{k} \; \langle\lambda| \frac{\partial H_0(\boldsymbol{k})}{\partial k_{a_1}} |\lambda\rangle \, n_F\left(\epsilon_{\lambda}(\boldsymbol{k})\right). \end{aligned} \tag{3.10}$$

In the equation above, the thermal average was trivially computed as $\left\langle c^{\dagger}_{\boldsymbol{k},\lambda} c_{\boldsymbol{k},\lambda'} \right\rangle_0 = \delta_{\lambda,\lambda'} \; n_F\left(\epsilon_{\lambda}(\boldsymbol{k})\right)$, where n_F stands for the Fermi-Dirac function,

$$n_F\left(\epsilon\right) = \frac{1}{1 + \exp\left(\frac{\epsilon - \mu}{k_B T}\right)}, \tag{3.11}$$

in which k_B is the Boltzamnn constant, T is the absolute temperature and μ is the Fermi level.

We proceed to the derivation of an important result that will be used repeatedly in what follows. To keep the notation light, we will drop the explicit dependency on momentum in the Hamiltonian, $H_0(\boldsymbol{k}) \equiv H_0$, as we did for the states $|\boldsymbol{k},\gamma\rangle \equiv |\gamma\rangle$ or $|\boldsymbol{k},\lambda\rangle \equiv |\lambda\rangle$. We rewrite the average of the Hamiltonian's derivative as

$$\begin{aligned} \langle\lambda| \frac{\partial H_0}{\partial k_a} |\lambda'\rangle &= \sum_{\lambda_1} \langle\lambda| \frac{\partial \left(H_0 \left|\lambda_1\right\rangle \left\langle\lambda_1\right|\right)}{\partial k_a} |\lambda'\rangle = \sum_{\lambda_1} \langle\lambda| \frac{\partial \left(\epsilon_{\lambda_1} \left|\lambda_1\right\rangle \left\langle\lambda_1\right|\right)}{\partial k_a} |\lambda'\rangle \\ &= \sum_{\lambda_1} \langle\lambda| \left(\frac{\partial \epsilon_{\lambda_1}}{\partial k_a} \left|\lambda_1\right\rangle \left\langle\lambda_1\right| \; + \; \epsilon_{\lambda_1} \frac{\partial \left|\lambda_1\right\rangle}{\partial k_a} \left\langle\lambda_1\right| \; + \; \epsilon_{\lambda_1} \left|\lambda_1\right\rangle \frac{\partial \left\langle\lambda_1\right|}{\partial k_a} \right) |\lambda'\rangle \\ &= \frac{\partial \epsilon_{\lambda}}{\partial k_a} \delta_{\lambda,\lambda'} \; + \; \epsilon_{\lambda'} \left\langle\lambda|\partial_{k_a}\lambda'\right\rangle \; + \; \epsilon_{\lambda} \left\langle\partial_{k_a}\lambda|\lambda'\right\rangle \\ &= \frac{\partial \epsilon_{\lambda}}{\partial k_a} \delta_{\lambda,\lambda'} \; + \; \left(\epsilon_{\lambda'} - \epsilon_{\lambda}\right) \left\langle\lambda|\partial_{k_a}\lambda'\right\rangle, \end{aligned} \tag{3.12}$$

where, in the last step, we used $\frac{\partial}{\partial k_a} \left\langle\lambda|\lambda'\right\rangle \equiv \partial_{k_a} \left\langle\lambda|\lambda'\right\rangle = 0 \Leftrightarrow \left\langle\partial_{k_a}\lambda|\lambda'\right\rangle = -\left\langle\lambda|\partial_{k_a}\lambda'\right\rangle$.

Using this last result, the equilibrium current becomes

$$J^0_{a_1}(t) = -\frac{e}{\hbar(2\pi)^2}\sum_{\lambda}\int_{BZ} d\boldsymbol{k}\ \frac{\partial\epsilon_\lambda}{\partial k_{a_1}} n_F\left(\epsilon_\lambda\right). \tag{3.13}$$

Taking into account the time inversion symmetry in reciprocal space, $\epsilon_\lambda(-\boldsymbol{k}) = \epsilon_\lambda(\boldsymbol{k})$, and the fact that the integral is over a BZ that is symmetric under the inversion of $\boldsymbol{k}$, we show that the equilibrium current is zero, $J^0_{a_1}(t) = 0$. We point out that, even in our model for the tBLG, time inversion symmetry is not broken: we can explicitly see that, for every point $\boldsymbol{q}$ in the moiré BZ centered around K ($\boldsymbol{k} = K + \boldsymbol{q}$), we have a completely equivalent point in $-\boldsymbol{k} = -K - \boldsymbol{q}$, which corresponds to a point $-\boldsymbol{q}$ in the moiré BZ centered around $K' = -K$.

Linear response current and conductivity

Now, we collect the first order terms, which lead to the following linear response current:

$$\begin{aligned} J^1_{a_1}(t) =& -\frac{e^2}{\hbar^2 A_{total}}\sum_{\substack{\boldsymbol{k}\in BZ,\\ \lambda,\lambda'}} \langle\lambda|\,\frac{\partial^2 H_0}{\partial k_{a_1}\partial k_{a_2}}\,|\lambda'\rangle\, A_{a_2}(t) e^{i\omega_{\lambda\lambda'}(t-t_0)}\,\langle c^\dagger_{\boldsymbol{k},\lambda} c_{\boldsymbol{k},\lambda'}\rangle_0 + \\ &+ \frac{ie^2}{\hbar^3 A_{total}}\sum_{\substack{\boldsymbol{k}\in BZ,\\ \lambda_1,\lambda_2}}\sum_{\substack{\boldsymbol{k'}\in BZ,\\ \lambda_3,\lambda_4}} \langle\lambda_1|\,\frac{\partial H_0}{\partial k_{a_1}}\,|\lambda_2\rangle\,\langle\lambda_3|\,\frac{\partial H_0}{\partial k'_{a_2}}\,|\lambda_4\rangle\,\left\langle\left[c^\dagger_{\boldsymbol{k},\lambda_1} c_{\boldsymbol{k},\lambda_2}\ ,\ c^\dagger_{\boldsymbol{k'},\lambda_3} c_{\boldsymbol{k'},\lambda_4}\right]\right\rangle_0 \times \\ &\times \int_{t_0}^{t} dt_1\ e^{i\omega_{\lambda_1\lambda_2}(t-t_0)} e^{i\omega_{\lambda_3\lambda_4}(t_1-t_0)} A_{a_2}(t_1). \end{aligned} \tag{3.14}$$

Using the fermionic commutation relations, we can solve

$$\begin{aligned} \left\langle\left[c^\dagger_{\boldsymbol{k},\lambda_1} c_{\boldsymbol{k},\lambda_2}\ ,\ c^\dagger_{\boldsymbol{k'},\lambda_3} c_{\boldsymbol{k'},\lambda_4}\right]\right\rangle_0 &= \langle c^\dagger_{\boldsymbol{k},\lambda_1} c_{\boldsymbol{k},\lambda_2} c^\dagger_{\boldsymbol{k'},\lambda_3} c_{\boldsymbol{k'},\lambda_4}\rangle_0 - \langle c^\dagger_{\boldsymbol{k'},\lambda_3} c_{\boldsymbol{k'},\lambda_4} c^\dagger_{\boldsymbol{k},\lambda_1} c_{\boldsymbol{k},\lambda_2}\rangle_0 \\ &= \langle c^\dagger_{\boldsymbol{k},\lambda_1} c_{\boldsymbol{k},\lambda_2} c^\dagger_{\boldsymbol{k'},\lambda_3} c_{\boldsymbol{k'},\lambda_4}\rangle_0 - \langle c^\dagger_{\boldsymbol{k},\lambda_1} c^\dagger_{\boldsymbol{k'},\lambda_3} c_{\boldsymbol{k'},\lambda_4} c_{\boldsymbol{k},\lambda_2}\rangle_0 - \delta_{\boldsymbol{k},\boldsymbol{k'}}\delta_{\lambda_1,\lambda_4}\,\langle c^\dagger_{\boldsymbol{k'},\lambda_3} c_{\boldsymbol{k},\lambda_2}\rangle_0 \\ &= -\delta_{\boldsymbol{k},\boldsymbol{k'}}\delta_{\lambda_1,\lambda_4}\,\langle c^\dagger_{\boldsymbol{k'},\lambda_3} c_{\boldsymbol{k},\lambda_2}\rangle_0 + \delta_{\boldsymbol{k},\boldsymbol{k'}}\delta_{\lambda_2,\lambda_3}\,\langle c^\dagger_{\boldsymbol{k},\lambda_1} c_{\boldsymbol{k'},\lambda_4}\rangle_0 \\ &= \delta_{\boldsymbol{k},\boldsymbol{k'}}\delta_{\lambda_1,\lambda_4}\delta_{\lambda_2,\lambda_3}\left(n_F(\epsilon_{\lambda_1}) - n_F(\epsilon_{\lambda_2})\right), \end{aligned} \tag{3.15}$$

and use this to simplify

$$\begin{aligned} J^1_{a_1}(t) =& -\frac{e^2}{\hbar^2 A_{total}}\sum_{\boldsymbol{k}\in BZ,\lambda} \langle\lambda|\,\frac{\partial^2 H_0}{\partial k_{a_1}\partial k_{a_2}}\,|\lambda\rangle\, n_F(\epsilon_\lambda) A_{a_2}(t) + \\ &+ \frac{ie^2}{\hbar^3 A_{total}}\sum_{\substack{\boldsymbol{k}\in BZ,\\ \lambda_1,\lambda_2}} \langle\lambda_1|\,\frac{\partial H_0}{\partial k_{a_1}}\,|\lambda_2\rangle\,\langle\lambda_2|\,\frac{\partial H_0}{\partial k_{a_2}}\,|\lambda_1\rangle\left(n_F(\epsilon_{\lambda_1}) - n_F(\epsilon_{\lambda_2})\right)\int_{t_0}^{t} dt_1\ e^{i\omega_{\lambda_1\lambda_2}(t-t_1)} A_{a_2}(t_1). \end{aligned} \tag{3.16}$$

At this point, we make a FT to the magnetic vector potential,

$$A_a(t) = \int_{\mathbb{R}} \frac{d\omega}{2\pi} A_a(\omega) e^{-i\omega t}, \tag{3.17}$$

and use the relation between the Fourier amplitude of the magnetic vector potential, $A_a(\omega)$, and the Fourier amplitude of the electric field, $E_a(\omega)$,

$$E_a(t) = -\frac{dA_a(t)}{dt} \Rightarrow A_a(\omega) = \frac{E_a(\omega)}{i\omega}, \tag{3.18}$$

to obtain

$$A_a(t) = \int_{\mathbb{R}} \frac{d\omega}{2\pi} \frac{E_a(\omega)}{i\omega} e^{-i\omega t}, \tag{3.19}$$

where, in the adiabatic regime, we make $\omega \to \omega + i\gamma,\ \gamma \to 0^+$, meaning that we switch on the electromagnetic fields very slowly.

Substituting (3.19) into (3.16), we get

$$\begin{aligned} J^1_{a_1}(t) = & \int_{\mathbb{R}} \frac{d\omega}{2\pi} \left(\frac{e^2}{\hbar^2 A_{total}} \sum_{\boldsymbol{k} \in BZ, \lambda} \langle \lambda | \frac{\partial^2 H_0}{\partial k_{a_1} \partial k_{a_2}} | \lambda \rangle \frac{i n_F(\epsilon_\lambda)}{\omega} \right) E_{a_2}(\omega) e^{-i\omega t} + \\ & + \frac{ie^2}{\hbar^3 A_{total}} \sum_{\substack{\boldsymbol{k} \in BZ, \\ \lambda_1, \lambda_2}} \langle \lambda_1 | \frac{\partial H_0}{\partial k_{a_1}} | \lambda_2 \rangle \langle \lambda_2 | \frac{\partial H_0}{\partial k_{a_2}} | \lambda_1 \rangle \left(n_F(\epsilon_{\lambda_1}) - n_F(\epsilon_{\lambda_2}) \right) \times \\ & \times \int_{t_0}^{t} dt_1 \; e^{i\omega_{\lambda_1 \lambda_2}(t - t_1)} \int_{\mathbb{R}} \frac{d\omega}{2\pi} \frac{E_{a_2}(\omega)}{i\omega} e^{-i\omega t_1}. \end{aligned} \tag{3.20}$$

We can compute the integral in time,

$$\int_{t_0}^{t} dt_1 \; e^{i\omega_{\lambda_1 \lambda_2}(t - t_1)} e^{-i\omega t_1} = e^{i\omega_{\lambda_1 \lambda_2} t} \int_{t_0}^{t} dt_1 \; e^{-i(\omega_{\lambda_1 \lambda_2} + \omega) t_1} = \frac{i e^{-i\omega t}}{\omega_{\lambda_1 \lambda_2} + \omega} + \cancelto{}{\ldots}, \tag{3.21}$$

where we eliminated the last the term by making $t_0 \to -\infty$, which means that we have waited long enough for the transient terms to be negligible. Using this result, we simplify the linear response current expression into

$$\begin{aligned} J^1_{a_1}(t) = & \int_{\mathbb{R}} \frac{d\omega}{2\pi} \left(\frac{e^2}{\hbar^2 A_{total}} \sum_{\boldsymbol{k} \in BZ, \lambda} \langle \lambda | \frac{\partial^2 H_0}{\partial k_{a_1} \partial k_{a_2}} | \lambda \rangle \frac{i n_F(\epsilon_\lambda)}{\omega} \right) E_{a_2}(\omega) e^{-i\omega t} + \\ & + \int_{\mathbb{R}} \frac{d\omega}{2\pi} \left(\frac{e^2}{\hbar^3 A_{total}} \sum_{\substack{\boldsymbol{k} \in BZ, \\ \lambda_1, \lambda_2}} \langle \lambda_1 | \frac{\partial H_0}{\partial k_{a_1}} | \lambda_2 \rangle \langle \lambda_2 | \frac{\partial H_0}{\partial k_{a_2}} | \lambda_1 \rangle \frac{i \left(n_F(\epsilon_{\lambda_1}) - n_F(\epsilon_{\lambda_2}) \right)}{\omega (\omega_{\lambda_1 \lambda_2} + \omega)} \right) E_{a_2}(\omega) e^{-i\omega t}. \end{aligned} \tag{3.22}$$

Taking a closer look at the last expression, we identify the conductivity (rank-2) tensor, σ, which leads to the current that arises in response to an electric field ($\boldsymbol{J} = \sigma \boldsymbol{E}$ in matrix form), as

$$\begin{aligned} \sigma_{a_1 a_2}(\omega) = & \frac{ie^2}{\hbar^2 A_{total}} \sum_{\boldsymbol{k} \in BZ, \lambda_1} \left(\langle \lambda_1 | \frac{\partial^2 H_0}{\partial k_{a_1} \partial k_{a_2}} | \lambda_1 \rangle \frac{n^F_{\lambda_1}}{\omega} + \frac{1}{\hbar} \sum_{\lambda_2} \langle \lambda_1 | \frac{\partial H_0}{\partial k_{a_1}} | \lambda_2 \rangle \langle \lambda_2 | \frac{\partial H_0}{\partial k_{a_2}} | \lambda_1 \rangle \frac{n^F_{\lambda_1} - n^F_{\lambda_2}}{\omega(\omega_{\lambda_1 \lambda_2} + \omega)} \right) \\ = & \frac{i4\sigma_0}{N_1 N_2 A_{u.c.}} \sum_{\boldsymbol{k} \in BZ, \lambda_1} \left(\langle \lambda_1 | \frac{\partial^2 H_0}{\partial k_{a_1} \partial k_{a_2}} | \lambda_1 \rangle \frac{n^F_{\lambda_1}}{\hbar\omega} + \sum_{\lambda_2 \neq \lambda_1} \langle \lambda_1 | \frac{\partial H_0}{\partial k_{a_1}} | \lambda_2 \rangle \langle \lambda_2 | \frac{\partial H_0}{\partial k_{a_2}} | \lambda_1 \rangle \frac{n^F_{\lambda_1} - n^F_{\lambda_2}}{\hbar\omega(\epsilon_{\lambda_1 \lambda_2} + \hbar\omega)} \right), \end{aligned} \tag{3.23}$$

where $\sigma_0 = e^2/(4\hbar)$ is the graphene universal conductivity and $n_F(\epsilon_\lambda) \equiv n_\lambda^F$. Once again, we used PBC to discretize the sum in momentum in $N = N_1 N_2$ terms. At last, we recall that we have ommited the sum in spin; therefore, since we do not have any spin dependency, we may add a factor of 2 to the conductivity,

$$\sigma_{a_1a_2}(\omega) = \frac{8\sigma_0 i}{NA_{u.c.}} \sum_{\substack{\boldsymbol{k}\in BZ,\\ \lambda_1}} \left(\langle\lambda_1| \frac{\partial^2 H_0}{\partial k_{a_1}\partial k_{a_2}} |\lambda_1\rangle \frac{n_{\lambda_1}^F}{\hbar\omega} + \sum_{\lambda_2\neq\lambda_1} \langle\lambda_1| \frac{\partial H_0}{\partial k_{a_1}} |\lambda_2\rangle \langle\lambda_2| \frac{\partial H_0}{\partial k_{a_2}} |\lambda_1\rangle \frac{n_{\lambda_1}^F - n_{\lambda_2}^F}{\hbar\omega(\epsilon_{\lambda_1\lambda_2} + \hbar\omega)} \right). \tag{3.24}$$

Drude and regular conductivity

It is usual to split the conductivity in a Drude contribution plus a regular term. Making

$$\frac{1}{\hbar\omega(\epsilon_{\lambda_1\lambda_2} + \hbar\omega)} = \frac{1}{\hbar\omega\ \epsilon_{\lambda_1\lambda_2}} - \frac{1}{\epsilon_{\lambda_1\lambda_2}(\epsilon_{\lambda_1\lambda_2} + \hbar\omega)}, \quad \epsilon_{\lambda_1\lambda_2} \neq 0, \tag{3.25}$$

we write the Drude conductivity as

$$\sigma_{a_1a_2}^D(\omega) = \frac{8\sigma_0 i}{NA_{u.c.}\hbar\omega} \sum_{\boldsymbol{k}\in BZ,\lambda_1} \left(\langle\lambda_1| \frac{\partial^2 H_0}{\partial k_{a_1}\partial k_{a_2}} |\lambda_1\rangle n_{\lambda_1}^F + \sum_{\lambda_2\neq\lambda_1} \langle\lambda_1| \frac{\partial H_0}{\partial k_{a_1}} |\lambda_2\rangle \langle\lambda_2| \frac{\partial H_0}{\partial k_{a_2}} |\lambda_1\rangle \frac{n_{\lambda_1}^F - n_{\lambda_2}^F}{\epsilon_{\lambda_1\lambda_2}} \right), \tag{3.26}$$

and the regular conductivity as

$$\sigma_{a_1a_2}^{reg}(\omega) = \frac{-8\sigma_0 i}{NA_{u.c.}} \sum_{\substack{\boldsymbol{k}\in BZ,\\ \lambda_1,\lambda_2\neq\lambda_1}} \langle\lambda_1| \frac{\partial H_0}{\partial k_{a_1}} |\lambda_2\rangle \langle\lambda_2| \frac{\partial H_0}{\partial k_{a_2}} |\lambda_1\rangle \frac{n_{\lambda_1}^F - n_{\lambda_2}^F}{\epsilon_{\lambda_1\lambda_2}(\epsilon_{\lambda_1\lambda_2} + \hbar\omega)}. \tag{3.27}$$

Using the mathematical relation,

$$\frac{1}{x \pm i\eta} = P\left(\frac{1}{x}\right) \mp i\pi\delta(x), \quad \eta \to 0^+, \tag{3.28}$$

where P stands for the Cauchy principal value, we can rewrite the expression for the Drude conductivity in the adiabatic regime as

$$\sigma_{a_1a_2}^D(\omega) = \frac{i}{\pi}\frac{D_{a_1a_2}}{\hbar\omega + i\Gamma} \to D_{a_1a_2}\left(\delta(\hbar\omega) + P\left(\frac{i}{\pi\hbar\omega}\right)\right), \tag{3.29}$$

where $\Gamma = \hbar\gamma \to 0^+$ and the Drude weight is given by

$$D_{a_1a_2} = \frac{8\pi\sigma_0}{NA_{u.c.}} \sum_{\boldsymbol{k}\in BZ,\lambda_1} \left(\langle\lambda_1| \frac{\partial^2 H_0}{\partial k_{a_1}\partial k_{a_2}} |\lambda_1\rangle n_{\lambda_1}^F + \sum_{\lambda_2\neq\lambda_1} \langle\lambda_1| \frac{\partial H_0}{\partial k_{a_1}} |\lambda_2\rangle \langle\lambda_2| \frac{\partial H_0}{\partial k_{a_2}} |\lambda_1\rangle \frac{n_{\lambda_1}^F - n_{\lambda_2}^F}{\epsilon_{\lambda_1\lambda_2}} \right). \tag{3.30}$$

We can thus see that the real part of σ^D corresponds to the typical Drude peak for $\omega = 0$, characteristic of metals [56]. Therefore, we interpret this contribution as an intraband term (where momentum is not conserved), which reflects the response of the electrons to a static applied electric field. Consequently, the regular conductivity is understood as an interband term, which corresponds to electronic band transitions (within the same $\boldsymbol{k}$) with energy $\hbar\omega$, induced by an applied harmonic electric field, $\boldsymbol{E} \sim e^{-i\omega t}$. We also note that we can empirically account for disorder effects by considering a finite Γ, which is a broadening parameter (usually interpreted as a scattering rate) that may depend on intrinsic and extrisic aspects, such as impurities, electron-electron interactions and substrate, for example.

At this point, we see that we already have expressions to compute the conductivity. Let us clarify the numerical computations by expressing all the dependencies that were ommited before. For the Drude conductivity, we compute the Drude weight by (3.30),

$$\begin{aligned} D_{a_1a_2} =& \frac{8\pi\sigma_0}{NA_{u.c.}} \sum_{\boldsymbol{k}\in BZ,\lambda_1} \Bigg[\langle\lambda_1,\boldsymbol{k}| \frac{\partial^2 H_0(\boldsymbol{k})}{\partial k_{a_1}\partial k_{a_2}} |\lambda_1,\boldsymbol{k}\rangle\, n_F\left(\epsilon_{\lambda_1}(\boldsymbol{k})\right) + \\ &+ \sum_{\lambda_2\neq\lambda_1} \langle\lambda_1,\boldsymbol{k}| \frac{\partial H_0(\boldsymbol{k})}{\partial k_{a_1}} |\lambda_2,\boldsymbol{k}\rangle \langle\lambda_2,\boldsymbol{k}| \frac{\partial H_0(\boldsymbol{k})}{\partial k_{a_2}} |\lambda_1,\boldsymbol{k}\rangle \frac{n_F\left(\epsilon_{\lambda_1}(\boldsymbol{k})\right) - n_F\left(\epsilon_{\lambda_2}(\boldsymbol{k})\right)}{\epsilon_{\lambda_1}(\boldsymbol{k}) - \epsilon_{\lambda_2}(\boldsymbol{k})} \Bigg], \end{aligned} \tag{3.31}$$

and then apply (3.29) with a finite Γ,

$$\sigma^D_{a_1a_2}(\omega) = \frac{i}{\pi}\frac{D_{a_1a_2}}{\hbar\omega + i\Gamma}. \tag{3.32}$$

For the regular conductivity, we use (3.27) with $\hbar\omega \to \hbar\omega + i\Gamma$,

$$\begin{aligned} \sigma^{reg}_{a_1a_2}(\omega) = \frac{-8\sigma_0 i}{NA_{u.c.}} \sum_{\substack{\boldsymbol{k}\in BZ,\\ \lambda_1,\lambda_2\neq\lambda_1}} \langle\lambda_1,\boldsymbol{k}| \frac{\partial H_0(\boldsymbol{k})}{\partial k_{a_1}} |\lambda_2,\boldsymbol{k}\rangle \langle\lambda_2,\boldsymbol{k}| \frac{\partial H_0(\boldsymbol{k})}{\partial k_{a_2}} |\lambda_1,\boldsymbol{k}\rangle \times \\ \times \frac{n_F\left(\epsilon_{\lambda_1}(\boldsymbol{k})\right) - n_F\left(\epsilon_{\lambda_2}(\boldsymbol{k})\right)}{\left[\epsilon_{\lambda_1}(\boldsymbol{k}) - \epsilon_{\lambda_2}(\boldsymbol{k})\right]\left[\epsilon_{\lambda_1}(\boldsymbol{k}) - \epsilon_{\lambda_2}(\boldsymbol{k}) + \hbar\omega + i\Gamma\right]}. \end{aligned} \tag{3.33}$$

These expressions must work when we have the complete Hamiltonian defined in the full BZ. However, for effective Hamiltonians, they might not be the most appropriate. In particular, when computing the Drude weight, we expect that all the dependency comes from the electrons near the Fermi level, which are the ones that can flow in response to the static applied electric field. Yet, this is not explicit in our expression, which indicates that there should be an underlying annulment of the other terms. For this reason, we will work the expression (3.30) into a convenient form. Regarding the regular conductivity, we observe that the real part is strongly constrained to eigenstates within $\hbar\omega$ of the Fermi level; therefore, this computation should not be problematic and we will keep this method. For the imaginary part, we see that, even for small ω, we do not have an argument to avoid a summation over all the bands; we will thus make use of the Kramers-Kronig (KK) relations to compute the imaginary part using the results obtained for the real part.

Drude weight — 2$^{\text{nd}}$ method

Here, we derive an alternative expression for computing the Drude weight. Using the result obtained in (3.12), the second term in the equation describing the Drude weight, (3.30), can be written as

$$\sum_{\lambda_1,\lambda_2\neq\lambda_1} \langle\lambda_1| \frac{\partial H_0}{\partial k_{a_1}} |\lambda_2\rangle \langle\lambda_2| \frac{\partial H_0}{\partial k_{a_2}} |\lambda_1\rangle \frac{n^F_{\lambda_1} - n^F_{\lambda_2}}{\epsilon_{\lambda_1\lambda_2}} = \sum_{\lambda_1,\lambda_2\neq\lambda_1} \langle\lambda_1| \frac{\partial H_0}{\partial k_{a_1}} |\lambda_2\rangle \langle\lambda_2|\partial_{a_2}\lambda_1\rangle\, (n^F_{\lambda_1} - n^F_{\lambda_2}). \tag{3.34}$$

Clearly, the last sum can be extended to the case where $\lambda_2 = \lambda_1$. We then proceed with the following manipulations:

$$\begin{aligned}
&\sum_{\lambda_1,\lambda_2} \langle\lambda_1| \frac{\partial H_0}{\partial k_{a_1}} |\lambda_2\rangle \langle\lambda_2|\partial_{a_2}\lambda_1\rangle \left(n^F_{\lambda_1} - n^F_{\lambda_2}\right) \\
&\quad= \sum_{\lambda_1} \langle\lambda_1| \frac{\partial H_0}{\partial k_{a_1}} |\partial_{a_2}\lambda_1\rangle\, n^F_{\lambda_1} - \sum_{\lambda_1,\lambda_2} \langle\lambda_1| \frac{\partial H_0}{\partial k_{a_1}} |\lambda_2\rangle \langle\lambda_2|\partial_{a_2}\lambda_1\rangle\, n^F_{\lambda_2} \\
&\quad= \sum_{\lambda_1} \langle\lambda_1| \frac{\partial H_0}{\partial k_{a_1}} |\partial_{a_2}\lambda_1\rangle\, n^F_{\lambda_1} + \sum_{\lambda_1,\lambda_2} \langle\lambda_1| \frac{\partial H_0}{\partial k_{a_1}} |\lambda_2\rangle \langle\partial_{a_2}\lambda_2|\lambda_1\rangle\, n^F_{\lambda_2} \\
&\quad= \sum_{\lambda_1} \langle\lambda_1| \frac{\partial H_0}{\partial k_{a_1}} |\partial_{a_2}\lambda_1\rangle\, n^F_{\lambda_1} + \sum_{\lambda_1,\lambda_2} \langle\partial_{a_2}\lambda_1|\lambda_2\rangle \langle\lambda_2| \frac{\partial H_0}{\partial k_{a_1}} |\lambda_1\rangle\, n^F_{\lambda_1} \\
&\quad= \sum_{\lambda_1} \left(\langle\lambda_1| \frac{\partial H_0}{\partial k_{a_1}} |\partial_{a_2}\lambda_1\rangle + \langle\partial_{a_2}\lambda_1|\frac{\partial H_0}{\partial k_{a_1}}|\lambda_1\rangle \right) n^F_{\lambda_1}. \qquad (3.35)
\end{aligned}$$

Collecting all terms, the Drude weight yields:

$$\begin{aligned}
D_{a_1a_2} &= \frac{8\pi\sigma_0}{NA_{u.c.}} \sum_{\boldsymbol{k}\in BZ,\lambda_1} \left(\langle\lambda_1| \frac{\partial^2 H_0}{\partial k_{a_1}\partial k_{a_2}} |\lambda_1\rangle + \langle\lambda_1| \frac{\partial H_0}{\partial k_{a_1}} |\partial_{a_2}\lambda_1\rangle + \langle\partial_{a_2}\lambda_1|\frac{\partial H_0}{\partial k_{a_1}}|\lambda_1\rangle \right) n^F_{\lambda_1} \\
&= \frac{8\pi\sigma_0}{NA_{u.c.}} \sum_{\boldsymbol{k}\in BZ,\lambda_1} n^F_{\lambda_1} \frac{\partial}{\partial k_{a_2}} \langle\lambda_1| \frac{\partial H_0}{\partial k_{a_1}} |\lambda_1\rangle \\
&= \frac{8\pi\sigma_0}{NA_{u.c.}} \sum_{\boldsymbol{k}\in BZ,\lambda_1} \frac{\partial^2 \epsilon_{\lambda_1}}{\partial k_{a_1}\partial k_{a_2}} n^F_{\lambda_1} \\
&= \frac{8\pi\sigma_0}{NA_{u.c.}} \sum_{\boldsymbol{k}\in BZ,\lambda_1} \left(\frac{\partial}{\partial k_{a_1}} \left(\frac{\partial \epsilon_{\lambda_1}}{\partial k_{a_2}} n^F_{\lambda_1} \right) - \frac{\partial \epsilon_{\lambda_1}}{\partial k_{a_2}} \frac{\partial n^F_{\lambda_1}}{\partial k_{a_1}} \right). \qquad (3.36)
\end{aligned}$$

The first term is shown to be null, making use of time inversion symmetry,

$$\sum_{\boldsymbol{k}\in BZ,\lambda_1} \frac{\partial}{\partial k_{a_1}} \left(\frac{\partial \epsilon_{\lambda_1}}{\partial k_{a_2}} n^F_{\lambda_1} \right) = \frac{\partial}{\partial k_{a_1}} \left(\sum_{\boldsymbol{k}\in BZ,\lambda_1} \frac{\partial \epsilon_{\lambda_1}}{\partial k_{a_2}} n^F_{\lambda_1} \right) = \frac{\partial}{\partial k_{a_1}} (0) = 0. \qquad (3.37)$$

The final expression therefore reads

$$\begin{aligned}
D_{a_1a_2} &= -\frac{8\pi\sigma_0}{NA_{u.c.}} \sum_{\boldsymbol{k}\in BZ,\lambda_1} \frac{\partial \epsilon_{\lambda_1}}{\partial k_{a_2}} \frac{\partial n^F_{\lambda_1}}{\partial k_{a_1}} \\
&= -\frac{8\pi\sigma_0}{NA_{u.c.}} \sum_{\boldsymbol{k}\in BZ,\lambda_1} \frac{\partial \epsilon_{\lambda_1}}{\partial k_{a_2}} \frac{\partial \epsilon_{\lambda_1}}{\partial k_{a_1}} \frac{\partial n^F_{\lambda_1}}{\partial \epsilon_{\lambda_1}} \\
&= -\frac{8\pi\sigma_0}{NA_{u.c.}} \sum_{\boldsymbol{k}\in BZ,\lambda} \frac{\partial \epsilon_{\lambda}(\boldsymbol{k})}{\partial k_{a_1}} \frac{\partial \epsilon_{\lambda}(\boldsymbol{k})}{\partial k_{a_2}} \frac{\partial n_F(\epsilon)}{\partial \epsilon} \left(\epsilon_\lambda(\boldsymbol{k})\right). \qquad (3.38)
\end{aligned}$$

As foreseen, this expression only takes into account electrons near the Fermi level. This can be directly detected by the presence of the derivative of the Fermi-Dirac function.

Imaginary part of the regular conductivity — 2^{nd} method

The KK relations relate the real part of a response function with its imaginary part. They enable us to find one of the components if we know the other at all frequencies. In our case, we want to compute the imaginary part of the regular conductivity. The appropriate relation is [57]

$$\text{Im}\left\{\sigma^{reg}(\omega)\right\} = -\frac{2\omega}{\pi} P \int_0^{+\infty} ds \, \frac{\text{Re}\left\{\sigma^{reg}(s)\right\}}{s^2 - \omega^2}. \tag{3.39}$$

Looking at this expression, there is apparently no advantage in using this method for effective models, since the integral extends to infinity. Moreover, this integral is ill defined, since at high frequencies our continuum model for the tBLG is expected to yield a constant $\text{Re}\left\{\sigma^{reg}(\omega)\right\} = 2\sigma_0$. We can thus perform a regularization of eq. (3.39) by invoking the following property (which we verified numerically):

$$P \int_0^{+\infty} ds \frac{1}{s^2 - \omega^2} = 0. \tag{3.40}$$

The final regularized definition then reads

$$\text{Im}\left\{\sigma^{reg}(\omega)\right\} = -\frac{2\omega}{\pi} P \int_0^{+\infty} ds \, \frac{\text{Re}\left\{\sigma^{reg}(s)\right\} - 2\sigma_0}{s^2 - \omega^2}, \tag{3.41}$$

which we can now evaluate by introducing a finite cutoff Λ for which $\text{Re}\left\{\sigma^{reg}(\Lambda)\right\} \simeq 2\sigma_0$. The fact that our model yields a constant for high frequencies is not problematic in the range of frequencies that we are interested in.

3.1.2 Results for single layer graphene

Drude weight

The results for the Drude weight in SLG are presented in fig. 3.1. We stress that both methods —eqs. (3.31) and (3.38)— yielded the same results and that they were isotropic, i.e., $D_{xx} = D_{yy}$, $D_{xy} = 0$. The low-energy results for $D_{xx} = D_{yy} \equiv D$ are in agreement with the theoretical predictions for the Drude conductivity at $T = 0$K [19, 58],

$$\sigma^D(\omega) = 4\sigma_0 \frac{i}{\pi} \frac{\mu}{\hbar\omega + i\Gamma}. \tag{3.42}$$

From this expression, we recognize the Drude weight as $D/\sigma_0 = 4\mu$, which we compare to the zoomed plot in fig. 3.1(a). The smoothed behavior near $\mu \sim \mu_0 = 0$ is explained by the finite temperature: we only have electrons available for the transport due to thermal activation.

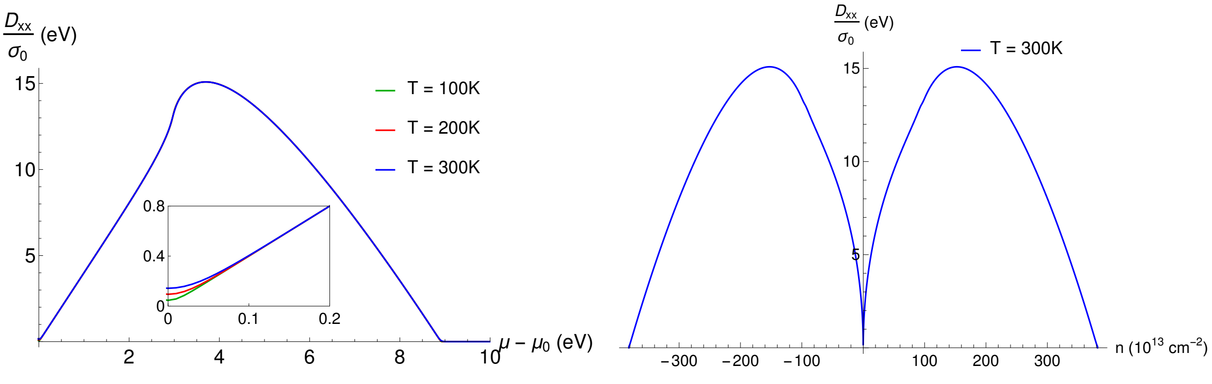

(a) (b)

Figure 3.1: Drude weight results for SLG: (a) as a function of the Fermi level; (b) as a function of the carrier density.

Regular conductivity

In fig. 3.2, we present the results for the regular conductivity in SLG. Here, and in what follows, we set $\Gamma = 16$meV in agreement with ref. [35]. Once again, both methods —eq. (3.33) for both real and imaginary parts and eq. (3.33) for the real part along with eq. (3.41) for the imaginary part— yielded the same results and we obtained an isotropic conductivity, $\sigma_{xx}^{reg} = \sigma_{yy}^{reg}$, $\sigma_{xy}^{reg} = 0$. The visible peak for $\hbar\omega = 2t \simeq 6$eV in fig. 3.2(a) corresponds to electronic transitions from the van Hove singularity of the valence band to the van Hove singularity in the conduction band, as we depict in fig. 3.3(a). These transitions are enhanced because there is a peak in the number of electrons that can occupy the initial and final energy states. Regarding fig. 3.2(b), we also infer that transitions with $\hbar\omega < 2\mu$ are forbidden, which has been observed experimentally [59]. The explanation is sketched in fig. 3.3(b). When we increase the Fermi level up to $\mu > \mu_0$, states with $E < \mu$ become occupied. Therefore, transitions for those states are blocked due to the Pauli exclusion principle. Since we have particle-hole symmetry, we conclude that we can only have transistions when $\hbar\omega > 2\mu$. The increase in temperature smooths out this behavior.

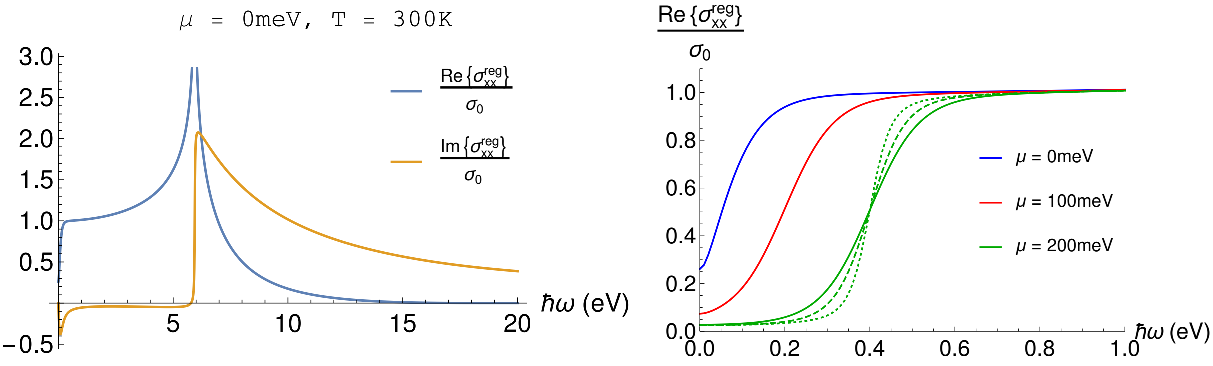

(a) (b)

Figure 3.2: (a) and (b) show the regular conductivity results for SLG. In (b), the dotted line corresponds to $T = 100$K, the dashed line to $T = 200$K and the solid lines to $T = 300$K.

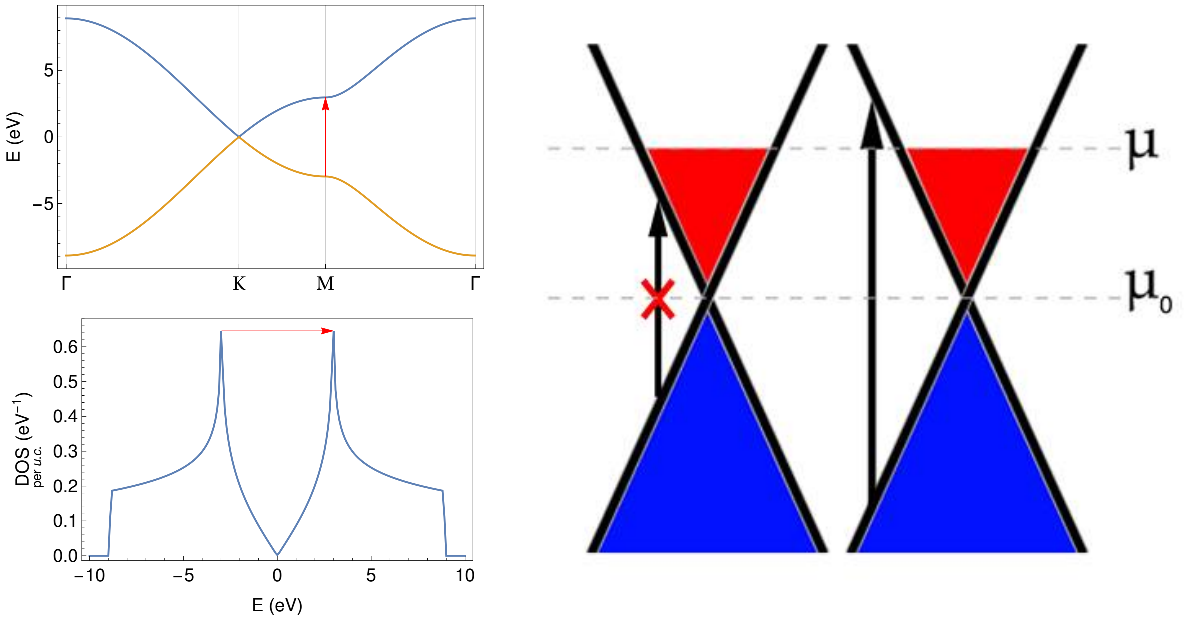

(a) Dominant transition.

(b) Forbidden and allowed transitions.

Figure 3.3: Interband transitions in SLG.

3.1.3 Results for twisted bilayer graphene

Drude weight

Some of the results obtained for the Drude weight in tBLG systems are summarized in fig. 3.4. We stress that only the 2$^{\text{nd}}$ method worked well for these computations. We believe it happened because we are working with an effective Hamiltonian, as discussed before. We also point out that the 1$^{\text{st}}$ method depends explicitly on second derivatives of the Hamiltonian and, since we used the Dirac approximation for the diagonal entries and the hopping terms were modeled as constant, these second derivatives are identically null for the tBLG. Similarly to what we saw for the SLG, we observe symmetric results for electron or hole doping; this reflects the apparent symmetry in positive and negative bands discussed in section 2.3.7. By looking at fig. 3.4(a), along with fig. 2.13(a), we conclude that the Drude weight curve changes drastically (compared with SLG or decoupled BLG) when we cross the van Hove singularities. This tendency coincides with what was found in ref. [34]. The effect of increasing the temperature is again the smoothening of this behavior (fig. 3.4(b)).

In fig. 3.5(a), we show recent experimental results for the Drude conductivity in tBLG, obtained in ref. [31]. We observe the expected symmetry for doping with electrons and holes. Moreover, since for $\omega = 0$ the conductivity is dominated by the Drude contribution, we may compare the experimental results with the theoretical calculations from fig. 3.4(b). We note the need of including the disorder broadening Γ in order to obtain a quantitative agreement on the order of magnitude with the experiment. In addition, we see that the experimental drop in the conductivity, at $n \sim 7.5 \times 10^{12}\text{cm}^{-2}$, is in agreement with what our model predicts. These insulating states are interpreted as the gaps occuring at the point Γ_m in the electronic spectrum (fig. 3.5(b)). However, we immediately verify that the insulating behavior is much

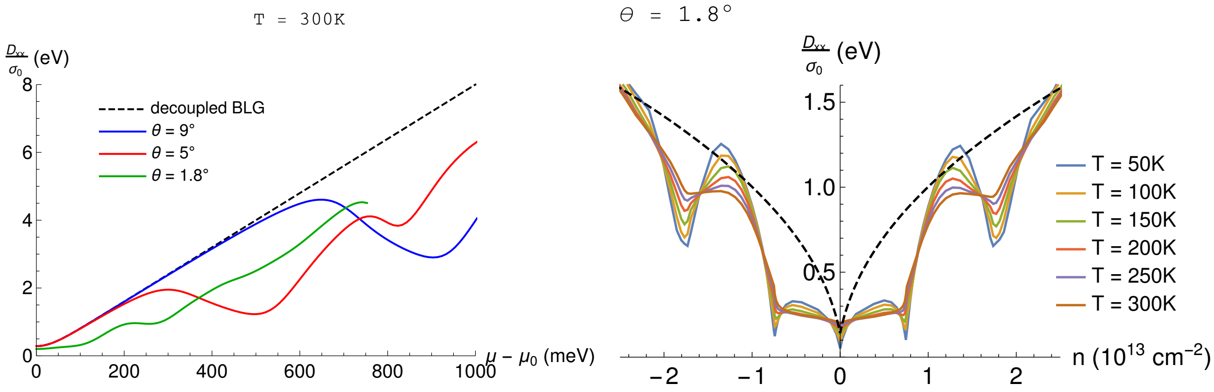

(a) (b)

Figure 3.4: Drude weight results for tBLG (2^{nd} method): (a) as a function of the Fermi level, for different angles; (b) as a function of the carrier density, for different temperatures. The outcomes were again isotropic. In (b), the black dashed line is for decoupled BLG at $T = 300\text{K}$. The results for decoupled BLG (tBLG continuum model with $t_\perp = 0$) were verified to match the results for the SLG, multiplied by 2.

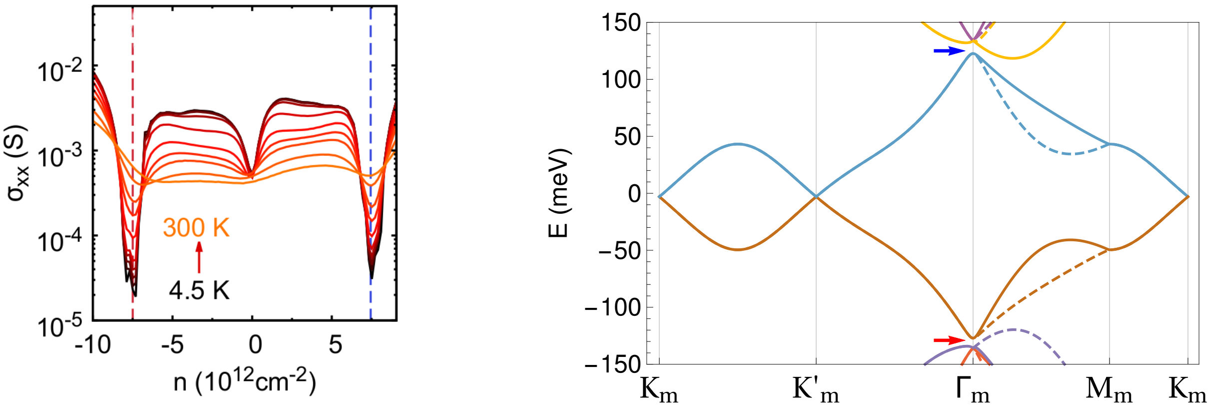

(a) (b)

Figure 3.5: tBLG with $\theta = 1.8°$: (a) experimental results for the Drude conductivity, source: ref. [31]; (b) band structure.

more pronnounced in the experimental results. In the work done in ref. [31], the authors estimated a band gap of $50 - 60$meV, which is much larger than what we observe in the electronic spectrum. This motivates some of the work that will be done in chapter 4. In particular, the goal is to compute the band renormalization due to electron-electron interactions and check if it is responsible, to some extent, for the enhanced gaps around ± 125meV in this system. Finally, we also note the disagreement between the experimental results and the theory near the Dirac point (which corresponds to $n = 0$), in particular the fact that the conductivity is not very much sensitive to T below some value T_{max} (see fig. 3.5(a)). This is an expected result observed in graphene and the explanation is that it occurs due to inhomogeneities in the system (extrinsic disorder, ripples, etc...), which basically make the Dirac point inacessible [60].

Regular conductivity

In figs. 3.6 and 3.7, we show representative results that allow us to analyze the regular conductivity in tBLG systems. All conductivity results obtained were isotropic. Before discussing these results, we

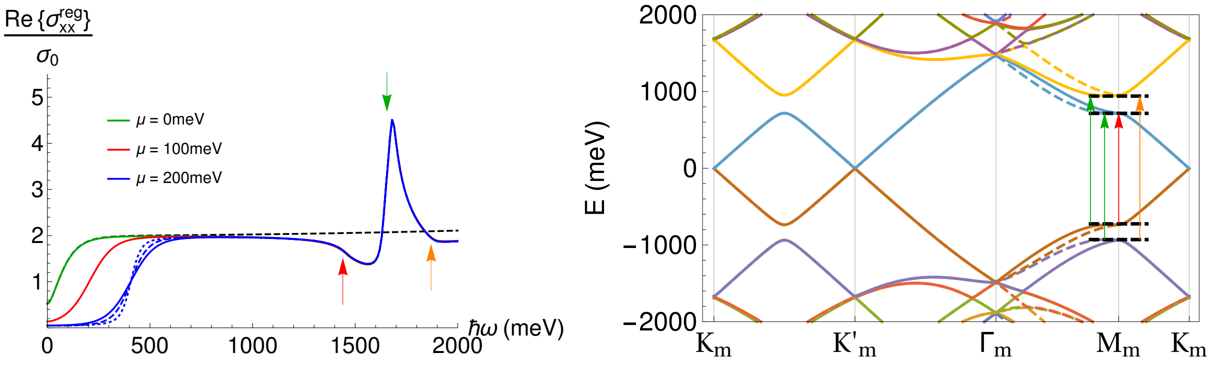

(a) (b)

Figure 3.6: tBLG with $\theta = 9^\circ$: (a) real part of the regular conductivity; (b) electronic spectrum. In (a), the dotted blue line corresponds to $T = 100$K, the dashed blue line to $T = 200$K and the solid lines to $T = 300$K; the black dashed line is for decoupled tBLG (or 2×SLG) at $T = 300$K and $\mu = 0$.

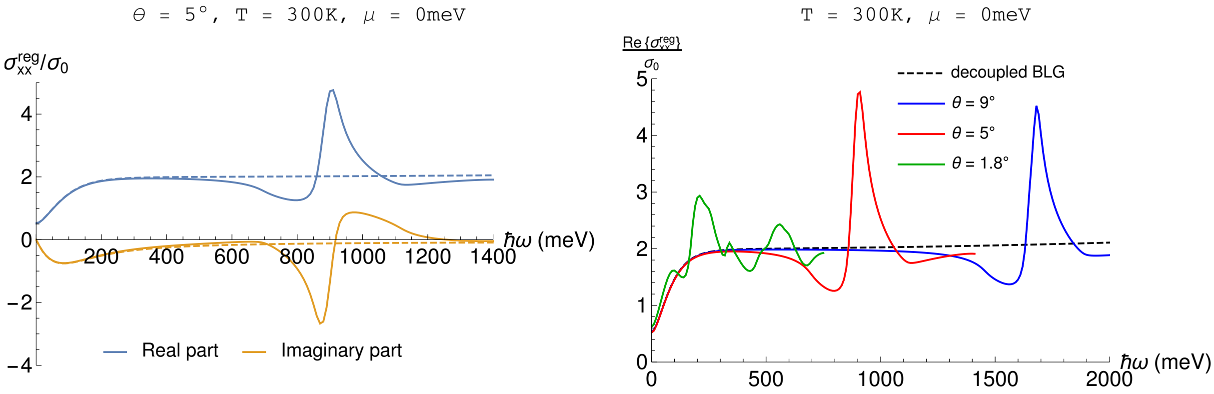

(a) (b)

Figure 3.7: Regular conductivity results for tBLG. In (a) and (b), the dashed lines are for decoupled BLG or 2×SLG.

give a word about the numerical implementation of the real part (the imaginary part is straightforwardly computed from the real part by using the regularized KK relation). In contrast with the other calculations, where we only needed to consider bands with $|E| \lesssim 1$eV (which are well described by the model), in this case we see that, for a given μ and for a given ω, all bands with energy respecting $|E - \mu| \lesssim \hbar\omega$ contribute. Therefore, depending on the Fermi level μ and, most importantly, on the energy $\hbar\omega$ of the interband transition that we want to capture, we may need to consider higher energy bands that are not well described by the model. Still, this does not constitute a big concern because these bands lead to the well established constant value $2\sigma_0$, typical of the Dirac cone approximation.

Looking at fig. 3.6(a), we first notice the already discussed dependency on both the Fermi level and temperature. In addition, we observe a low-energy peak (marked with a green arrow), which we interpret as the dominant transitions shown in fig. 3.6(b). Notice that there are other transitions (red and orange arrows) which we would expect to be dominant, since they connect different van Hove singularities; however, these transitions are optically inactive, in agreement with what was found in refs. [32, 33]. This optical selection rule occurs due to a symmetry in the effective Hamiltonian which makes the matrix elements from eq. (3.33) null for bands with symmetric energies and in the M_m points only [33]. From fig. 3.7(a), we highlight the fact that the results obtained for the decoupled tBLG —tBLG with a null interlayer hopping parameter, $t_\perp = 0$— match perfectly the results for 2×SLG (results for SLG, multiplied by 2). Although this was trivially expected, it was only achieved when we used the second method for computing the imaginary part of the regular conductivity; therefore, this served as a benchmark test for the validity of the computational methods. Moreover, we remark that we now have a region with a big deep on $\mathrm{Im}\left\{\sigma^{reg}(\omega)\right\}$ occuring at lower frequencies, which will be an important feature in the next section. Regarding the last figure, fig. 3.7(b), we emphasize that, for small angles, we start to lose the "signature" behavior of the curves because of the presence of multiple low-energy van Hove singularities.

3.2 Spectrum of graphene surface plasmon-polaritons

3.2.1 Dispersion relation — transverse magnetic modes

For this derivation, we will closely follow Gonçalves and Peres [19]. We consider a system consisting of a single graphene sheet cladded between two semi-infinite dielectric media, characterized by the real dielectric constants (relative permittivities) ε_1^r and ε_2^r, as depicted in fig. 3.8. We stress that, although the tBLG is not truly a 2D surface, its thickness is still negligible and we can view it as a monolayer for these purposes [2].

Let us assume a solution of Maxwell's equations in the form of a TM wave. We use the following ansatz for the electric and magnetic fields in the medium $j = 1, 2$:

$$\boldsymbol{E}_j = (E_{j,x}\hat{\boldsymbol{x}} + E_{j,z}\hat{\boldsymbol{z}})e^{iqx}e^{-\kappa_j|z|}, \quad \boldsymbol{B}_j = B_{j,y}e^{iqx}e^{-\kappa_j|z|}\hat{\boldsymbol{y}}. \tag{3.43}$$

This ansatz describes an electromagnetic wave (TM mode) which is confined to the neighborhood of the graphene sheet (with damping parameter $\kappa_j, \mathrm{Re}\left\{\kappa_j\right\} > 0$) and propagates along the $\hat{\boldsymbol{x}}$-direction. Due to translational invariance symmetry, the linear momentum along the propagation direction must be conserved, enabling us to write $q \equiv q_1 = q_2$, where $q_{1/2}$ is the momentum of the electromagnetic wave propagating in medium 1/2. Moreover, we note that we are just writting the spatial components of the fields; the time dependency, in what follows, is assumed to be of the typical harmonic form, i.e., $e^{-i\omega t}$.

We now make use of Maxwell's equations. For each one of the media, Faraday's law of induction and Ampère's law read, respectively,

$$\boldsymbol{\nabla} \times \boldsymbol{E}_j = -\frac{\partial \boldsymbol{B}_j}{\partial t}, \tag{3.44}$$

$$\boldsymbol{\nabla} \times \boldsymbol{H}_j = \boldsymbol{J}_j^f + \frac{\partial \boldsymbol{D}_j}{\partial t}. \tag{3.45}$$

Considering isotropic linear dielectric media, we can write the electric displacement as $\boldsymbol{D}_j = \varepsilon_0\varepsilon_j^r\boldsymbol{E}_j$, where ε_0 is the vacuum permittivity. Assuming isotropic linear magnetic media with unitary relative permeability, we may also write the magnetic field strength as $\boldsymbol{H}_j = \frac{\boldsymbol{B}_j}{\mu_0\mu_j^r} = \frac{\boldsymbol{B}_j}{\mu_0}$ where μ_0 is the vacuum

---

[2] Typically, the 2D nature is still predominant for less than 10 layers [61].

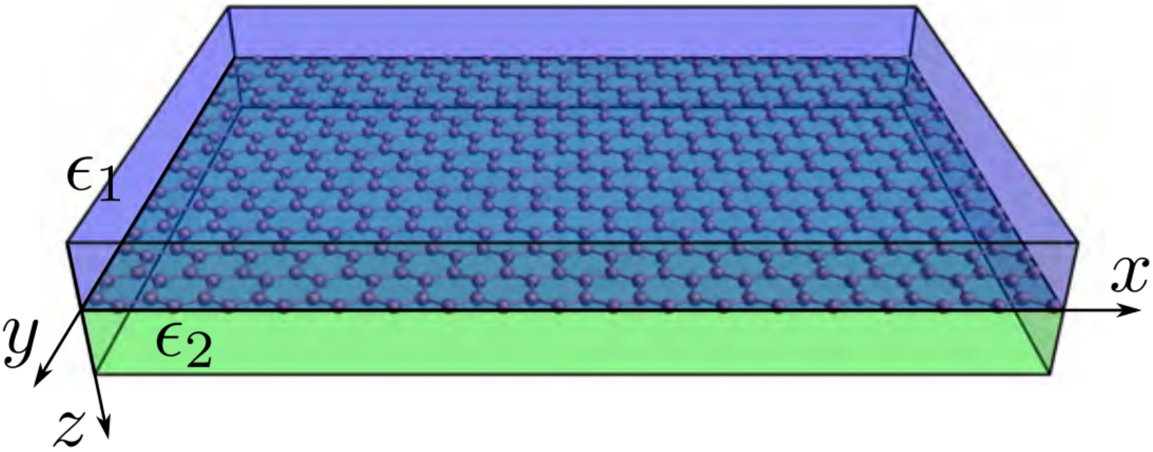

Figure 3.8: Illustration of a single graphene sheet sandwiched between two semi-infinite insulators with relative permittivities $\epsilon_i \equiv \varepsilon_i^r$ (in our notation). Medium 1 occupies the $z < 0$ half-space and medium 2 the $z > 0$; the graphene sheet is located at the $z = 0$ plane. Source: ref. [19].

permeability. Finally, if the free current density is zero, $\boldsymbol{J}_j^f = \boldsymbol{0}$, we rewrite Ampère's law as

$$\boldsymbol{\nabla} \times \boldsymbol{B}_j = \frac{\varepsilon_j^r}{c^2} \frac{\partial \boldsymbol{E}_j}{\partial t}, \tag{3.46}$$

where $c = 1/\sqrt{\mu_0 \varepsilon_0}$ is the speed of light. Introducing the fields (3.43) into (3.44) and (3.46), we obtain the following useful relations:

$$-\operatorname{sgn}(z)\kappa_j E_{j,x} - iqE_{j,z} = i\omega B_{j,y}, \tag{3.47}$$

$$\operatorname{sgn}(z)\kappa_j B_{j,y} = -i\omega \frac{\varepsilon_j^r}{c^2} E_{j,x}, \tag{3.48}$$

$$iqB_{j,y} = -i\omega \frac{\varepsilon_j^r}{c^2} E_{j,z}. \tag{3.49}$$

From these, we can deduce

$$E_{j,x} = i \operatorname{sgn}(z) \frac{\kappa_j c^2}{\omega \varepsilon_j^r} B_{j,y}, \tag{3.50}$$

$$E_{j,z} = -\frac{qc^2}{\omega \varepsilon_j^r} B_{j,y}, \tag{3.51}$$

$$\kappa_j^2 = q^2 - \frac{\omega^2 \varepsilon_j^r}{c^2}. \tag{3.52}$$

Within the linear response regime, the boundary conditions linking the electromagnetic fields at $z = 0$ read

$$E_{1,x}(x, z = 0) = E_{2,x}(x, z = 0), \tag{3.53}$$

$$B_{1,y}(x, z = 0) - B_{2,y}(x, z = 0) = \mu_0 J_x(x) = \mu_0 \sigma_{xx} E_{2,x}(x, z = 0), \tag{3.54}$$

which assure the continuity of the tangential component of the electric field and the discontinuity of the tangential component of the magnetic field across the interface. We emphasize that the conductivity of graphene is taken into account in the boundary condition only. For unstrained graphene (and particularly for the systems in focus), graphene's conductivity is isotropic and frequency-dependent, so we write $\sigma(\omega) \equiv \sigma_{xx} = \sigma_{yy}$. From (3.53) and (3.50), we get

$$B_{1,y} = -\frac{\kappa_2}{\kappa_1}\frac{\varepsilon_1^r}{\varepsilon_2^r}B_{2,y}, \tag{3.55}$$

which we insert in (3.54) to obtain

$$\frac{\varepsilon_1^r}{\kappa_1(q,\omega)} + \frac{\varepsilon_2^r}{\kappa_2(q,\omega)} + i\frac{\sigma(\omega)}{\omega\varepsilon_0} = 0. \tag{3.56}$$

This last equation describes the dispersion relation, $\omega(q)$, of graphene TM surface plasmon-polaritons. Notice that this is an implicit equation, so it needs to be solved numerically. Nonetheless, just by looking at it, we can see that it is only solvable when $\text{Im}\left\{\sigma(\omega)\right\} > 0$.

3.2.2 Results for single layer graphene

In fig. 3.9, we present our results for the total conductivity (Drude plus regular terms) in SLG, as a function of the frequency, $f = \omega/(2\pi)$, across the spectral region where we are interested to study the spectrum of GSPPs —from the THz up to the mid-infrared. We recall that we have set $\Gamma = 16$meV; moreover, in the following results, we will always be considering room temperature, $T = 300$K [3]. We also stress that we avoided exceeding frequencies of 30THz because of the surface polar phonons that arise from the SiO_2 —the typical substrate used as medium 2—, according to the work done by Eduardo Dias in his master's thesis (fig. 3.10).

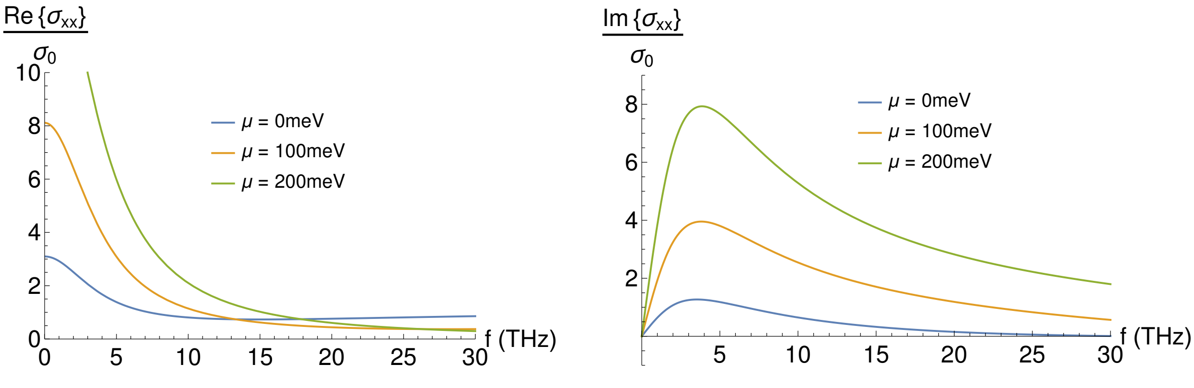

(a)

(b)

Figure 3.9: Total conductivity in SLG: (a) real part; (b) imaginary part.

---

[3] It should already be clear, from the results for $\mu = 0$meV, that we are not considering zero temperature.

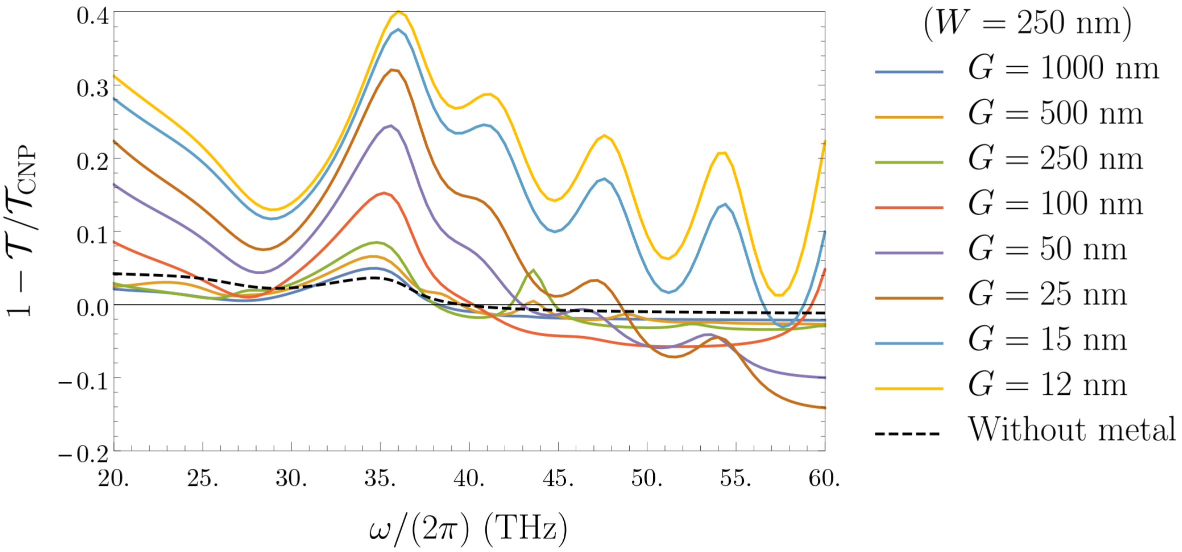

Figure 3.10: Evidence of surface optical phonons arising from the SiO_2 substrate. In this plot, the quantity in focus is the optical transmittance, $\mathcal{T}$, with $\mathcal{T}_{CNP}$ being the optical transmittance in the charge neutrality point. This quantity was obtained within a theoretical calculation, which takes into account the full dielectric function of the SiO_2. The parameters W and G correspond to a and $d - a$, repectively, in the scheme of fig. 1.6. The peak that starts at $f \sim 30$THz was interpreted as a contribution from the SiO_2 optical phonons. Image kindly provided by Eduardo Dias (private communication).

Given the total conductivity at a given Fermi level, we can obtain the dispersion curve by solving eq. (3.56) numerically. Notice that, if we consider only the Drude contribution with $\Gamma = 0$, we have a pure imaginary conductivity and we can solve this equation with real q. If not, we have to consider a complex-valued wave vector, whose imaginary part characterizes the attenuation of the SPPs [19, 62]. In fig. 3.11, we present the spectrum of the GSPPs for $\mu = 450$meV, which we obtained by taking into account the total conductiviy. This curve is in agreement with the results obtained in ref. [19], namely with fig. 4.2 (of this reference), where the authors considered only the Drude contribution (which is the dominant term in this case) with no absorption ($\Gamma = 0$), and fig. 4.3, where they verified that the consideration of absorption ($\Gamma \neq 0$) only affects the spectrum in the region of low wave vectors. Analyzing the spectrum, we see that the dispersion curve lies to the right of the light line, which indicates, as we have mentioned earlier, that we cannot excite GSPPs simply by directly shining electromagnetic radiation [4]. It is now clear why we need to use a setup with a periodic grid, like the one described in section 1.2.3 (see fig. 1.6).

---

[4] In fact, if we look closely, we see that the dispersion curve crosses the light line at some point (this happens only because we are considering a non-zero Γ, which is the more realistic situation). However, this point falls within the overdamped regime, $\omega_{SPP}/\gamma < 1$, in which SPPs cannot be sustained [19].

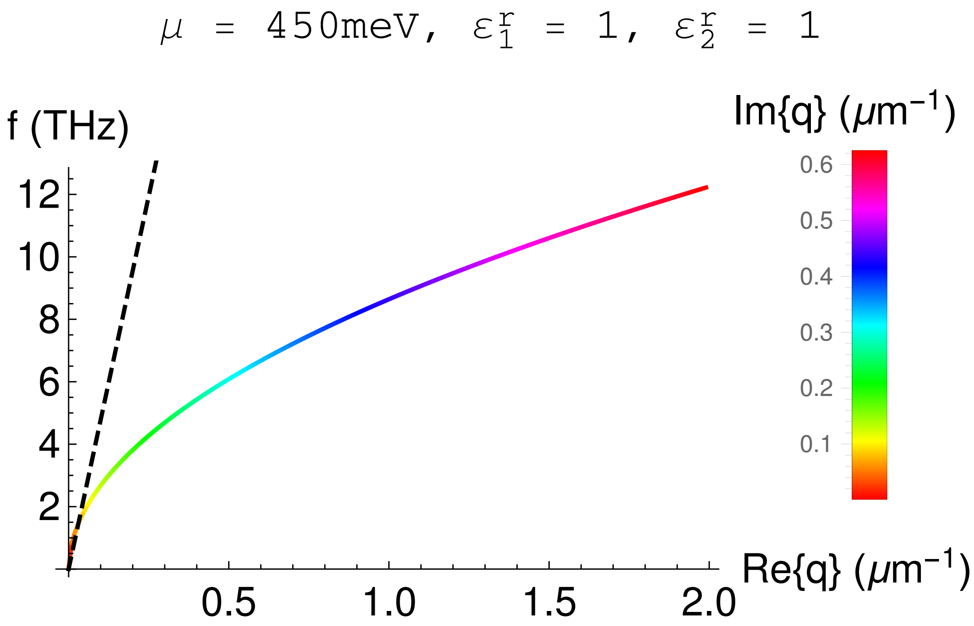

Figure 3.11: Dispersion relation of TM GSPPs in SLG. The dashed line corresponds to the light dispersion, $\omega = cq$, where c is the speed of the light in the medium (in this case we considered air).

At last, we can fix a wave vector —physically, if we take the light line as roughly vertical, this corresponds to fixing a gap in the periodic grid— and study the dependency of the dispersion curves on the Fermi level (or the carrier density). The results are shown in fig. 3.12. We stress that we do not obtain $f(n = 0) = 0$ in fig. 3.12(b) because of the finite temperature.

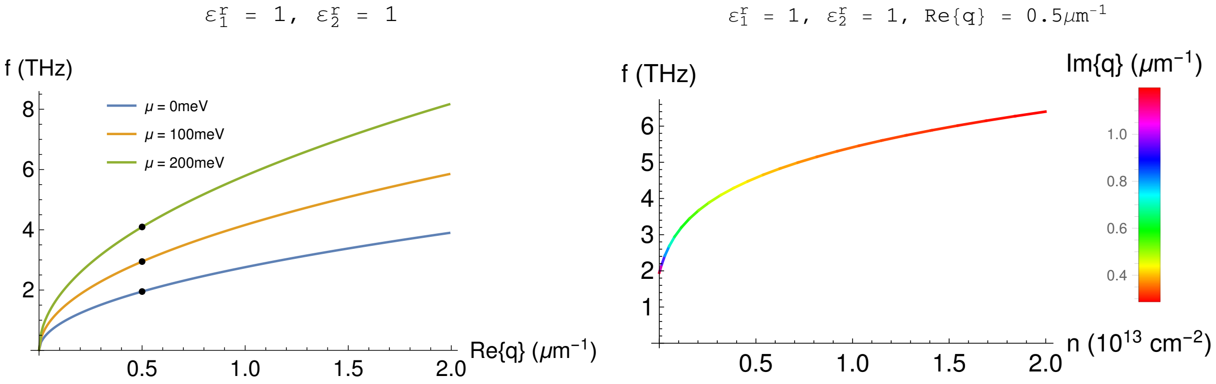

(a)

(b)

Figure 3.12: Spectrum of TM GSPPs in SLG: dependency on the Fermi level/carrier density. Figure (a) schematically shows the procedure used to obtain figure (b).

3.2.3 Results for twisted bilayer graphene

For the tBLG, we repeated the previous analysis —namely the last 2 plots from fig. 3.12, which we considered as sufficiently representative— for two different twist angles.

$\underline{\theta = 9^\circ}$

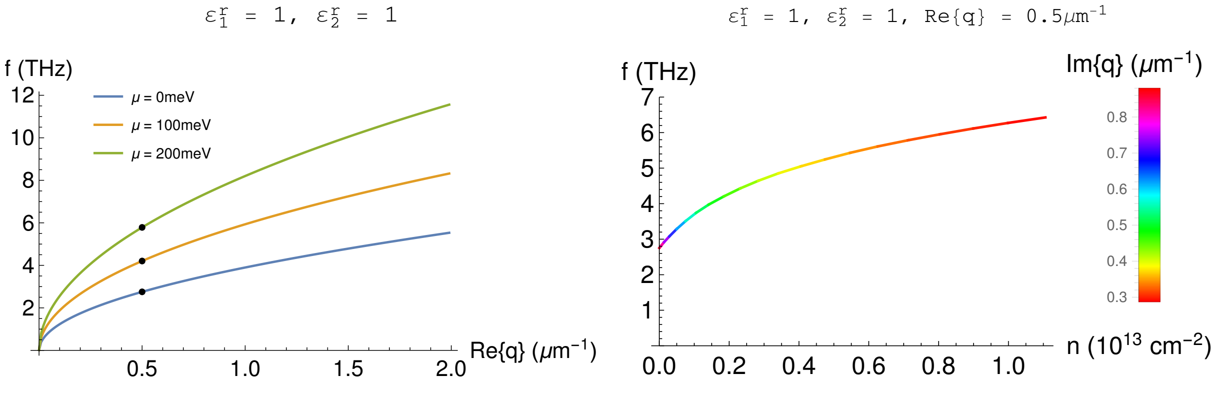

(a) (b)

Figure 3.13: Spectrum of TM GSPPs in tBLG with $\theta = 9^\circ$: dependency on the Fermi level/carrier density. The black dots in (a) mark the fixed parameter in (b).

For this angle, we see that the “signatures” of the curves do not differ a lot from those of the SLG. This happens due to two main reasons:

- Within this range of frequency, $f \lesssim 30\text{THz} \Leftrightarrow \hbar\omega \lesssim 124\text{meV}$, the regular conductivity is basically twice the value obtained for the SLG (fig. 3.6(a) indicates that). Moreover, for $\mu \lesssim 250\text{meV}$, the Drude weight is also twice the value obtained for the SLG (see fig. 3.4(a)). Therefore, we do not capture any hybridization effect and we just recover the total conductivity of a decoupled BLG.
- As we can see in fig. 2.13(b), the curves $n(\mu)$ for $\theta = 9^\circ$ and for decoupled BLG are also very close within the range in focus, $\mu \lesssim 250\text{meV} \Leftrightarrow n \lesssim 1 \times 10^{13}\text{cm}^{-2}$.

$\underline{\theta = 1.8^\circ}$

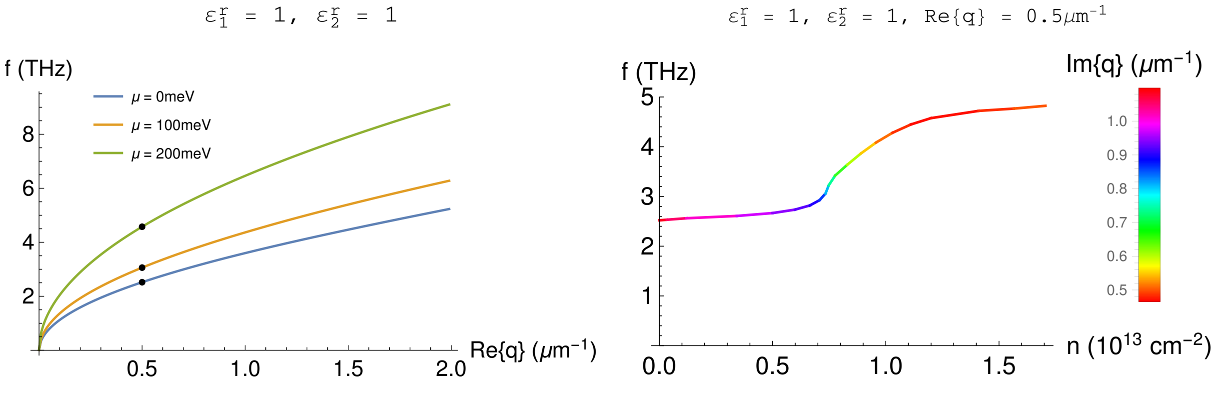

(a) (b)

Figure 3.14: Spectrum of TM GSPPs in tBLG with $\theta = 1.8^\circ$: dependency on the Fermi level/carrier density. The black dots in (a) mark the fixed parameter in (b).

In this case, not only the total conductivity is different but also the relation $n(\mu)$ changes drastically. This leads to the plot of fig. 3.14(b), which we highlight since it is totally different from all the results obtained before. As an immediate application, we can think of using these results as an alternative method for determining the twist angle. Nevertheless, a more extensive study on the behavior of these curves with the variation of θ remains to be done, in order to investigate more promising applications.

Chapter 4

Electron-electron interactions

The effects of electron-electron interactions are the subject matter of this chapter. We start by including an additional term in the Hamiltonian, which takes into account the long range Coulomb repulsion between electrons; Thomas-Fermi (TF) screening is considered later. Within a mean field (MF) analysis, we derive expressions for the Hartree-Fock (HF) corrections due to these interactions. Band renormalization is computed for the SLG and compared to the literature. Bearing in mind the explanation of the enhanced gaps discussed in section 3.1.3, we also calculate the bandgap renormalization for a system described by the SLG Hamiltonian with a gap. The analysis of the tBLG has been initiated but results were not yet obtained; here, we discuss the difficulties we have encountered and strategies to solve them in future works.

4.1 Long range Coulomb interaction

In the next sections, our goal is to derive the expressions for the band renormalization due to electron-electron Coulomb interactions. This deduction has in mind further implementations for both SLG and tBLG systems. Yet, it becomes hard to maintain a general notation and proceed with a derivation that can be applied to both systems. Therefore, we will stick to the SLG, for which the notation is lighter and the deduction simpler. In the end of each section, we will highlight the differences that appear in the tBLG treatment, and present just the final expressions, which can be obtained in the exact same manner.

We start by writing the electron-electron interaction in the usual form (2-particle operator),

$$V_{ee} = \frac{1}{2}\sum_{\sigma,\sigma'}\int d\boldsymbol{r}d\boldsymbol{r}'\ \hat{\Psi}^{\dagger}_{\sigma}(\boldsymbol{r})\hat{\Psi}^{\dagger}_{\sigma'}(\boldsymbol{r}')v(|\boldsymbol{r}-\boldsymbol{r}'|)\hat{\Psi}_{\sigma'}(\boldsymbol{r}')\hat{\Psi}_{\sigma}(\boldsymbol{r}), \tag{4.1}$$

where $\hat{\Psi}^{\dagger}_{\sigma}(\boldsymbol{r})/\hat{\Psi}_{\sigma}(\boldsymbol{r})$ are the creation/destruction fermionic field operators for spin σ and position $\boldsymbol{r}$ and $v(|\boldsymbol{r}-\boldsymbol{r}'|)$ is the Coulomb potential between 2 electrons,

$$v(|\boldsymbol{r}-\boldsymbol{r}'|) = \frac{e^2}{4\pi\varepsilon_r\varepsilon_0|\boldsymbol{r}-\boldsymbol{r}'|}. \tag{4.2}$$

We want to write eq. (4.1) in terms of band operators. In order to do so, we expand the field operators in a complete basis set, the Bloch basis $\{\psi_{\boldsymbol{k},\sigma,\lambda}(\boldsymbol{r})\}$ (which diagonalizes the Hamiltonian), such that

$$\hat{\Psi}_\sigma(\boldsymbol{r}) = \sum_{\boldsymbol{k},\lambda} \psi_{\boldsymbol{k},\sigma,\lambda}(\boldsymbol{r}) \hat{c}_{\boldsymbol{k},\sigma,\lambda}, \tag{4.3}$$

where we recall that $\hat{c}_{\boldsymbol{k},\sigma,\lambda}$ is the fermionic operator that annihilates an electron with crystal momentum $\boldsymbol{k} \in BZ$ and spin σ in band λ. The Bloch basis is spin independent and we can write

$$|\psi_{\boldsymbol{k},\sigma,\lambda}\rangle = |\psi_{\boldsymbol{k},\lambda}\rangle = \sum_\alpha c_{\alpha,\lambda}(\boldsymbol{k}) \, |\psi_{\boldsymbol{k},\alpha}\rangle \,, \tag{4.4}$$

where α is the label for the sublattice. We clarify that the $c_{\alpha,\lambda}(\boldsymbol{k})$ are the same that appear in the column vectors, (2.16), after diagonalizing the Hamiltonian (notice that there is a set of column vectors for each λ). Within the tight-binding approximation (recall (2.8)), we have

$$\begin{aligned}
\psi_{\boldsymbol{k},\lambda}(\boldsymbol{r}) \equiv \langle \boldsymbol{r} | \psi_{\boldsymbol{k},\lambda}\rangle &= \sum_\alpha c_{\alpha,\lambda}(\boldsymbol{k}) \, \langle \boldsymbol{r}|\psi_{\boldsymbol{k},\alpha}\rangle \\
&= \frac{1}{\sqrt{N}} \sum_\alpha \sum_{n_1,n_2} c_{\alpha,\lambda}(\boldsymbol{k}) e^{i\boldsymbol{k}\cdot(\boldsymbol{R}_{n_1,n_2}+\boldsymbol{\delta}_\alpha)} \, \langle \boldsymbol{r}|\boldsymbol{R}_{n_1,n_2}+\boldsymbol{\delta}_\alpha, \alpha\rangle \\
&= \frac{1}{\sqrt{N}} \sum_\alpha \sum_{\boldsymbol{R}} c_{\alpha,\lambda}(\boldsymbol{k}) e^{i\boldsymbol{k}\cdot\boldsymbol{R}^\alpha} \, \phi_\alpha(\boldsymbol{r}-\boldsymbol{R}^\alpha),
\end{aligned} \tag{4.5}$$

where $\boldsymbol{R}^\alpha \equiv \boldsymbol{R}_{n_1,n_2} + \boldsymbol{\delta}_\alpha$. In the new basis, the interaction term reads

$$V_{ee} = \frac{1}{2} \sum_{\sigma,\sigma'} \sum_{1,2,3,4} V_{1,2,3,4} \; \hat{c}^\dagger_{1,\sigma} \hat{c}^\dagger_{2,\sigma'} \hat{c}_{3,\sigma'} \hat{c}_{4,\sigma}, \tag{4.6}$$

where the numbers $1-4$ are used for a composed index, $1 \equiv \{\boldsymbol{k}_1, \lambda_1\}$ for example, and $V_{1,2,3,4}$ is given by

$$\begin{aligned}
V_{1,2,3,4} =& \frac{1}{N^2} \sum_{\substack{\alpha_1,\alpha_2,\\ \alpha_3,\alpha_4}} \sum_{\substack{\boldsymbol{R}_1,\boldsymbol{R}_2,\\ \boldsymbol{R}_3,\boldsymbol{R}_4}} [c_{\alpha_1,\lambda_1}(\boldsymbol{k}_1)]^* \, [c_{\alpha_2,\lambda_2}(\boldsymbol{k}_2)]^* \, c_{\alpha_3,\lambda_3}(\boldsymbol{k}_3) c_{\alpha_4,\lambda_4}(\boldsymbol{k}_4) \times \\
& \times e^{-i\boldsymbol{k}_1\cdot\boldsymbol{R}_1^{\alpha_1}} e^{-i\boldsymbol{k}_2\cdot\boldsymbol{R}_2^{\alpha_2}} e^{i\boldsymbol{k}_3\cdot\boldsymbol{R}_3^{\alpha_3}} e^{i\boldsymbol{k}_4\cdot\boldsymbol{R}_4^{\alpha_4}} \times \\
& \times \int d\boldsymbol{r} d\boldsymbol{r}' \;\; [\phi_{\alpha_1}(\boldsymbol{r}-\boldsymbol{R}_1^{\alpha_1})]^* \, [\phi_{\alpha_2}(\boldsymbol{r}'-\boldsymbol{R}_2^{\alpha_2})]^* \, v(|\boldsymbol{r}-\boldsymbol{r}'|) \phi_{\alpha_3}(\boldsymbol{r}'-\boldsymbol{R}_3^{\alpha_3}) \phi_{\alpha_4}(\boldsymbol{r}-\boldsymbol{R}_4^{\alpha_4}).
\end{aligned} \tag{4.7}$$

In the spirit of the tight-binding approximation (localized atomic orbitals), it is reasonable to assume that the most important terms in the integral occur when $\{\boldsymbol{R}_1, \alpha_1\} = \{\boldsymbol{R}_4, \alpha_4\}$ and $\{\boldsymbol{R}_2, \alpha_2\} = \{\boldsymbol{R}_3, \alpha_3\}$. This yields

$$\begin{aligned}
V_{1,2,3,4} = & \frac{1}{N^2} \sum_{\alpha_1,\alpha_2} \sum_{\boldsymbol{R}_1,\boldsymbol{R}_2} [c_{\alpha_1,\lambda_1}(\boldsymbol{k}_1)]^* \, [c_{\alpha_2,\lambda_2}(\boldsymbol{k}_2)]^* \, c_{\alpha_2,\lambda_3}(\boldsymbol{k}_3) c_{\alpha_1,\lambda_4}(\boldsymbol{k}_4) \times \\
& \times e^{-i(\boldsymbol{k}_1-\boldsymbol{k}_4)\cdot\boldsymbol{R}_1^{\alpha_1}} e^{-i(\boldsymbol{k}_2-\boldsymbol{k}_3)\cdot\boldsymbol{R}_2^{\alpha_2}} \int d\boldsymbol{r} d\boldsymbol{r}' \; |\phi_{\alpha_1}(\boldsymbol{r}-\boldsymbol{R}_1^{\alpha_1})|^2 \frac{e^2}{4\pi\varepsilon_r\varepsilon_0|\boldsymbol{r}-\boldsymbol{r}'|} |\phi_{\alpha_2}(\boldsymbol{r}'-\boldsymbol{R}_2^{\alpha_2})|^2.
\end{aligned} \tag{4.8}$$

We now work the following term:

$$\begin{aligned}
&\sum_{\boldsymbol{R}_1,\boldsymbol{R}_2} e^{-i(\boldsymbol{k}_1-\boldsymbol{k}_4).\boldsymbol{R}_1^{\alpha_1}} e^{-i(\boldsymbol{k}_2-\boldsymbol{k}_3).\boldsymbol{R}_2^{\alpha_2}} \int d\boldsymbol{r}d\boldsymbol{r'}\ |\phi_{\alpha_1}(\boldsymbol{r}-\boldsymbol{R}_1^{\alpha_1})|^2 \frac{e^2}{4\pi\varepsilon_r\varepsilon_0|\boldsymbol{r}-\boldsymbol{r'}|}|\phi_{\alpha_2}(\boldsymbol{r'}-\boldsymbol{R}_2^{\alpha_2})|^2 \\
&=\sum_{\boldsymbol{R}_1,\boldsymbol{R}_2} e^{-i(\boldsymbol{k}_1-\boldsymbol{k}_4).\boldsymbol{R}_1^{\alpha_1}} e^{-i(\boldsymbol{k}_2-\boldsymbol{k}_3).\boldsymbol{R}_2^{\alpha_2}} \int d\boldsymbol{r}d\boldsymbol{r'}\ |\phi_{\alpha_1}(\boldsymbol{r})|^2 \frac{e^2}{4\pi\varepsilon_r\varepsilon_0|\boldsymbol{r}-\boldsymbol{r'}-(\boldsymbol{R}_2^{\alpha_2}-\boldsymbol{R}_1^{\alpha_1})\,|}|\phi_{\alpha_2}(\boldsymbol{r'})|^2 \\
&=\sum_{\boldsymbol{R}_1,\boldsymbol{R}_2} e^{-i(\boldsymbol{k}_1-\boldsymbol{k}_4).\boldsymbol{R}_1^{\alpha_1}} e^{-i(\boldsymbol{k}_2-\boldsymbol{k}_3).\boldsymbol{R}_2^{\alpha_2}} \int d\boldsymbol{r}d\boldsymbol{r'}\ |\phi_{\alpha_1}(\boldsymbol{r'})|^2 \frac{e^2}{4\pi\varepsilon_r\varepsilon_0|\boldsymbol{r}-\boldsymbol{r'}-(\boldsymbol{R}_1^{\alpha_1}-\boldsymbol{R}_2^{\alpha_2})\,|}|\phi_{\alpha_2}(\boldsymbol{r})|^2 \\
&=\sum_{\boldsymbol{R}_1,\boldsymbol{R'}} e^{-i(\boldsymbol{k}_1-\boldsymbol{k}_4+\boldsymbol{k}_2-\boldsymbol{k}_3).\boldsymbol{R}_1^{\alpha_1}} e^{i(\boldsymbol{k}_2-\boldsymbol{k}_3).\boldsymbol{R'}_{\alpha_1,\alpha_2}} \int d\boldsymbol{r}d\boldsymbol{r'}\ |\phi_{\alpha_1}(\boldsymbol{r'})|^2 \frac{e^2}{4\pi\varepsilon_r\varepsilon_0|\boldsymbol{r}-\boldsymbol{r'}-\boldsymbol{R'}_{\alpha_1,\alpha_2}|}|\phi_{\alpha_2}(\boldsymbol{r})|^2,
\end{aligned} \tag{4.9}$$

where $\boldsymbol{R'}_{\alpha_1,\alpha_2} = \boldsymbol{R}_1 - \boldsymbol{R}_2 + \boldsymbol{\delta}_{\alpha_1} - \boldsymbol{\delta}_{\alpha_2} = \boldsymbol{R'} + \boldsymbol{\delta}_{\alpha_1,\alpha_2}$, with $\boldsymbol{R'} = \boldsymbol{R}_1 - \boldsymbol{R}_2$ defining a lattice centered in a different point for each $\boldsymbol{R}_1$. In the limit of an infinite system, the origin does not matter and we can treat $\boldsymbol{R'}$ as an independent lattice. Using the orthogonality relation,

$$\sum_{\boldsymbol{R}_1} e^{-i(\boldsymbol{k}_1-\boldsymbol{k}_4+\boldsymbol{k}_2-\boldsymbol{k}_3).\boldsymbol{R}_1^{\alpha_1}} = N\ \delta_{\boldsymbol{k}_1-\boldsymbol{k}_4,-\boldsymbol{k}_2+\boldsymbol{k}_3}, \quad \boldsymbol{k}_i \in BZ, \tag{4.10}$$

and the identity, $\delta_{\boldsymbol{k}_1-\boldsymbol{k}_4,-\boldsymbol{k}_2+\boldsymbol{k}_3} = \sum_{\boldsymbol{q}} \delta_{\boldsymbol{k}_2-\boldsymbol{k}_3,\boldsymbol{q}}\ \delta_{\boldsymbol{k}_1-\boldsymbol{k}_4,-\boldsymbol{q}}$, we obtain

$$\begin{aligned}
V_{1,2,3,4} = \frac{1}{N}\sum_{\alpha_1,\alpha_2}\sum_{\boldsymbol{R'}}\sum_{\boldsymbol{q}} &[c_{\alpha_1,\lambda_1}(\boldsymbol{k}_4-\boldsymbol{q})]^*\ [c_{\alpha_2,\lambda_2}(\boldsymbol{k}_3+\boldsymbol{q})]^*\ c_{\alpha_2,\lambda_3}(\boldsymbol{k}_3)c_{\alpha_1,\lambda_4}(\boldsymbol{k}_4)\times \\
&\times e^{i\boldsymbol{q}.\boldsymbol{R'}_{\alpha_1,\alpha_2}}\ \delta_{\boldsymbol{k}_2-\boldsymbol{k}_3,\boldsymbol{q}}\ \delta_{\boldsymbol{k}_1-\boldsymbol{k}_4,-\boldsymbol{q}} \int d\boldsymbol{r}d\boldsymbol{r'}\ |\phi_{\alpha_1}(\boldsymbol{r'})|^2 \frac{e^2}{4\pi\varepsilon_r\varepsilon_0|\boldsymbol{r}-\boldsymbol{r'}-\boldsymbol{R'}_{\alpha_1,\alpha_2}|}|\phi_{\alpha_2}(\boldsymbol{r})|^2.
\end{aligned} \tag{4.11}$$

Let us isolate and manipulate the following term:

$$\begin{aligned}
&\sum_{\boldsymbol{R'}} e^{i\boldsymbol{q}.\boldsymbol{R'}_{\alpha_1,\alpha_2}} \int d\boldsymbol{r}d\boldsymbol{r'}\ |\phi_{\alpha_1}(\boldsymbol{r'})|^2 \frac{e^2}{4\pi\varepsilon_r\varepsilon_0|\boldsymbol{r}-\boldsymbol{r'}-\boldsymbol{R'}_{\alpha_1,\alpha_2}|}|\phi_{\alpha_2}(\boldsymbol{r})|^2 \\
&=\int d\boldsymbol{r}d\boldsymbol{r'}\ |\phi_{\alpha_1}(\boldsymbol{r'})|^2 e^{i\boldsymbol{q}\cdot(\boldsymbol{r}-\boldsymbol{r'})} \sum_{\boldsymbol{R'}} e^{-i\boldsymbol{q}\cdot\left(\boldsymbol{r}-\boldsymbol{r'}-\boldsymbol{R'}_{\alpha_1,\alpha_2}\right)} \frac{e^2}{4\pi\varepsilon_r\varepsilon_0|\boldsymbol{r}-\boldsymbol{r'}-\boldsymbol{R'}_{\alpha_1,\alpha_2}|}|\phi_{\alpha_2}(\boldsymbol{r})|^2 \\
&=\int d\boldsymbol{r}d\boldsymbol{r'}\ |\phi_{\alpha_1}(\boldsymbol{r'})|^2 e^{i\boldsymbol{q}\cdot(\boldsymbol{r}-\boldsymbol{r'})} \frac{1}{A_{u.c.}} \int d\boldsymbol{R'}\ e^{-i\boldsymbol{q}\cdot\left(\boldsymbol{r}-\boldsymbol{r'}-\boldsymbol{R'}_{\alpha_1,\alpha_2}\right)} \frac{e^2}{4\pi\varepsilon_r\varepsilon_0|\boldsymbol{r}-\boldsymbol{r'}-\boldsymbol{R'}_{\alpha_1,\alpha_2}|}|\phi_{\alpha_2}(\boldsymbol{r})|^2,
\end{aligned} \tag{4.12}$$

where we converted the sum into an integral in the limit of an infinite system, $\sum_{\boldsymbol{R'}} \to \frac{1}{A_{u.c.}}\int d\boldsymbol{R'}$. At this moment, we recognize the FT of the Coulomb potential,

$$\int d\boldsymbol{R'}\ e^{-i\boldsymbol{q}\cdot\left(\boldsymbol{r}-\boldsymbol{r'}-\boldsymbol{R'}_{\alpha_1,\alpha_2}\right)} \frac{e^2}{4\pi\varepsilon_r\varepsilon_0|\boldsymbol{r}-\boldsymbol{r'}-\boldsymbol{R'}_{\alpha_1,\alpha_2}|} = \int d\boldsymbol{R'}\ e^{-i\boldsymbol{q}.\boldsymbol{R'}} \frac{e^2}{4\pi\varepsilon_r\varepsilon_0|\boldsymbol{R'}|} = v(\boldsymbol{q}), \tag{4.13}$$

which is computed in appendix D and yields

$$v(\boldsymbol{q}) = \frac{e^2}{2\varepsilon_r\varepsilon_0 q}. \tag{4.14}$$

Collecting all terms, we rewrite $V_{1,2,3,4}$,

$$V_{1,2,3,4} = \frac{1}{NA_{u.c.}} \sum_{\alpha_1,\alpha_2} \sum_{\boldsymbol{R}'} \sum_{\boldsymbol{q}} \left[c_{\alpha_1,\lambda_1}(\boldsymbol{k}_4 - \boldsymbol{q})\right]^* \left[c_{\alpha_2,\lambda_2}(\boldsymbol{k}_3 + \boldsymbol{q})\right]^* c_{\alpha_2,\lambda_3}(\boldsymbol{k}_3) c_{\alpha_1,\lambda_4}(\boldsymbol{k}_4) \times$$
$$\times\, \delta_{\boldsymbol{k}_2-\boldsymbol{k}_3,\boldsymbol{q}}\, \delta_{\boldsymbol{k}_1-\boldsymbol{k}_4,-\boldsymbol{q}}\, I_{\alpha_1}(\boldsymbol{q}) I_{\alpha_2}(-\boldsymbol{q}) \frac{e^2}{2\varepsilon_r\varepsilon_0 q}, \tag{4.15}$$

where

$$I_{\alpha_i}(\boldsymbol{q}) = \int d\boldsymbol{r}\; e^{-\boldsymbol{q}.\boldsymbol{r}} |\phi_{\alpha_i}(\boldsymbol{r})|^2. \tag{4.16}$$

The integrals in the last equation can be approximated to the unity, as done in ref. [63]. Qualitatively, we may argue that the atomic orbitals are only significant (deep) inside the unit cell, $\boldsymbol{r} \in u.c.$. Since $\boldsymbol{q} \in BZ$ (due to the Dirac deltas), we have $\boldsymbol{q}.\boldsymbol{r} \ll 1$ for most $\boldsymbol{q}$ and, therefore, $I_{\alpha_i}(\boldsymbol{q}) \simeq 1$.

At last, we retain all these results to write the interaction term as

$$V_{ee} = \frac{1}{2NA_{u.c.}} \sum_{\sigma,\sigma'} \sum_{\substack{\lambda_1,\lambda_2,\\ \lambda_3,\lambda_4}} \sum_{\boldsymbol{k}_3,\boldsymbol{k}_4} \sum_{\alpha_1,\alpha_2} \sum_{\boldsymbol{q}} \left[c_{\alpha_1,\lambda_1}(\boldsymbol{k}_4 - \boldsymbol{q})\right]^* \left[c_{\alpha_2,\lambda_2}(\boldsymbol{k}_3 + \boldsymbol{q})\right]^* c_{\alpha_2,\lambda_3}(\boldsymbol{k}_3) c_{\alpha_1,\lambda_4}(\boldsymbol{k}_4) \times$$
$$\times \frac{e^2}{2\varepsilon_r\varepsilon_0 q}\, \hat{c}^\dagger_{\boldsymbol{k}_4-\boldsymbol{q},\lambda_1,\sigma} \hat{c}^\dagger_{\boldsymbol{k}_3+\boldsymbol{q},\lambda_2,\sigma'} \hat{c}_{\boldsymbol{k}_3,\lambda_3,\sigma'} \hat{c}_{\boldsymbol{k}_4,\lambda_4,\sigma}. \tag{4.17}$$

The tBLG treatment

For this system, the Coulomb potential is given by (4.2) when the electrons are in the same layer, and by

$$v(|\boldsymbol{r} - \boldsymbol{r}'|) = \frac{e^2}{4\pi\varepsilon_r\varepsilon_0\sqrt{r^2 - (r')^2 + d_\perp^2}}, \tag{4.18}$$

when they are not. The FT of this potential is also done in appendix D and yields

$$v(\boldsymbol{q}) = v(q) = \frac{e^2}{2\varepsilon_r\varepsilon_0 q} e^{-qd_\perp}, \tag{4.19}$$

which we may approximate to the same result as before since $e^{-qd_\perp} \sim 1$ for $\boldsymbol{q} \in mBZ$.

The expansion of the field operators in the Bloch basis is done in the following manner:

$$\hat{\Psi}_\sigma(\boldsymbol{r}) = \sum_{\boldsymbol{q},\lambda} \psi_{\boldsymbol{q},\lambda}(\boldsymbol{r}) \hat{c}_{\boldsymbol{q},\sigma,\lambda}, \tag{4.20}$$

with

$$\psi_{\boldsymbol{q},\lambda}(\boldsymbol{r}) = \frac{1}{\sqrt{N}} \sum_{\gamma(\nu)} \sum_{\boldsymbol{R}} c_{\gamma(\nu),\lambda}(\boldsymbol{q}) e^{i\tilde{\boldsymbol{q}}.\boldsymbol{R}^\nu} \phi_\nu(\boldsymbol{r} - \boldsymbol{R}^\nu), \tag{4.21}$$

where $\boldsymbol{q} \in mBZ$, $\tilde{\boldsymbol{q}} = K + \boldsymbol{q}$ (recalling that the momentum $\boldsymbol{q}$ which diagonalizes the Hamiltonian is being measured from the Dirac point K), ν labels both sublattice and layer, $\nu = \{\alpha, i\}$, and γ is the index associated with all the components of the column vectors, like the one shown in (2.119); the notation $\gamma(\nu)$ is used to express that γ also encodes information about the sublattice and the layer. Notice that we are not taking into consideration the valley degeneracy. However, we do not expect the Coulomb interactions between electrons in the opposite valeys to be significant due to the difference in momentum.

We are therefore separating the treatment of K and K' bands.

The final expression for the interaction term is

$$V_{ee} = \frac{1}{2NA_{g.u.c.}} \sum_{\sigma,\sigma'} \sum_{\substack{\lambda_1,\lambda_2,\\ \lambda_3,\lambda_4}} \sum_{\boldsymbol{q}_3,\boldsymbol{q}_4} \sum_{\substack{\gamma_1(\nu_1),\gamma_2(\nu_2),\\ \gamma_3(\nu_2),\gamma_4(\nu_1)}} \sum_{\boldsymbol{q}} \left[c_{\gamma_1(\nu_1),\lambda_1}(\boldsymbol{q}_4 - \boldsymbol{q})\right]^* \left[c_{\gamma_2(\nu_2),\lambda_2}(\boldsymbol{q}_3 + \boldsymbol{q})\right]^* \times$$
$$\times\, c_{\gamma_3(\nu_2),\lambda_3}(\boldsymbol{q}_3) c_{\gamma_4(\nu_1),\lambda_4}(\boldsymbol{q}_4) \frac{e^2}{2\varepsilon_r\varepsilon_0 q}\, \hat{c}^\dagger_{\boldsymbol{q}_4-\boldsymbol{q},\lambda_1,\sigma} \hat{c}^\dagger_{\boldsymbol{q}_3+\boldsymbol{q},\lambda_2,\sigma'} \hat{c}_{\boldsymbol{q}_3,\lambda_3,\sigma'} \hat{c}_{\boldsymbol{q}_4,\lambda_4,\sigma}, \tag{4.22}$$

where we stress that $A_{g.u.c.}$ is the area of a graphene unit cell (and not the area of a moiré unit cell). We also point out that, for the tBLG, the approximation $I_{\nu_i}(\boldsymbol{q}) \simeq 1$ is comparatively better to the one done in the SLG case, because $\boldsymbol{q} \in mBZ$.

4.2 Thomas-Fermi screening

Within a TF approximation, the screened Coulomb interaction reads

$$v_s(q) = \frac{e^2}{2\varepsilon_r\varepsilon_0(q + q_{TF})}, \tag{4.23}$$

where q_{TF} stands for the TF wave vector. This result can be obtained as a static low-energy limit of random phase approximation (RPA) [64], which is equivalent to writing the Coulomb potential screened by the static dielectric function $\varepsilon(q)$,

$$v(q) \to v_s(q) = \frac{v(q)}{\varepsilon(q)}, \tag{4.24}$$

where

$$\varepsilon(q) = 1 + \mathcal{U}(q)N(\mu), \tag{4.25}$$

with $\mathcal{U}(q) = \frac{e^2}{2\varepsilon_r\varepsilon_0 q}$ standing for the FT of the 2D Coulomb potential and $N(\mu)$ for the DOS (per total area) at Fermi level μ. This implies

$$q_{TF} = \frac{e^2}{2\varepsilon_r\varepsilon_0} N(\mu). \tag{4.26}$$

We notice that, for systems like graphene, we have poor screening for $\mu \sim \mu_0$ since the DOS vanishes at this point. Nonetheless, we may still include some residual phenomenological screening due to disorder effects or to the fact that the sp_2 orbitals are not taken into account in the models.

4.3 Mean field treatment

We introduce the HF approximation to treat the interaction term in eq. (4.17). This MF approach can be done by using the Gibbs-Bogoliubov inequality as a variational principle (see deduction in appendix E),

$$F \leq F_{MF} + \langle H - H_{MF} \rangle_{MF} \equiv \tilde{F}. \tag{4.27}$$

Given the Hamiltonian $H = H_0 + V$, what we do is to replace the interaction $V = V_{ee} + V_{ei} + V_{ii}$ by a one-body potential, V_{MF}, which is chosen in order to minimize the right hand side of (4.27). The ion-ion term, V_{ii}, can be discarded since it does not depend on fermionic field operators and therefore drops out when doing the functional derivative (it just redefines the zero energy). Regarding the remaining terms, we will only keep V_{ee} for now. As we shall see, we will get $V_{MF} = V_H + V_{exc}$, where V_H and V_{exc} are the Hartree and Fock/exchange terms, respectively. Later, we will show that the consideration of the electron-ion term, V_{ei}, cancels out the Hartree term.

We perform this MF treatment in real space. Recalling that our system's Hamiltonian is written as $H = H_0 + V_{ee}$, where H_0 is the non-interacting Hamiltonian and V_{ee} is given by (4.1), we introduce a MF Hamiltonian, $H_{MF} = H_0 + V_{MF}$, with

$$V_{MF} = \sum_{\sigma,\sigma'} \int d\boldsymbol{r} d\boldsymbol{r}' \ f(\boldsymbol{r},\boldsymbol{r}') \hat{\Psi}^{\dagger}_{\sigma}(\boldsymbol{r}) \hat{\Psi}_{\sigma'}(\boldsymbol{r}') \tag{4.28}$$

being the most general one-body interaction. Imposing an hermitian Hamiltonian, we obtain the relation $f(\boldsymbol{r},\boldsymbol{r}') = f^*(\boldsymbol{r}',\boldsymbol{r})$. Now, we introduce a variation in H_{MF}, $H_{MF} \to H_{MF} + \delta H_{MF}$, which corresponds to a variation $f \to f + \delta f$, and impose the extremum condition which minimizes $\tilde{F}$,

$$\begin{aligned} \delta \tilde{F} = 0 &\Leftrightarrow \delta \left(F_{MF} + \langle H - H_{MF} \rangle_{MF} \right) = 0 \\ &\Leftrightarrow \delta F_{MF} + \delta \langle V_{ee} \rangle_{MF} - \delta \langle V_{MF} \rangle_{MF} = 0. \end{aligned} \tag{4.29}$$

The computation of each term yields:

- $\delta \langle V_{ee} \rangle_{MF}$

$$\begin{aligned} \delta \langle V_{ee} \rangle &= \frac{1}{2} \sum_{\sigma,\sigma'} \int d\boldsymbol{r} d\boldsymbol{r}' \ v(|\mathbf{r} - \boldsymbol{r}'|) \delta \left(\langle \hat{\Psi}^{\dagger}_{\sigma}(\boldsymbol{r}) \hat{\Psi}^{\dagger}_{\sigma'}(\boldsymbol{r}') \hat{\Psi}_{\sigma'}(\boldsymbol{r}') \hat{\Psi}_{\sigma}(\boldsymbol{r}) \rangle \right) \\ &= \sum_{\sigma,\sigma'} \int d\boldsymbol{r} d\boldsymbol{r}' \ v(|\mathbf{r} - \boldsymbol{r}'|) \left[\left(\delta \langle \hat{n}_{\sigma}(\boldsymbol{r}) \rangle \right) \langle \hat{n}_{\sigma'}(\boldsymbol{r}') \rangle - \left(\delta \langle \hat{\Psi}^{\dagger}_{\sigma}(\boldsymbol{r}) \hat{\Psi}_{\sigma'}(\boldsymbol{r}') \rangle \right) \langle \hat{\Psi}^{\dagger}_{\sigma'}(\boldsymbol{r}') \hat{\Psi}_{\sigma}(\boldsymbol{r}) \rangle \right], \end{aligned} \tag{4.30}$$

  where we have dropped the label of MF and introduced the number operator, $\hat{n}_{\sigma}(\boldsymbol{r}) \equiv \hat{\Psi}^{\dagger}_{\sigma}(\boldsymbol{r}) \hat{\Psi}_{\sigma}(\boldsymbol{r})$. We also used Wick's Theorem, in the form

$$\langle \hat{\Psi}^{\dagger}_1 \hat{\Psi}^{\dagger}_2 \hat{\Psi}_3 \hat{\Psi}_4 \rangle = \langle \hat{\Psi}^{\dagger}_1 \hat{\Psi}_4 \rangle \langle \hat{\Psi}^{\dagger}_2 \hat{\Psi}_3 \rangle - \langle \hat{\Psi}^{\dagger}_1 \hat{\Psi}_3 \rangle \langle \hat{\Psi}^{\dagger}_2 \hat{\Psi}_4 \rangle + \cancelto{0}{\ldots} \tag{4.31}$$

  where the last terms are 0 because the averages do not conserve the number of particles (superconducting phases are not expected, therefore we do not allow them as a possible MF solution).

- $\delta \langle V_{MF} \rangle_{MF}$

$$\begin{aligned} \delta \langle V_{MF} \rangle &= \sum_{\sigma,\sigma'} \int d\boldsymbol{r} d\boldsymbol{r}' \ \delta \left(f(\boldsymbol{r},\boldsymbol{r}') \langle \hat{\Psi}^{\dagger}_{\sigma}(\boldsymbol{r}) \hat{\Psi}_{\sigma'}(\boldsymbol{r}') \rangle \right) \\ &= \sum_{\sigma,\sigma'} \int d\boldsymbol{r} d\boldsymbol{r}' \ \left[\left(\delta f(\boldsymbol{r},\boldsymbol{r}') \right) \langle \hat{\Psi}^{\dagger}_{\sigma}(\boldsymbol{r}) \hat{\Psi}_{\sigma'}(\boldsymbol{r}') \rangle + f(\boldsymbol{r},\boldsymbol{r}') \left(\delta \langle \hat{\Psi}^{\dagger}_{\sigma}(\boldsymbol{r}) \hat{\Psi}_{\sigma'}(\boldsymbol{r}') \rangle \right) \right]. \end{aligned} \tag{4.32}$$

- δF_{MF}

$$\begin{aligned}\delta F_{MF} &= \delta\left(-k_BT\,\mathrm{Tr}\left\{e^{-\beta(\hat H_{MF}-\cancel{\mu\hat N})}\right\}\right)\\ &= -k_BT\frac{\delta\left(\mathrm{Tr}\left\{e^{-\beta\hat H_{MF}}\right\}\right)}{\mathrm{Tr}\left\{e^{-\beta\hat H_{MF}}\right\}} = -k_BT\frac{\mathrm{Tr}\left\{e^{-\beta\left(\hat H_{MF}+\delta\hat H_{MF}\right)}\right\}-\mathrm{Tr}\left\{e^{-\beta\hat H_{MF}}\right\}}{\mathrm{Tr}\left\{e^{-\beta\hat H_{MF}}\right\}},\end{aligned} \tag{4.33}$$

where we absorbed the term $\mu\hat N$ (which arises from the free energy in the grand canonical ensemble) in $\hat H_{MF}$ to lighten the notation. We now work the term $\mathrm{Tr}\left\{e^{-\beta\left(\hat H+\delta\hat H\right)}\right\}$ to the first order in $\delta\hat H$:

$$\begin{aligned}\mathrm{Tr}\left\{e^{-\beta\left(\hat H+\delta\hat H\right)}\right\} &= \mathrm{Tr}\left\{\sum_{n=0}^{+\infty}\frac{(-\beta)^n}{n!}\left(\hat H+\delta\hat H\right)^n\right\} = 1+\mathrm{Tr}\left\{\sum_{n=1}^{+\infty}\frac{(-\beta)^n}{n!}\hat H^n\right\}+\\ &\quad+\mathrm{Tr}\left\{\sum_{n=1}^{+\infty}\frac{(-\beta)^n}{n!}\left(\delta\hat H\hat H^{n-1}+\hat H\delta\hat H\hat H^{n-2}+...+\hat H^{n-1}\delta\hat H\right)\right\}+\cancel{\mathcal{O}(\delta\hat H^2)}\\ &= \mathrm{Tr}\left\{e^{-\beta\hat H}\right\}+\mathrm{Tr}\left\{n\delta\hat H\sum_{n=1}^{+\infty}\frac{(-\beta)^n}{n(n-1)!}\hat H^{n-1}\right\}\\ &= \mathrm{Tr}\left\{e^{-\beta\hat H}\right\}-\beta\,\mathrm{Tr}\left\{\delta\hat H e^{-\beta\hat H}\right\},\end{aligned} \tag{4.34}$$

where we made use of the cyclic propertie of the trace. Using this result, (4.33) becomes

$$\begin{aligned}\delta F_{MF} &= \frac{\mathrm{Tr}\left\{\delta\hat H_{MF}\ e^{-\beta\hat H_{MF}}\right\}}{\mathrm{Tr}\left\{e^{-\beta\hat H_{MF}}\right\}} = \langle\delta\hat H_{MF}\rangle_{MF}\\ &= \sum_{\sigma,\sigma'}\int d\boldsymbol{r}d\boldsymbol{r}'\ \left(\delta f(\boldsymbol{r},\boldsymbol{r}')\right)\langle\hat\Psi^\dagger_\sigma(\boldsymbol{r})\hat\Psi_{\sigma'}(\boldsymbol{r}')\rangle_{MF}\,.\end{aligned} \tag{4.35}$$

Collecting these 3 terms and inserting them in eq. (4.29), we obtain

$$\begin{aligned}\delta\tilde F = \sum_{\sigma,\sigma'}\int d\boldsymbol{r}d\boldsymbol{r}'\ \Big\{&v(|\boldsymbol{r}-\boldsymbol{r}'|)\Big[\langle\hat n_{\sigma'}(\boldsymbol{r}')\rangle\ \delta\langle\hat n_\sigma(\boldsymbol{r})\rangle-\langle\hat\Psi^\dagger_{\sigma'}(\boldsymbol{r}')\hat\Psi_\sigma(\boldsymbol{r})\rangle\ \delta\langle\hat\Psi^\dagger_\sigma(\boldsymbol{r})\hat\Psi_{\sigma'}(\boldsymbol{r}')\rangle\Big]-\\ &-f(\boldsymbol{r},\boldsymbol{r}')\ \delta\langle\hat\Psi^\dagger_\sigma(\boldsymbol{r})\hat\Psi_{\sigma'}(\boldsymbol{r}')\rangle\Big\} = 0.\end{aligned} \tag{4.36}$$

Little manipulation on the last equation gives

$$f(\boldsymbol{r},\boldsymbol{r}') = -v(|\boldsymbol{r}-\boldsymbol{r}'|)\langle\hat\Psi^\dagger_{\sigma'}(\boldsymbol{r}')\hat\Psi_\sigma(\boldsymbol{r})\rangle+\sum_{\sigma''}\int d\boldsymbol{r}''\ v(|\boldsymbol{r}-\boldsymbol{r}''|)\langle\hat n_{\sigma''}(\boldsymbol{r}'')\rangle\ \ \delta_{\sigma,\sigma'}\delta(\boldsymbol{r}'-\boldsymbol{r}) \tag{4.37}$$

Inserting (4.37) in (4.28), we obtain $V_{MF}=V_H+V_{exc}$, where

$$V_H = \sum_{\sigma,\sigma'}\int d\boldsymbol{r}d\boldsymbol{r}'\ v(|\boldsymbol{r}-\boldsymbol{r}'|)\langle\hat n_{\sigma'}(\boldsymbol{r}')\rangle_{MF}\,\hat n_\sigma(\boldsymbol{r}), \tag{4.38}$$

$$V_{exc} = -\sum_{\sigma,\sigma'}\int d\boldsymbol{r}d\boldsymbol{r}'\ v(|\boldsymbol{r}-\boldsymbol{r}'|)\langle\hat\Psi^\dagger_{\sigma'}(\boldsymbol{r}')\hat\Psi_\sigma(\boldsymbol{r})\rangle_{MF}\,\hat\Psi^\dagger_\sigma(\boldsymbol{r})\hat\Psi_{\sigma'}(\boldsymbol{r}'). \tag{4.39}$$

At this point, we emphasize that this MF treatment was completely general and independent of the system we are considering. Moreover, it is clear that we can move to the reciprocal space using the exact same procedure that we have described in section 4.1. Besides the prefactors, we only have to keep track of the order of the operators and which ones are averaged. For SLG, we obtain

$$V_H = \frac{1}{NA_{u.c.}} \sum_{\sigma,\sigma'} \sum_{\alpha,\alpha'} \sum_{\substack{\lambda_1,\lambda_2,\\ \lambda_3,\lambda_4}} \sum_{\substack{\boldsymbol{k},\boldsymbol{k}',\\ \boldsymbol{k}''}} \left[c_{\alpha,\lambda_1}(\boldsymbol{k}-\boldsymbol{k}'')\right]^* \left[c_{\alpha',\lambda_2}(\boldsymbol{k}'+\boldsymbol{k}'')\right]^* c_{\alpha',\lambda_3}(\boldsymbol{k}') c_{\alpha,\lambda_4}(\boldsymbol{k}) \times \\ \times v(|\boldsymbol{k}''|) \left\langle \hat{c}^\dagger_{\boldsymbol{k}'+\boldsymbol{k}'',\lambda_2,\sigma'} \hat{c}_{\boldsymbol{k}',\lambda_3,\sigma'} \right\rangle_{MF} \hat{c}^\dagger_{\boldsymbol{k}-\boldsymbol{k}'',\lambda_1,\sigma} \hat{c}_{\boldsymbol{k},\lambda_4,\sigma}, \tag{4.40}$$

$$V_{exc} = -\frac{1}{NA_{u.c.}} \sum_{\sigma,\sigma'} \sum_{\alpha,\alpha'} \sum_{\substack{\lambda_1,\lambda_2,\\ \lambda_3,\lambda_4}} \sum_{\substack{\boldsymbol{k},\boldsymbol{k}',\\ \boldsymbol{k}''}} \left[c_{\alpha,\lambda_1}(\boldsymbol{k}-\boldsymbol{k}'')\right]^* \left[c_{\alpha',\lambda_2}(\boldsymbol{k}'+\boldsymbol{k}'')\right]^* c_{\alpha',\lambda_3}(\boldsymbol{k}') c_{\alpha,\lambda_4}(\boldsymbol{k}) \times \\ \times v(|\boldsymbol{k}''|) \left\langle \hat{c}^\dagger_{\boldsymbol{k}'+\boldsymbol{k}'',\lambda_2,\sigma'} \hat{c}_{\boldsymbol{k},\lambda_4,\sigma} \right\rangle_{MF} \hat{c}^\dagger_{\boldsymbol{k}-\boldsymbol{k}'',\lambda_1,\sigma} \hat{c}_{\boldsymbol{k}',\lambda_3,\sigma'}. \tag{4.41}$$

For the tBLG, we have

$$V_H = \frac{1}{NA_{u.c.}} \sum_{\sigma,\sigma'} \sum_{\substack{\gamma_1(\nu),\gamma_2(\nu'),\\ \gamma_3(\nu'),\gamma_4(\nu)}} \sum_{\substack{\lambda_1,\lambda_2,\\ \lambda_3,\lambda_4}} \sum_{\substack{\boldsymbol{q},\boldsymbol{q}',\\ \boldsymbol{q}''}} \left[c_{\gamma_1(\nu),\lambda_1}(\boldsymbol{q}-\boldsymbol{q}'')\right]^* \left[c_{\gamma_2(\nu'),\lambda_2}(\boldsymbol{q}'+\boldsymbol{q}'')\right]^* c_{\gamma_3(\nu'),\lambda_3}(\boldsymbol{q}') c_{\gamma_4(\nu),\lambda_4}(\boldsymbol{q}) \times \\ \times v(|\boldsymbol{q}''|) \left\langle \hat{c}^\dagger_{\boldsymbol{q}'+\boldsymbol{q}'',\lambda_2,\sigma'} \hat{c}_{\boldsymbol{q}',\lambda_3,\sigma'} \right\rangle_{MF} \hat{c}^\dagger_{\boldsymbol{q}-\boldsymbol{q}'',\lambda_1,\sigma} \hat{c}_{\boldsymbol{q},\lambda_4,\sigma}, \tag{4.42}$$

$$V_{exc} = -\frac{1}{NA_{u.c.}} \sum_{\sigma,\sigma'} \sum_{\substack{\gamma_1(\nu),\gamma_2(\nu'),\\ \gamma_3(\nu'),\gamma_4(\nu)}} \sum_{\substack{\lambda_1,\lambda_2,\\ \lambda_3,\lambda_4}} \sum_{\substack{\boldsymbol{q},\boldsymbol{q}',\\ \boldsymbol{q}''}} \left[c_{\gamma_1(\nu),\lambda_1}(\boldsymbol{q}-\boldsymbol{q}'')\right]^* \left[c_{\gamma_2(\nu'),\lambda_2}(\boldsymbol{q}'+\boldsymbol{q}'')\right]^* c_{\gamma_3(\nu'),\lambda_3}(\boldsymbol{q}') c_{\gamma_4(\nu),\lambda_4}(\boldsymbol{q}) \times \\ \times v(|\boldsymbol{q}''|) \left\langle \hat{c}^\dagger_{\boldsymbol{q}'+\boldsymbol{q}'',\lambda_2,\sigma'} \hat{c}_{\boldsymbol{q},\lambda_4,\sigma} \right\rangle_{MF} \hat{c}^\dagger_{\boldsymbol{q}-\boldsymbol{q}'',\lambda_1,\sigma} \hat{c}_{\boldsymbol{q}',\lambda_3,\sigma'}. \tag{4.43}$$

4.4 Cancellation between electron-ion and Hartree electron-electron terms

In graphene systems, the “ions” are the effective charges, from the carbon atoms, seen by the electrons. As we have seen, there is an effective charge of $+e$ in every carbon atom. Considering the complete Hamiltonian, we have $H = H_0 + V_{ee} + V_{ei} + V_{ii}$ with

$$V_{ei} = \sum_i V_{ei}(\tilde{\boldsymbol{R}}_i), \quad V_{ei}(\tilde{\boldsymbol{R}}_i) = -\sum_\sigma \int d\boldsymbol{r}\; \frac{e^2}{4\pi\varepsilon_r\varepsilon_0|\boldsymbol{r}-\tilde{\boldsymbol{R}}_i|} \hat{n}_\sigma(\boldsymbol{r}), \tag{4.44}$$

$$V_{ii} = \sum_{i\neq j} \frac{e^2}{4\pi\varepsilon_r\varepsilon_0|\tilde{\boldsymbol{R}}_i-\tilde{\boldsymbol{R}}_j|}, \tag{4.45}$$

where $\tilde{\boldsymbol{R}}_i$ is the position of the i^{th} ion. As already stated, we see that, when we apply the variational principle, the presence of V_{ii} does not change anything since $\delta\left\langle V_{ii}\right\rangle_{MF} = 0$. We thus discard this term.

The presence of V_{ei} introduces a new term, $\delta \left\langle V_{ei}\right\rangle_{MF}$, given by

$$\delta \left\langle V_{ei}\right\rangle_{MF} = -\sum_{i}\sum_{\sigma}\int d\boldsymbol{r}\ v(|\boldsymbol{r}-\tilde{\boldsymbol{R}}_i|)\ \delta\left\langle \hat{n}_{\sigma}(\boldsymbol{r})\right\rangle_{MF}. \tag{4.46}$$

We now recover the term in $\delta \left\langle V_{ee}\right\rangle_{MF}$ (eq. (4.30)) which led to the Hartree term,

$$\delta \left\langle V_{ee}\right\rangle_{MF}^{H} = \sum_{\sigma,\sigma'}\int d\boldsymbol{r}d\boldsymbol{r}'\ v(|\boldsymbol{r}-\boldsymbol{r}'|)\ \left\langle \hat{n}_{\sigma'}(\boldsymbol{r}')\right\rangle_{MF}\delta\left\langle \hat{n}_{\sigma}(\boldsymbol{r})\right\rangle_{MF}. \tag{4.47}$$

For homogeneous neutral graphene, the density of electrons is uniformly distributed and we may argue that, on average, we have one electron (out of 2, due to spin degeneracy) for each ion position. Mathematically, we write

$$\sum_{\sigma'}\left\langle \hat{n}_{\sigma'}(\boldsymbol{r}')\right\rangle_{MF} = \sum_{i}\delta(\boldsymbol{r}'-\tilde{\boldsymbol{R}}_i), \tag{4.48}$$

and we verify the cancellation of (4.46) and (4.47). This is the lattice analogue of the well-known continuum long wavelength cancellation used in the Jellium model [64].

At last, we warn that, when we vary the Fermi level, we are in pratice doping graphene with electrons or holes. Therefore, we do not have neutral graphene in this situation. Nevertheless, we may argue that, taking into account the whole physical system (graphene + capacitor), this cancellation still holds. From the point of view of graphene alone, the Hartree correction in this case implies just a constant energy shift of the bands, which corresponds to the classical energy due to the other parallel capacitor plate.

4.5 Band renormalization — self-energy

Let us briefly summarize what we have accomplished so far. We introduced the effects of electron-electron interactions by writing an Hamiltonian $H = H_0 + V_{ee} + V_{ei} + V_{ii}$. Within a MF approximation, we obtained a simplified 1-particle description of H, $H_{MF} = H_0 + V_{MF}$ where V_{MF} was shown to be the exchange term in the HF approximation, $V_{MF} = V_{exc}$. In particular, for SLG, we obtained

$$V_{exc} = -\frac{1}{NA_{u.c.}}\sum_{\sigma,\sigma'}\sum_{\alpha,\alpha'}\sum_{\substack{\lambda_1,\lambda_2,\\ \lambda_3,\lambda_4}}\sum_{\substack{\boldsymbol{k},\boldsymbol{k}',\\ \boldsymbol{k}''}}\left[c_{\alpha,\lambda_1}(\boldsymbol{k}-\boldsymbol{k}'')\right]^*\left[c_{\alpha',\lambda_2}(\boldsymbol{k}'+\boldsymbol{k}'')\right]^* c_{\alpha',\lambda_3}(\boldsymbol{k}')c_{\alpha,\lambda_4}(\boldsymbol{k})\times$$
$$\times\ v(|\boldsymbol{k}''|)\left\langle \hat{c}^{\dagger}_{\boldsymbol{k}'+\boldsymbol{k}'',\lambda_2,\sigma'}\hat{c}_{\boldsymbol{k},\lambda_4,\sigma}\right\rangle_{MF}\hat{c}^{\dagger}_{\boldsymbol{k}-\boldsymbol{k}'',\lambda_1,\sigma}\hat{c}_{\boldsymbol{k}',\lambda_3,\sigma'}. \tag{4.49}$$

Assuming that $\{\boldsymbol{k},\lambda,\sigma\}$ are still good quantum numbers even when using the MF approximation —meaning that the ground state is assumed to preserve the translational invariance of the lattice and that the description in a set of bands λ is still valid—, we see that

$$\boldsymbol{k}'+\boldsymbol{k}'' = \boldsymbol{k}+\boldsymbol{G} \Leftrightarrow \boldsymbol{k}'' = \boldsymbol{k}-\boldsymbol{k}'+\boldsymbol{G},\quad \lambda_1=\lambda_3,\quad \lambda_2=\lambda_4,\quad \sigma=\sigma', \tag{4.50}$$

where $\boldsymbol{G}$ is a graphene reciprocal basis vector. Eq. (4.49) can be further simplified if we keep only the

$\boldsymbol{G} = \boldsymbol{0}$ term, which should be the leading correction to the non-interacing theory. We get

$$V_{exc} = -\frac{1}{NA_{u.c.}} \sum_{\sigma} \sum_{\alpha,\alpha'} \sum_{\substack{\lambda_1,\lambda_2,\\ \lambda_3}} \sum_{\boldsymbol{k},\boldsymbol{k}'} \left[c_{\alpha,\lambda_1}(\boldsymbol{k}')\right]^* \left[c_{\alpha',\lambda_2}(\boldsymbol{k})\right]^* c_{\alpha',\lambda_3}(\boldsymbol{k}') c_{\alpha,\lambda_2}(\boldsymbol{k}) \times$$
$$\times\, v(|\boldsymbol{k}-\boldsymbol{k}'|) \left\langle \hat{c}^{\dagger}_{\boldsymbol{k},\lambda_2,\sigma} \hat{c}_{\boldsymbol{k},\lambda_2,\sigma} \right\rangle_{MF} \hat{c}^{\dagger}_{\boldsymbol{k}',\lambda_1,\sigma} \hat{c}_{\boldsymbol{k}',\lambda_1,\sigma}. \tag{4.51}$$

Notice that the average $\langle ... \rangle_{MF}$ must be done with respect to the new one-body Hamiltonian; this is the socalled self-consistent HF approximation. In the non self-consistent approach, the first correction is obtained by doing the average $\langle ... \rangle_{MF}$ with respect to the bare Hamiltonian, H_0. This leads to

$$V_{exc} = \sum_{\sigma} \sum_{\boldsymbol{k},\lambda} \Sigma_{\lambda}(\boldsymbol{k}) \hat{c}^{\dagger}_{\boldsymbol{k},\lambda,\sigma} \hat{c}_{\boldsymbol{k},\lambda,\sigma}, \tag{4.52}$$

with

$$\begin{aligned} \Sigma_{\lambda}(\boldsymbol{k}) &= -\frac{1}{NA_{u.c.}} \sum_{\alpha,\alpha'} \sum_{\boldsymbol{k}',\lambda'} \left[c_{\alpha,\lambda}(\boldsymbol{k})\right]^* \left[c_{\alpha',\lambda'}(\boldsymbol{k}')\right]^* c_{\alpha',\lambda}(\boldsymbol{k}) c_{\alpha,\lambda'}(\boldsymbol{k}') v(|\boldsymbol{k}-\boldsymbol{k}'|)\ \left\langle \hat{c}^{\dagger}_{\boldsymbol{k}',\lambda',\sigma} \hat{c}_{\boldsymbol{k}',\lambda',\sigma} \right\rangle_0 \\ &= -\frac{1}{NA_{u.c.}} \sum_{\alpha,\alpha'} \sum_{\boldsymbol{k}',\lambda'} \left[c_{\alpha,\lambda}(\boldsymbol{k})\right]^* \left[c_{\alpha',\lambda'}(\boldsymbol{k}')\right]^* c_{\alpha',\lambda}(\boldsymbol{k}) c_{\alpha,\lambda'}(\boldsymbol{k}') v(|\boldsymbol{k}-\boldsymbol{k}'|)\ n_F\left(\epsilon^0_{\lambda'}(\boldsymbol{k}')\right), \end{aligned} \tag{4.53}$$

where n_F is the Fermi-Dirac function and $\epsilon^0_{\lambda'}(\boldsymbol{k}')$ are the eigenvalues for the bare Hamiltonian. Looking at (4.52), we recognize $\Sigma_{\lambda}(\boldsymbol{k})$ as a self-energy term. Band renormalization is thus obtained in the following manner: for a given $\boldsymbol{k}$-state in band λ, the renormalized band energy is given by

$$\epsilon_{\lambda}(\boldsymbol{k}) = \epsilon^0_{\lambda}(\boldsymbol{k}) + \Sigma_{\lambda}(\boldsymbol{k}). \tag{4.54}$$

We stress that, since we have retained the $\boldsymbol{G} = \boldsymbol{0}$ term, the sum over $\boldsymbol{k}'$ in (4.53) should be done in a BZ centered close to the $\boldsymbol{k}$-point we intend to describe. Otherwise, we may miss important contributions arising from small values of $|\boldsymbol{k}-\boldsymbol{k}'|$.

We now compare our expression (4.53) to eq. (13) from Roldán et al. [63], obtained through a diagrammatic technique,

$$\Sigma_{\lambda}(\boldsymbol{k}) = -\sum_{\lambda'} \int_{BZ} \frac{d\boldsymbol{q}}{(2\pi)^2}\ v(|\boldsymbol{q}|)\ F_{\lambda,\lambda'}(\boldsymbol{k},\boldsymbol{k}+\boldsymbol{q})\ \Theta(\mu - \epsilon^0_{\lambda'}(\boldsymbol{k}+\boldsymbol{q})). \tag{4.55}$$

Apart from the fact that we are considering different Coulomb interactions (they combine long and short range Coulomb potentials), if we take $T \to 0$ (which implies our Fermi-Dirac function to become a step function) and if we write $\boldsymbol{k}' = \boldsymbol{k} + \boldsymbol{q}$ and alternate from the sum over $\boldsymbol{q} \in BZ$ to an integral, the expressions start looking very similar. Using the analytical expressions for the SLG eigenvectors (which can be trivially derived),

$$\begin{bmatrix} u_1^{\lambda}(\boldsymbol{k}) \\ u_2^{\lambda}(\boldsymbol{k}) \end{bmatrix} = \frac{1}{\sqrt{2}} \begin{bmatrix} 1 \\ -\lambda \frac{|f(\boldsymbol{k})|}{f(\boldsymbol{k})} \end{bmatrix} \equiv \begin{bmatrix} c_{A,\lambda}(\boldsymbol{k}) \\ c_{B,\lambda}(\boldsymbol{k}) \end{bmatrix}, \tag{4.56}$$

where $f(\boldsymbol{k})$ is given by (2.17), we compute the sum

$$\sum_{\alpha,\alpha'} \left[c_{\alpha,\lambda}(\boldsymbol{k})\right]^* \left[c_{\alpha',\lambda'}(\boldsymbol{k}+\boldsymbol{q})\right]^* c_{\alpha',\lambda}(\boldsymbol{k}) c_{\alpha,\lambda'}(\boldsymbol{k}+\boldsymbol{q}) = \frac{1}{4}\left|1+\lambda\lambda'\frac{f(\boldsymbol{k})f^*(\boldsymbol{k}+\boldsymbol{q})}{|f(\boldsymbol{k})f(\boldsymbol{k}+\boldsymbol{q})|}\right|^2 \equiv F_{\lambda,\lambda'}(\boldsymbol{k},\boldsymbol{k}+\boldsymbol{q}) \quad (4.57)$$

and we verify that the expressions match precisely. Moreover, we see that the problem of centering the sum/integral is already addressed when we changed from summing in $\boldsymbol{k}'$ to a sum over $\boldsymbol{q}$ with $\boldsymbol{k}' = \boldsymbol{k}+\boldsymbol{q}$.

The tBLG treatment

In this case, we retain the term $\boldsymbol{G}^m = \boldsymbol{0}$, which also implies that our sum over $\boldsymbol{q}'$ should be done in a mBZ centered around $\boldsymbol{q}$. The remaining steps are completely identical and we obtain

$$\Sigma_\lambda(\boldsymbol{q}) = -\frac{1}{NA_{g.u.c.}} \sum_{\substack{\gamma_1(\nu),\gamma_2(\nu'),\\ \gamma_3(\nu'),\gamma_4(\nu)}} \sum_{\boldsymbol{q}',\lambda'} \left[c_{\gamma_1(\nu),\lambda}(\boldsymbol{q})\right]^* \left[c_{\gamma_2(\nu'),\lambda'}(\boldsymbol{q}')\right]^* c_{\gamma_3(\nu'),\lambda}(\boldsymbol{q}) c_{\gamma_4(\nu),\lambda'}(\boldsymbol{q}') \times \\ \times v(|\boldsymbol{q}-\boldsymbol{q}'|)\, n_F\left(\epsilon^0_{\lambda'}(\boldsymbol{q}')\right). \quad (4.58)$$

Here, it is worth to recall that we are splitting the treatment of K and K' bands. This separation is implicit when we write the wave vectors.

4.6 Self-energy results for single layer graphene

Here, we focus on studying the band renormalization near the Dirac point K at $T = 0\text{K}$ [1]. We stress that, after computing the self-energy, the zero energy must be redefined because we are now taking into consideration the Coulomb repulsion between the electrons and, therefore, the bands are shifted to negative energies. In order to do so, we matched all the spectra by defining the zero energy as the situation of half-filling. We also note that, when we do not consider screening, the terms $\boldsymbol{k}' = \boldsymbol{k}$ in the sum (4.53) must be eliminated.

In fig. 4.1(a), we present results for the SLG. When screening is not taken into account, we observe points with infinite slope (black dots marked in the figure) that appear at the Fermi surface of the renormalized spectrum. This is in agreement with ref. [64] (see fig. 5.1 in the page 383). When we consider TF screening, we conclude that the electronic structure is basically maintained, with just a slight renormalization —in particular, an increase— of the Fermi velocity; qualitatively, this behavior was also verified in Roldán et al. [63].

Let us now illustrate the physics that led us to consider the effect of electron-electron interactions as a possible source for the gap renormalization observed experimentally in ref. [31] (see section 3.1.3 and fig. 3.5(a)). To that purpose, we took the SLG Hamiltonian (2.18) and introduced a gap Δ between the

---

[1] The dependency on the temperature was actually verified to be unimportant.

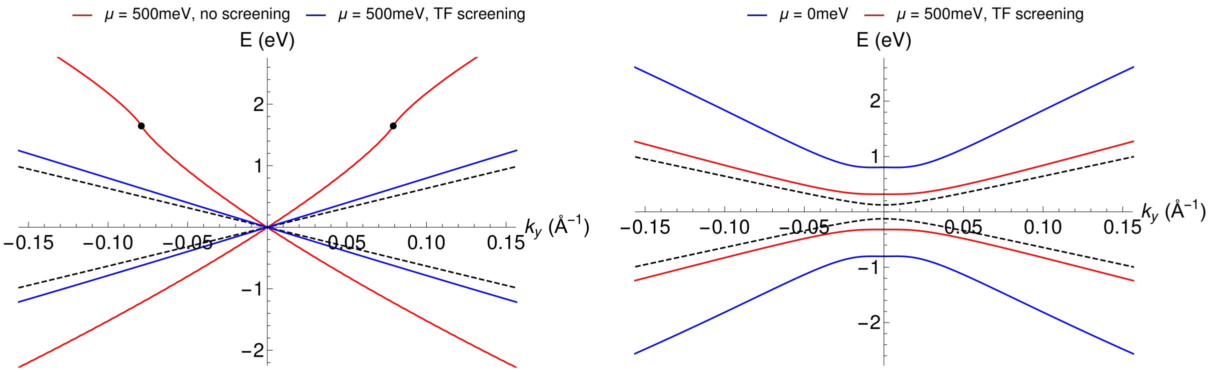

(a) SLG

(b) SLG with gap

Figure 4.1: Renormalized bands near the K point for: (a) SLG; (b) SLG with a gap $\Delta = 250$meV. In both graphics, the dashed black line corresponds to the bare/noninteracting spectrum; moreover, we have $k_x = \frac{4\pi}{3\sqrt{3}d} \simeq 1.703\text{Å}^{-1}$.

valence and the conduction bands by writting

$$H^{\Delta}_{SLG}(\boldsymbol{k}) = \begin{bmatrix} \Delta/2 & -tf(\boldsymbol{k}) \\ -tf^*(\boldsymbol{k}) & -\Delta/2 \end{bmatrix}. \tag{4.59}$$

Then, we computed the band renormalization for this Hamiltonian, obtaining the results from fig. 4.1(b). We first stress that, for $\mu = 0$meV, although the TF screening is null, we considered a small value for q_{TF} which we may interpret as a disorder effect or as residual screening coming from the sp_2 orbitals; nevertheless, the results were not substantially altered by this. From the figure, we conclude that the gaps are enhanced and that this enhacement is larger when the Fermi level is placed at the gap. Although we cannot conclude anything for the tBLG, in particular the desired explanation for the experimental results discussed before, the results obtained here for the SLG with gap may indicate that the consideration of electron-electron effects could be a key to explain, to some extent, this pronounced insulator behavior.

4.7 A word on the implementation for the twisted bilayer graphene

We tried to apply the same method to compute the self-energy for the tBLG system with $\theta = 1.8°$ near the Γ_m point. Since the self-energy computation is numerically heavy (even for the SLG), we used the smallest effective Hamiltonian that still captures the first bands and, in particular, the band gap observed at the Γ_m point (fig. 3.5(b)). The Hamiltonian used was 38×38 ($NN = 3$) and we considered the first 4 bands closer to the zero energy, which are the ones that are still reasonably described. Notice that, even with this simplification, the complexity of the diagonalization is much greater. In addition, looking at (4.58), we also see that this numerical implementation has two more sums/cycles, comparing with the SLG (4.53). With all this in mind, we still performed the numerical computation using a good precision in the discretization of the sum over momentum [2], but the results obtained were senseless. We believe this happened because we only considered the first 4 bands: if we think in the folded picture,

---

[2] We set roughly the same number of $\boldsymbol{k}$-points per unit cell in reciprocal space, comparing to the SLG calculation.

when we unfold the spectrum, the first 4 bands may not cover a sufficiently wide area of the (unfolded) BZ to make the results valid. However, we cannot increase the number of (well described) bands without increasing the dimension of the Hamiltonian, and therefore, the time of calculation. Moreover, we are using a Dirac cone approximation so, even if we wanted to perform a very long calculation with all the bands, we would never be able to define a finite Hamiltonian (not even for the commensurate case). In conclusion, the numerical implementation of (4.58) for effective Hamiltonians is something that we still could not establish. Yet, we settled that, as benchmark, we should first try to make these calculations for the K_m point, since we do not expect major modifications in the renormalized spectrum near this point (similarly to what we saw for the SLG). In this context, one strategy that we will follow in the future is to incorporate a cutoff (in the bands) and compute the self-energy for the tBLG at the K_m point, without interlayer coupling [3], comparing it with the results for the SLG. With this, we hope to understand how the cutoff afects the computation and how to calibrate this cutoff properly.

---

[3] We believe that the interlayer coupling will not change considerably the results if the energy scale of the cutoff is sufficiently higher than the coupling.

Chapter 5

Conclusions and future work

In chapter 2 of this dissertation, we derived a semi-analytical model for the tBLG, which was the foundation for the whole work. We mainly followed ref. [26] but we also kept on track with the differences and similarities of the treatments made in other relevant papers within this subject. From our derivation, we highlight section 2.3.4, where we provided more detail (specially when compared to our main reference) on the computation of the FT for the interlayer hopping. With the spectrum reconstruction established, we also computed the profiles of the DOS and the carrier density, wherefore we consider the objectives 1-3 to be fully accomplished. The principal conclusion of this chapter is that the electronic spectrum is strongly modified by varying the twist angle, namely by bringing van Hove singularities to lower energies and thus making them easily accessible to the electrons.

The calculation of the optical conductivity —objective 4— was addressed in section 3.1. Using linear response theory, we derived general expressions for computing the homogeneous dynamical conductivity from a spin-independent tight-binding Hamiltonian of a periodic system. A discussion of the best implementation methods for effective low-energy Hamiltonians was also provided. Here, as our own contribution, we highlight the 2^{nd} method that we introduced to compute the Drude weight, which can easily be applied. We also emphasize the work that we reproduced from ref. [34], which enables us to compute the imaginary part of the regular conductivity by using regularized KK relations; despite the lack of physical meaning of the imaginary part, it is important to compute it in order to study the plasmonic response. The results obtained for the tBLG were verified to be in agreement with the (few) existent references related to this topic. As major conclusions, we retain the forbidden optical transitions between symmetric bands in the M_m point (firstly explained in ref. [33]) and the fact that the conductivity profiles can be drastically modified —even for low frequencies and/or little doping levels— by varying the twist angle. At this moment, we have a collaboration with an investigation group from Brazil and we are waiting for experimental measurements of the optical conductivity in the tBLG to publish our results together; we stress that the results obtained in this thesis are consistent with the results obtained from DFT calculations by this group.

The computation of reflectance, transmittance and absorption (objective 5) was left for future work.

With the calculation of the optical conductivity established (both the real and imaginary parts), we

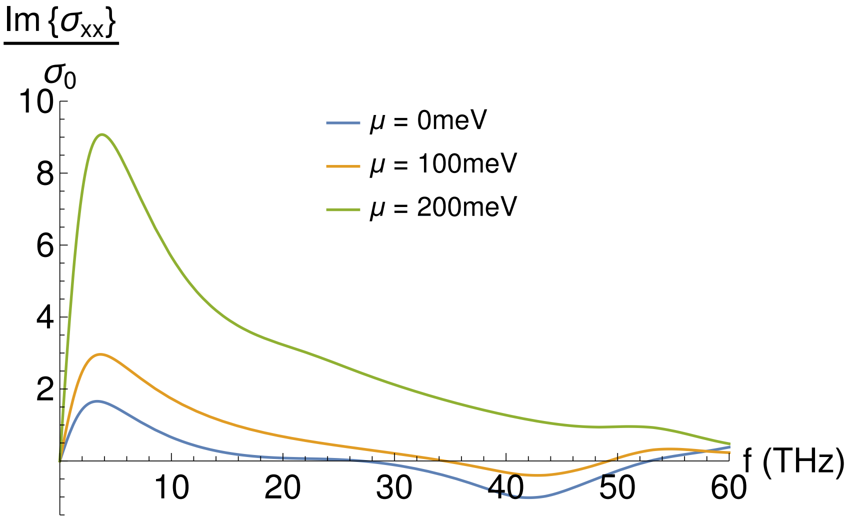

Figure 5.1: Imaginary part of the total conductivity for tBLG with $\theta = 1.8°$. We extended the frequency range to show that the region where TE modes appear is close, and can eventually be reached by tuning the twist angle.

finally dived into the 6^{th} objective —the study of the plasmonic response, in particular the spectrum of GSPPs, which, for tBLG systems, is an absent topic in literature (as far as we know). In section 3.2, we derived the equation for the TM modes and then computed the results for the tBLG. As key achievement, we underscore the results from fig. 3.14(b), which may be used, for example, as an alternative method for determining the twist angle. Although we already have original results in this section, a more extensive study on the behavior of these curves with the variation of θ still remains to be done. In addition, we also leave for future work the study of the transverse electric (TE) modes, which are the ones that, in contrast to the TM modes, exist only when $\text{Im}\{\sigma(\omega)\} < 0$ [19]. In the low frequency range (in which we are interested), the Drude contribution —which yields a positive imaginary conductivity— is typically the dominant term; however, as we can see in fig. 5.1, we may tune the parameters so that we have negative terms in some low-frequency region, and therefore these TE modes can become worthy of investigation.

Finally, in chapter 4, we tackled the last objective of studying the effects of electron-electron interactions in the tBLG. Within a MF/HF approach, we derived an expression for the self-energy correction to the band spectrum, which was confirmed to be in agreement with the literature for the simpler case of a SLG. Although we could not obtain the results for the tBLG (a discussion on the problems concerning the numerical implementation was given in section 4.7), we believed to have taken a step in the right direction on a topic which we expect to cover in future works, specially since it is completely unexplored yet. Nevertheless, from the results obtained for the SLG, we were still able to infer that, when in the presence of a gap, the bandgap renormalization should open it, which may explain, to some extent, the experimental measurements from ref. [31] that indicated a pronounced insulator behavior (see discussion in section 3.1.3). At last, the investigation of magnetic instabilities was not addressed at all and was also left for future work. In short, the idea here is that the divergent DOS on the low-energy van Hove singularities that occur in the tBLG should result in some sort of magnetic instability.

Bibliography

[1] A. K. Geim and I. V. Grigorieva. Van der Waals heterostructures. *Nature*, 499(7459):419–425, 2013.

[2] K. S. Novoselov, A. Mishchenko, A. Carvalho, and A. H. C. Neto. 2D materials and van der Waals heterostructures. *Science*, 353(6298):aac9439, 2016.

[3] M. Massicotte, P. Schmidt, F. Vialla, K. G. Schädler, A. Reserbat-Plantey, K. Watanabe, T. Taniguchi, K. J. Tielrooij, and F. H. L. Koppens. Picosecond photoresponse in van der Waals heterostructures. *Nature nanotechnology*, 11(1):42–46, 2015.

[4] A. K. Geim and A. H. MacDonald. Graphene: exploring carbon flatland. *Phys. Today*, 60(8):35–41, 2007.

[5] R. Peierls. Quelques propriétés typiques des corps solides. *Annales de l'institut Henri Poincaré*, 5 (3):177–222, 1935.

[6] L. D. Landau. Zur Theorie der phasenumwandlungen II. *Phys. Z. Sowjetunion*, 11:26–35, 1937.

[7] N. D. Mermin. Crystalline order in two dimensions. *Phys. Rev.*, 176(1):250–254, 1968.

[8] K. S. Novoselov, D. Jiang, T. Booth, V. V. Khotkevich, S. M. Morozov, and A. K. Geim. Two-dimensional atomic crystals. *PNAS*, 102(30):10451–10453, 2005.

[9] A. Fasolino, J. H. Los, and M. I. Katsnelson. Intrinsic ripples in graphene. *Nat. Mater.*, 6(11): 858–861, 2007.

[10] M. I. Katsnelson. *Graphene: carbon in two dimensions*. Cambridge University Press, 2012.

[11] K. S. Novoselov and A. H. C. Neto. Two-dimensional crystals-based heterostructures: materials with tailored properties. *Phys. Scr.*, T146:014006, 2012.

[12] A. K. Geim. Graphene: status and prospects. *Science*, 324(5934):1530–1534, 2009.

[13] A. H. C.Neto, F. Guinea, N. M. R. Peres, K. S. Novoselov, and A. K. Geim. The electronic properties of graphene. *Rev. Mod. Phys.*, 81(1):109, 2009.

[14] The Royal Swedish Academy of Sciences. Scientific background on the Nobel prize in physics 2010 graphene, 2010. URL `http://www.nobelprize.org/nobel_prizes/physics/laureates/2010/press.html`.

[15] S. C. O'Hern, M. S. H. Boutilier, J. Idrobo, Y. Song, J. Kong, T. Laoui, M. Atieh, and R. Karnik. Selective ionic transport through tunable subnanometer pores in single-layer graphene membranes. *Nano Lett.*, 14(3):1234–1241, 2014.

[16] IdTechEx. Graphene, 2D materials and carbon nanotubes: markets, technologies and opportunities 2015-2025. Technical report, IdTechEx, 2015.

[17] A. V. Rozhkov, A. O. Sboychakov, A. I. Rakhmanov, and F. Nori. Electronic properties of graphene-based bilayer systems. *arXiv preprint arXiv:1511.06706*, 2015.

[18] X. Luo, T. Qiu, W. Lu, and Z. Ni. Plasmons in graphene: recent progress and applications. *Materials Science & Engineering, R: Reports*, 74(11):351–376, 2013.

[19] P. A. D. Gonçalves and N. M. R. Peres. *An introducion to graphene plasmonics.* World Scientific Publishing Co. Pte. Ltd., 2016.

[20] J. M. B. L. dos Santos, N. M. R. Peres, and A. H. C. Neto. Continuum model of the twisted graphene bilayer. *Phys. Rev. B*, 86(15):155449, 2012.

[21] I. Brihuega, P. Mallet, H. González-Herrero, G. T. de Laissardière, M. M. Ugeda, L. Magaud, J. Gómez-Rodríguez, F. Ynduráin, and J.-Y. Veuillen. Unravelling the intrinsic and robust nature of van Hove singularities in twisted bilayer graphene. *Phys. Rev. Lett.*, 109(19):196802, 2012.

[22] G. T. de Laissardière, D. Mayou, and L. Magaud. Numerical studies of confined state in rotated bilayer of graphene. *Phys. Rev.*, 86(12):125413, 2012.

[23] E. S. Morell, J. D. Correa, P. Vargas, M. Pacheco, and Z. Barticevic. Flat bands in slightly twisted bilayer graphene: tight-binding calculations. *Phys. Rev. B*, 82(12):121407, 2010.

[24] S. Latil, V. Meunier, and L. Henrard. Massless fermions in multilayer graphitic systems with misoriented layers: ab initio calculations and experimental fingerprints. *Phys. Rev. B*, 76(20):201402, 2007.

[25] J. M. B. L. dos Santos, N. M. R. Peres, and A. H. C. Neto. Graphene bilayer with a twist: electronic structure. *Phys. Rev. Lett.*, 99(25):256802, 2007.

[26] R. Bistritzer and A. H. MacDonald. Moiré bands in twisted double-layer graphene. *PNAS*, 108(30): 12233–12237, 2011.

[27] R. de Gail, M. O. Goerbig, F. Guinea, G. Montambaux, and A. H. C. Neto. Topologically protected zero modes in twisted bilayer graphene. *Phys. Rev. B*, 84(4):045436, 2011.

[28] D. Weckbecker, S. Shallcross, M. Fleischmann, N. Ray, S. Sharma, and O. Pankratov. Low-energy theory for the graphene twist bilayer. *Phys. Rev. B*, 93(3):035452, 2016.

[29] Y. Wang, Z. Ni, L. Liu, Y. Liu, C. Cong, T. Yu, X. Wang, D. Shen, and Z. Shen. Stacking dependent optical conductivity of bilayer graphene. *ACS nano*, 4(7):4074–4080, 2010.

[30] X. Zou, J. Shang, J. Leaw, Z. Luo, L. Luo, C. L. o vorakiat, L. Cheng, S. A. Cheong, H. Su, J.-X. Zhu, Y. Liu, K. P. Loh, A. H. C. Neto, and T. Y. E. E. M. Chia. Terahertz conductivity of twisted bilayer graphene. *Phys. Rev. Lett.*, 110(6):067401, 2013.

[31] Y. Cao, J. Y. Luo, V. Fatemi, S. Fang, J. D. Sanchez-Yamagishi, K. Watanabe, T. Taniguchi, E. Kaxiras, and P. Jarillo-Herrero. Superlattice-induced insulating states and valley-protected orbits in twisted bilayer graphene. *Phys. Rev. Lett.*, 117(11):116804, 2016.

[32] C. Tabert and E. Nicol. Optical conductivity of twisted bilayer graphene. *Phys. Rev. B*, 87(12): 121402, 2013.

[33] P. Moon and M. Koshino. Optical absorption in twisted bilayer graphene. *Phys. Rev. B*, 87(20): 205404, 2013.

[34] T. Stauber, P. San-Jose, and L. Brey. Optical conductivity, Drude weight and plasmons in twisted graphene bilayers. *New J. Phys.*, 15(11):113050, 2013.

[35] L. Ju, B. Geng, J. Horng, C. Girit, M. Martin, Z. Hao, H. A. Bechtel, X. Liang, A. Zettl, Y. R. Shen, and F. Wang. Graphene plasmonics for tunable terahertz metamaterials. *Nature nanotechnology*, 6 (10):630–634, 2011.

[36] M. Jablan, H. Buljan, and M. Soljačić. Plasmonics in graphene at infra-red frequencies. *Phys. Rev. B*, 80(24):245435, 2009.

[37] F. H. L. Koppens, D. E. Chand, and F. J. G. de Abajo. Graphene plasmonics: a platform for strong light–matter interactions. *Nano Lett.*, 11(8):3370–3377, 2011.

[38] Z. Fang, Y. Wang, Z. Liu, A. Schlather, P. M. Ajayan, F. H. L. Koppens, P. Nordlander, and N. J. Halas. Plasmon-induced doping of graphene. *ACS nano*, 6(11):10222–10228, 2012.

[39] A. Vakil and N. Engheta. Transformation optics using graphene. *Science*, 332(6035):1291–1294, 2011.

[40] A. N. Grigorenko, M. Polini, and K. S. Novoselov. Graphene plasmonics. *Nat. Photonics*, 6(11): 749–758, 2012.

[41] Z. Fei, A. S. Rodin, G. O. Andreev, W. Bao, A. S. McLeod, M. Wagner, L. M. Zhang, Z. Zhao, M. T. ang G. Dominguez, M. M. Fogler, A. H. C. Neto, C. N. Lau, F. Keilmann, and D. N. Basov. Gate-tuning of graphene plasmons revealed by infrared nano-imaging. *Nature*, 487(7405):82–85, 2012.

[42] J. Chen, M. Badioli, P. Alonso-González, S. Thongrattanasiri, F. Huth, J. Osmond, M. Spasenović, A. Centeno, A. Pesquera, P. Godignon, A. Zurutuza, N. Camara, J. G. de Abajo, R. Hillenbrand, and F. Koppens. Optical nano-imaging of gate-tuneable graphene plasmons. *Nature*, 487(7405): 77–81, 2012.

[43] S. Reich, J. Maultzsch, and C. Thomsen. Tight-binding description of graphene. *Phys. Rev. B*, 66 (3):035412, 2002.

[44] D. K. Efetov and P. Kim. Controlling electron-phonon interactions in graphene at ultrahigh carrier densities. *Phys. Rev. Lett.*, 105(25):256805, 2010.

[45] A. Das, S. Pisana, B. Chakraborty, S. Piscanec, S. K. Saha, U. V. Waghmare, K. S. Novoselov, H. R. Krishnamurthy, A. K. Geim, A. C. Ferrari, and A. K. Sood. Monitoring dopants by Raman scattering in an electrochemically top-gated graphene transistor. *Nature nanotechnology*, 3(4):210–215, 2008.

[46] K. F. Mak, C. H. Lui, J. Shan, and T. F. Heinz. Observation of an electric-field-induced band gap in bilayer graphene by infrared spectroscopy. *Phys. Rev. Lett.*, 102(25):256405, 2009.

[47] J. Yan, T. Villarson, E. A. Henriksen, P. Kim, and A. Pinczuk. Optical phonon mixing in bilayer graphene with a broken inversion symmetry. *Phys. Rev. B*, 80(24):241417, 2009.

[48] J. González. Kohn-Luttinger superconductivity in graphene. *Phys. Rev. B*, 78(20):205431, 2008.

[49] M. Fleck, A. M. Oleś, and L. Hedin. Magnetic phases near the van Hove singularity in s-and d-band Hubbard models. *Phys. Rev. B*, 56(6):3159, 1997.

[50] R. Nandkishore, L. S. Levitov, and A. V. Chubukov. Chiral superconductivity from repulsive interactions in doped graphene. *Nature Physics*, 8(2):158–163, 2012.

[51] G. Li, A. Luican, J. M. B. L. dos Santos, A. H. C. Neto, A. Reina, J. Kong, and E. Y. Andrei. Observation of van Hove singularities in twisted graphene layers. *Nature Physics*, 6(2):109–113, 2010.

[52] C. Bena and G. Montambaux. Remarks on the tight-binding model of graphene. *New J. Phys.*, 11 (9):095003, 2009.

[53] J. C. Slater and G. F. Koster. Simplified LCAO method for the periodic potential problem. *Phys. Rev.*, 94(6):1498–1524, 1954.

[54] A. Kretinin, G. L. Yu, R. Jalil, Y. Cao, F. Withers, A. Mishchenko, M. I. Katsnelson, K. S. Novoselov, A. K. Geim, and F. Guinea. Quantum capacitance measurements of electron-hole asymmetry and next-nearest-neighbor hopping in graphene. *Phys. Rev. B*, 88(16):165427, 2013.

[55] N. A. Doughty. *Lagrangian interaction.* Addison-Wesley, 1990.

[56] N. W. Ashcroft and N. D. Mermin. *Solid state physics.* Harcourt College Publishers, 1976.

[57] C. Kittel. *Introduction to solid state physics.* John Wiley & Sons, 1966.

[58] T. Stauber, N. M. R. Peres, and A. K. Geim. The optical conductivity of graphene in the visible region of the spectrum. *Phys. Rev. B*, 78(8):085432, 2008.

[59] Z. Q. Li, E. A. Henriksen, Z. Jiang, Z. Hao, M. C. Martin, P. Kim, H. L. Stormer, and D. N. Basov. Dirac charge dynamics in graphene by infrared spectroscopy. *Nature Physics*, 4(7):532–535, 2008.

[60] S. V. Morozov, K. S. Novoselov, M. I. Katsnelson, F. Schedin, D. C. Elias, J. A. Jaszczak, and A. K. Geim. Giant intrinsic carrier mobilities in graphene and its bilayer. *Phys. Rev. Lett.*, 100(1):016602, 2008.

[61] A. K. Geim and K. S. Novoselov. The rise of graphene. *Nat. Mater.*, 6(3):183–191, 2007.

[62] Y. V. Bludov, A. Ferreira, N. M. R. Peres, and M. I. Vasilevskiy. A primer on surface plasmon-polaritons in graphene. *Int. J. Mod. Phys. B*, 27(10):1341001, 2013.

[63] R. Roldán, M. P. López-Sancho, and F. Guinea. Effect of electron-electron interaction on the Fermi surface topology of doped graphene. *Phys. Rev. B*, 77(11):115410, 2008.

[64] G. D. Mahan. *Many-particle physics.* Springer Science & Business Media, 2013.

[65] E. J. S. Lage. *Física estatística.* Fundação Calouste Gulbenkian, 1995.

Appendix A

Density of states and carrier density: numerical implementation

A.1 Density of states

We start by introducing the general definition,

$$DOS(E) = \sum_{\boldsymbol{k}\in BZ,\lambda,\sigma} \delta\left(E - E_\lambda^\sigma(\boldsymbol{k})\right), \tag{A.1}$$

where $E_\lambda^\sigma(\boldsymbol{k})$ are the eigenvalues for momentum $\boldsymbol{k}$, band λ and spin σ and δ stands for the Dirac delta function. When our spectrum does not depend explicitly on the spin, we simplify (A.1) into

$$DOS(E) = 2\sum_{\boldsymbol{k}\in BZ,\lambda} \delta\left(E - E_\lambda(\boldsymbol{k})\right). \tag{A.2}$$

We now give insight to this expression. The easiest way to understand it is by integrating the DOS in some energy interval, let us say between E_1 and E_2. We obtain

$$\int_{E_1}^{E_2} dE\ DOS(E) = 2\sum_{\boldsymbol{k}\in BZ,\lambda} \int_{E_1}^{E_2} dE\ \delta\left(E - E_\lambda(\boldsymbol{k})\right). \tag{A.3}$$

Looking at the right hand side, we observe that the integral equals 1 whenever $E_1 \le E_\lambda(\boldsymbol{k}) \le E_2$ and 0 otherwise. Therefore, we are basically counting all states (with a multiplicity of 2 due to spin degeneracy) within the energy range, which is exactly what we expect from definition. With this in mind, we can now establish a general numerical method to compute the DOS from an arbitrary electronic spectrum. We first notice that, when we have a finite system, we typically apply periodic boundary conditions (PBC) which imply that our (in principle infinite) sum in $\boldsymbol{k} \in BZ$ becomes constrained to N_1N_2 terms. For general reciprocal basis vectors $\boldsymbol{b}_1$ and $\boldsymbol{b}_2$, the trivial discretization is

$$\boldsymbol{k} = \frac{m_1}{N_1}\boldsymbol{b}_1 + \frac{m_2}{N_2}\boldsymbol{b}_2\ , \quad m_i = 0, 1, ..., N_i - 1. \tag{A.4}$$

Then, we take the limit $E_2 = E_1 + \Delta E$, for small ΔE, and write

$$\begin{aligned}
&\int_{E_1}^{E_1+\Delta E} dE\ DOS(E) \sim \Delta E\ DOS(E_1) \\
&\quad = 2 \sum_{\boldsymbol{k}\in BZ,\lambda} \int_{E_1}^{E_1+\Delta E} dE\ \delta\left(E - E_\lambda(\boldsymbol{k})\right) \\
\Leftrightarrow &\frac{DOS(E_1)}{N_1 N_2} = \frac{2}{N_1 N_2 \Delta E} \sum_{\boldsymbol{k}\in BZ,\lambda} \int_{E_1}^{E_1+\Delta E} dE\ \delta\left(E - E_\lambda(\boldsymbol{k})\right). \qquad \text{(A.5)}
\end{aligned}$$

On the left hand side, we recognize the DOS per unit cell. The right hand side clarifies the numerical computation in order. We observe that it is normalized: the dimension we set for our physical system is arbitrary and only defines the precision we want in our momentum discretization. Ultimately, we just need to choose the range of energies we are interested in and a step ΔE to cover it; this will yield an histogram-like type of graphics.

A.2 Carrier density

Typically, we are interested in testing physical properties varying the Fermi level[1]. Experimentally, this is achieved by doping the material with electrons or holes. The parameter that is well defined in experimental results is the carrier density, n, which we define as positive for electrons and negative for holes. It is therefore useful to find a systematic way to relate the Fermi level, μ, with the carrier density, n, from an arbitrary electronic spectrum.

We stick to graphene-composed materials, for which we define the reference Fermi level, μ_0, as the energy corresponding to the half-filling situation. We now explain the numerical method. Let us start, without loss of generality, by the case where the system is doped with electrons. If we want to reach some Fermi level $\mu > \mu_0$, we have to count the number of states than can be occupied by electrons with energy smaller than μ. Given the electronic spectrum $E_\lambda(\boldsymbol{k})$, and taking into account the spin degeneracy, we have

$$N_e(\mu) = 2 \sum_{\boldsymbol{k}\in BZ,\lambda} \Theta(\mu - E_\lambda(\boldsymbol{k})), \qquad \text{(A.6)}$$

where Θ is the Heaviside step function. We now subtract the number of electrons in the half-filling situation, obtaining the effective number of electrons that we need for the doping:

$$\begin{aligned}
N_e(\mu) - N_e^{h.f.} &= 2 \sum_{\boldsymbol{k}\in BZ,\lambda} \Theta(\mu - E_\lambda(\boldsymbol{k})) - 2 \sum_{\boldsymbol{k}\in BZ,\lambda} \Theta(\mu_0 - E_\lambda(\boldsymbol{k})) \\
&= 2 \sum_{\substack{\boldsymbol{k}\in BZ,\\ \lambda\geq dim/2}} \Theta(\mu - E_\lambda(\boldsymbol{k})). \qquad \text{(A.7)}
\end{aligned}$$

Here, *dim* is the dimension of our system's Hamiltonian (which corresponds to the number of bands) and

---

[1] In a band structure picture, Fermi level is the term used to describe the top of the collection of electron energy levels at absolute zero temperature. Due to Pauli's exclusion principle, we cannot have two electrons in the same state, so we pack them into the lowest available energy states and build up a Fermi sea. The Fermi level is its surface and this concept is very important because the electrons near it are the major contributors for most physical properties.

the restriction $\lambda \geq dim/2$ implies that we sum over bands that are empty in the half-filling situation (we are labeling the bands as $\lambda = 0, 1, ..., dim - 1$, by increasing order of energy). Finally, for finite systems, we use again PBC and obtain

$$\begin{aligned} n(\mu > \mu_0) &= \frac{N_e(\mu) - N_e^{h.f.}}{A_{total}} = \frac{N_e(\mu) - N_e^{h.f.}}{N_1 N_2 A_{u.c.}} \\ &= \frac{2}{N_1 N_2 A_{u.c.}} \sum_{\substack{\boldsymbol{k} \in BZ, \\ \lambda \geq dim/2}} \Theta(\mu - E_\lambda(\boldsymbol{k})), \end{aligned} \tag{A.8}$$

where

$$A_{total} = N_1 N_2 A_{u.c.} \tag{A.9}$$

is the total area of the system and $A_{u.c.}$ the area of a unit cell. The deduction for systems doped with holes is straigthforward and leads to

$$n(\mu < \mu_0) = -\frac{2}{N_1 N_2 A_{u.c.}} \sum_{\substack{\boldsymbol{k} \in BZ, \\ \lambda < dim/2}} \Theta(E_\lambda(\boldsymbol{k}) - \mu). \tag{A.10}$$

Again, we notice that these expressions are normalized.

Appendix B

Method to derive effective Hamiltonians

We start by deriving the Dyson equation for the Green's functions of a quantum system. Let us consider a general Hamiltonian H, which we split into two parts,

$$H = H_0 + V. \tag{B.1}$$

We define $g(E)$ and $G(E)$ as Green's functions for H_0 and H, respectively:

$$(E - H_0)g(E) = 1 \Leftrightarrow g(E) = (E - H_0)^{-1}, \tag{B.2}$$

$$(E - H)G(E) = 1 \Leftrightarrow G(E) = (E - H)^{-1}. \tag{B.3}$$

Here, we stress that $g(E)$ and $G(E)$ are matrices with the same dimension of H_0 and H, and not column vectors. Then, we use the identity $E - H_0 = (E - H_0 - V) + V$ and apply $g(E)$ to the left and $G(E)$ to the right, obtaining the Dyson equation,

$$G(E) = g(E) + g(E)VG(E). \tag{B.4}$$

We now write

$$H = \begin{bmatrix} H_{AA} & H_{AB} \\ H_{BA} & H_{BB} \end{bmatrix}, \tag{B.5}$$

and split it such that

$$H_0 = \begin{bmatrix} H_{AA} & 0 \\ 0 & H_{BB} \end{bmatrix}, \quad V = \begin{bmatrix} 0 & H_{AB} \\ H_{BA} & 0 \end{bmatrix}. \tag{B.6}$$

The Dyson equation thus reads

$$\begin{bmatrix} G_{AA} & G_{AB} \\ G_{BA} & G_{BB} \end{bmatrix} = \begin{bmatrix} g_{AA} & 0 \\ 0 & g_{BB} \end{bmatrix} + \begin{bmatrix} g_{AA} & 0 \\ 0 & g_{BB} \end{bmatrix} \begin{bmatrix} 0 & H_{AB} \\ H_{BA} & 0 \end{bmatrix} \begin{bmatrix} G_{AA} & G_{BB} \\ G_{BA} & G_{BB} \end{bmatrix}, \tag{B.7}$$

where

$$G(E) = \begin{bmatrix} G_{AA} & G_{BB} \\ G_{BA} & G_{BB} \end{bmatrix}, \tag{B.8}$$

and

$$g(E) = \begin{bmatrix} g_{AA} & g_{BB} \\ g_{BA} & g_{BB} \end{bmatrix} = \begin{bmatrix} g_{AA} & 0 \\ 0 & g_{BB} \end{bmatrix} = \begin{bmatrix} (E - H_{AA})^{-1} & 0 \\ 0 & (E - H_{BB})^{-1} \end{bmatrix}, \tag{B.9}$$

given that H_0 is diagonal. From (B.7), we get

$$G_{AA} = g_{AA} + g_{AA} H_{AB} G_{BA}, \tag{B.10}$$

$$G_{BA} = g_{BB} H_{BA} G_{AA}, \tag{B.11}$$

and, therefore,

$$\begin{aligned} & G_{AA} = g_{AA} + g_{AA} H_{AB} g_{BB} H_{BA} G_{AA} \\ \Leftrightarrow\ & (1 - g_{AA} H_{AB} g_{BB} H_{BA}) G_{AA} = g_{AA} \\ \Leftrightarrow\ & G_{AA} = (1 - g_{AA} H_{AB} g_{BB} H_{BA})^{-1} g_{AA} \\ & \qquad = \left[g_{AA}^{-1}(1 - g_{AA} H_{AB} g_{BB} H_{BA})\right]^{-1} \\ & \qquad = \left[E - H_{AA} - H_{AB}(E - H_{BB})^{-1} H_{BA}\right]^{-1}. \end{aligned} \tag{B.12}$$

Finally, we interpret (B.12) by saying that G_{AA} is determined by an effective Hamiltonian in its subspace,

$$H_{AA}^{eff} = H_{AA} + H_{AB}(E - H_{BB})^{-1} H_{BA}. \tag{B.13}$$

Appendix C

Perturbation theory in the interaction picture

C.1 Time evolution in the Schrödinger representation

Let us consider a Hamiltonian $H_S(t) = H_{0,S} + V_S(t)$ (written in the Schrödinger representation) where all the time dependency is put into the potential $V_S(t)$. In the Schrödinger representation, all the dynamics is contained in the wave functions and is determined by the Schrödinger equation,

$$i\hbar\frac{\partial}{\partial t}\left|\psi(t)\right\rangle_S = H_S(t)\left|\psi(t)\right\rangle_S . \tag{C.1}$$

The solution for the time evolution can be written as

$$\left|\psi(t)\right\rangle_S = U(t,t_0)\left|\psi(t_0)\right\rangle_S , \tag{C.2}$$

where U is a unitary operator satisfying

$$i\hbar\frac{\partial U(t)}{\partial t} = H_S(t)U(t). \tag{C.3}$$

If our Hamiltonian is time independent, $H_S(t) = H_{0,S}$, we trivially obtain

$$U(t,t_0) = e^{-\frac{i}{\hbar}H_{0,S}(t-t_0)}. \tag{C.4}$$

When it is not, we obtain a self-consistent solution,

$$U(t,t_0) = 1 - \frac{i}{\hbar}\int_{t_0}^{t} dt' H_S(t')U(t',t_0), \tag{C.5}$$

which we can iterate to obtain

$$
\begin{aligned}
U(t,t_0) &= 1+\sum_{n=1}^{+\infty}\left(-\frac{i}{\hbar}\right)^n \int_{t_0}^{t} dt_1 \int_{t_0}^{t_1} dt_2 \;...\; \int_{t_0}^{t_{n-1}} dt_n H_S(t_1)H_S(t_2)...H_S(t_n) && \text{(C.6)}\\
&= \mathcal{T}\left\{e^{\frac{-i}{\hbar}\int_{t_0}^{t} dt' H_S(t')}\right\}, && \text{(C.7)}
\end{aligned}
$$

where $\mathcal{T}$ is the time-ordering operator. Looking at the right hand side of eq. (C.6), we observe that, even if we argue that our perturbation $V_S(t)$ is small, we cannot truncate the infinite sum. This is the motivation to introduce the interaction picture.

C.2 Time evolution in the interaction representation

In the interaction picture, we define

$$
|\psi(t)\rangle_I = e^{\frac{i}{\hbar}H_{0,S}(t-t_0)}\,|\psi(t)\rangle_S\,, \tag{C.8}
$$

which, according to Schrödinger's equation (C.1), satisfies

$$
i\hbar\frac{\partial}{\partial t}\,|\psi(t)\rangle_I = V_I(t)\,|\psi(t)\rangle_I\,, \tag{C.9}
$$

where the potential in the interaction representation is introduced as

$$
V_I(t) = e^{\frac{i}{\hbar}H_{0,S}(t-t_0)}V_S(t)e^{-\frac{i}{\hbar}H_{0,S}(t-t_0)}. \tag{C.10}
$$

Similarly to what we did before, we write the solution for the time evolution as

$$
|\psi(t)\rangle_I = U_I(t,t_0)\,|\psi(t_0)\rangle_I\,, \tag{C.11}
$$

where U_I is a unitary operator that satisfies

$$
i\hbar\frac{\partial U_I(t)}{\partial t} = V_I(t)U_I(t). \tag{C.12}
$$

Solving recursively, we obtain

$$
\begin{aligned}
U_I(t,t_0) &= 1+\sum_{n=1}^{+\infty}\left(-\frac{i}{\hbar}\right)^n \int_{t_0}^{t} dt_1 \int_{t_0}^{t_1} dt_2 \;...\; \int_{t_0}^{t_{n-1}} dt_n V_I(t_1)V_I(t_2)...V_I(t_n) && \text{(C.13)}\\
&= \mathcal{T}\left\{e^{\frac{-i}{\hbar}\int_{t_0}^{t} dt' V_I(t')}\right\}, && \text{(C.14)}
\end{aligned}
$$

which we can now truncate if $V_I(t)$ is small.

C.3 Average values in the interaction picture

By definition, the average value of an operator O must not depend on the representation. This can be trivially confirmed for the previous representations:

$$\langle\psi_S(t)|O_S|\psi_S(t)\rangle = \langle\psi_I(t)|O_I|\psi_I(t)\rangle\,. \tag{C.15}$$

Taking use of the Dyson equation (C.13), we can show that the average values in the interaction picture read

$$\begin{aligned}
\langle\psi_I(t)|O_I|\psi_I(t)\rangle = &\,\langle\psi_I(t_0)|O_I|\psi_I(t_0)\rangle + \\
&+\left(-\frac{i}{\hbar}\right)\int_{t_0}^{t} dt_1\,\langle\psi_I(t_0)|\left[O_I, V_I(t_1)\right]|\psi_I(t_0)\rangle + \\
&+\left(-\frac{i}{\hbar}\right)^2\int_{t_0}^{t} dt_1\int_{t_0}^{t_1} dt_2\,\langle\psi_I(t_0)|\left[\left[O_I, V_I(t_1)\right], V_I(t_2)\right]|\psi_I(t_0)\rangle + \\
&+\left(-\frac{i}{\hbar}\right)^3\int_{t_0}^{t} dt_1\int_{t_0}^{t_1} dt_2\int_{t_0}^{t_2} dt_3\,\langle\psi_I(t_0)|\left[\left[\left[O_I, V_I(t_1)\right], V_I(t_2)\right], V_I(t_3)\right]|\psi_I(t_0)\rangle + \\
&+\ldots\quad ,
\end{aligned} \tag{C.16}$$

where $[A, B] = AB - BA$ are commutators.

Appendix D

Fourier transform of the Coulomb potential

D.1 In 2 dimensions

Given the Coulomb potential in 2 dimensions,

$$v(\boldsymbol{r}) = \frac{e^2}{4\pi\varepsilon_r\varepsilon_0|\boldsymbol{r}|}, \quad \boldsymbol{r} \in \mathbb{R}^2, \tag{D.1}$$

we want to determine its FT, $v(\boldsymbol{q})$, which is given by

$$v(\boldsymbol{q}) = \int_{\mathbb{R}^2} d\boldsymbol{r}\ v(\boldsymbol{r})e^{-i\boldsymbol{q}.\boldsymbol{r}}. \tag{D.2}$$

We obtain

$$\begin{aligned} v(\boldsymbol{q}) &= \frac{e^2}{4\pi\varepsilon_r\varepsilon_0}\int_{\mathbb{R}^2} d\boldsymbol{r}\ \frac{e^{-i\boldsymbol{q}.\boldsymbol{r}}}{|\boldsymbol{r}|} \\ &= \frac{e^2}{4\pi\varepsilon_r\varepsilon_0}\int_0^{+\infty} dr\ r \int_0^{2\pi} d\theta\ \frac{e^{-iqr\cos{(\theta)}}}{r} \\ &= \frac{e^2}{2\pi\varepsilon_r\varepsilon_0 q}\int_0^{+\infty} dx \int_0^{\pi} d\theta\ e^{-ix\cos{(\theta)}} = v(q). \end{aligned} \tag{D.3}$$

Using the Jacobi-Anger expansion,

$$e^{ix\cos{(\theta)}} = J_0(x) + 2\sum_{n=1}^{+\infty} i^n J_n(x)\cos{(n\theta)}, \tag{D.4}$$

where $J_n(x)$ ($n \in \mathbb{N}_0$) is a Bessel function of the first kind, we can trivially compute the integration in θ,

$$\int_0^{\pi} d\theta\ e^{-ix\cos{(\theta)}} = \int_0^{\pi} d\theta\ e^{ix\cos{(\theta)}} = \pi J_0(x), \tag{D.5}$$

where we used that $\int_0^\pi d\theta\ \cos(n\theta) = 0$. Since Bessel functions are normalized, $\int_0^{+\infty} dx\ J_n(x) = 1$, we obtain the final result

$$v(\boldsymbol{q}) = v(q) = \frac{e^2}{2\varepsilon_r\varepsilon_0 q}. \tag{D.6}$$

D.2 Between two parallel planes

Let us now consider the Coulomb potential between two electrons in two different parallel planes separated by $d_\perp$. In this case, it is written as

$$v(\boldsymbol{r}) = \frac{e^2}{4\pi\varepsilon_r\varepsilon_0\sqrt{r^2 + d_\perp^2}}, \quad \boldsymbol{r} \in \mathbb{R}^2. \tag{D.7}$$

The FT reads

$$\begin{aligned} v(\boldsymbol{q}) &= \frac{e^2}{4\pi\varepsilon_r\varepsilon_0}\int_0^{+\infty} dr\ r \int_0^{2\pi} d\theta\ \frac{e^{-iqr\cos(\theta)}}{\sqrt{r^2 + d_\perp^2}} \\ &= \frac{e^2}{2\pi\varepsilon_r\varepsilon_0 q}\int_0^{+\infty} dx\ x \int_0^{\pi} d\theta\ \frac{e^{-ix\cos(\theta)}}{\sqrt{x^2 + (qd_\perp)^2}} \\ &= \frac{e^2}{2\varepsilon_r\varepsilon_0 q}\int_0^{+\infty} dx\ \frac{xJ_0(x)}{\sqrt{r^2 + (qd_\perp)^2}}. \end{aligned} \tag{D.8}$$

Using the property $\int_0^{+\infty} dx\ \frac{xJ_0(x)}{\sqrt{x^2+a^2}} = e^{-|a|}$, we get

$$v(\boldsymbol{q}) = v(q) = \frac{e^2}{2\varepsilon_r\varepsilon_0 q}e^{-qd_\perp}. \tag{D.9}$$

Appendix E

Gibbs-Bogoliubov inequality

In this appendix, we prove the Gibbs-Bogoliubov inequality,

$$F \leq F_{MF} + \langle H - H_{MF} \rangle_{MF} \,, \tag{E.1}$$

in which F represents the free energy of the system (described by the Hamiltonian $H = H_{MF} + \Delta H$) and F_{MF} the free energy of the system in MF (described by H_{MF}). The proof of this inequality can be accomplished by first proving the following theorem, from which (E.1) is obtained as a corollary.

Theorem

The generalized free energy functional, defined as [65]

$$\Omega[\hat{\rho}] = \mathrm{Tr}\left\{\hat{\rho}\left[\hat{H} - \mu\hat{N} + k_B T \log\left(\hat{\rho}\right)\right]\right\}, \tag{E.2}$$

(i) has an absolute minimum for the grand canonical distribution, i.e., when $\hat{\rho} = \hat{\rho}_G = \frac{e^{-\beta(\hat{H}-\mu\hat{N})}}{\Theta(T,\mu)}$, where $1/\beta = k_B T$ and $\Theta(T,\mu) = \mathrm{Tr}\left\{e^{-\beta(\hat{H}-\mu\hat{N})}\right\}$.

(ii) the minimum coincides with the grand potential of the system, $\Omega_S(T,\mu) = -k_B T \log[\Theta(T,\mu)]$.

Proof

We define $\hat{\omega}$ and $\hat{\omega}_G$ such that

$$\hat{\rho} = e^{-\hat{\omega}}, \quad \hat{\rho}_G = e^{-\hat{\omega}_G} \Rightarrow \hat{\omega}_G = \beta(\hat{H} - \mu\hat{N}) + \log(\Theta) = \beta(\hat{H} - \mu\hat{N} - \Omega_S). \tag{E.3}$$

Then, using that $\mathrm{Tr}\left\{\hat{\rho}\right\} = \mathrm{Tr}\left\{e^{-\hat{\omega}}\right\} = 1$, we can write

$$\begin{aligned} &\beta\Omega[\hat{\rho}] = \mathrm{Tr}\left\{e^{-\hat{\omega}}\left(\hat{\omega}_G + \beta\Omega_S - \hat{\omega}\right)\right\} \\ \Leftrightarrow &\beta\Omega[\hat{\rho}] - \beta\Omega_S(T,\mu) = \mathrm{Tr}\left\{e^{-\hat{\omega}}\left(\hat{\omega}_G - \hat{\omega}\right)\right\}, \end{aligned} \tag{E.4}$$

from which the part (ii) of the theorem immediately follows:

$$\hat{\rho} = \hat{\rho}_G \Rightarrow \hat{\omega} = \hat{\omega}_G \Rightarrow \Omega[\hat{\rho}_G] = \Omega_S(T, \mu). \tag{E.5}$$

In order to prove part (i), we define two Hilbert spaces, $\{|\psi_j\rangle\}$ and $\{|\phi_k\rangle\}$ such that

$$\hat{\omega} |\psi_j\rangle = \omega_j |\psi_j\rangle , \quad \hat{\omega}_G |\phi_k\rangle = \omega_k^{(G)} |\phi_k\rangle . \tag{E.6}$$

We also define the positive quantity, $c_{kj} = |\langle\phi_k|\psi_j\rangle|^2 \geq 0$. From eq. (E.4), and making use of the closure relation, $\sum_k |\phi_k\rangle\langle\phi_k| = 1$, we can write

$$\begin{aligned} \beta\Omega[\hat{\rho}] - \beta\Omega_S(T, \mu) &= \sum_j \langle\psi_j|e^{-\hat{\omega}}(\hat{\omega}_G - \hat{\omega})|\psi_j\rangle \\ &= \sum_j e^{-\omega_j} \left(\langle\psi_j|\hat{\omega}_G|\psi_j\rangle - \omega_j\right) \\ &= \sum_j e^{-\omega_j} \left(\sum_k c_{kj}\omega_k^{(G)} - \omega_j\right) \\ &= \sum_{j,k} c_{kj} e^{-\omega_j} \left(\omega_k^{(G)} - \omega_j\right) , \end{aligned} \tag{E.7}$$

where, in the last step, we have used the propriety $\sum_k c_{kj} = 1$. Now, we rewrite the (trivial) indentity, $\mathrm{Tr}\{\hat{\rho}\} = \mathrm{Tr}\{\hat{\rho}_G\} = 1$, in the following convenient manner:

$$\begin{aligned} \mathrm{Tr}\{\hat{\rho}_G\} - \mathrm{Tr}\{\hat{\rho}\} = 0 = \mathrm{Tr}\left\{e^{-\hat{\omega}_G}\right\} - \mathrm{Tr}\left\{e^{-\hat{\omega}}\right\} &= \sum_j \langle\psi_j|e^{-\hat{\omega}_G}|\psi_j\rangle - \sum_j \langle\psi_j|e^{-\hat{\omega}}|\psi_j\rangle \\ &= \sum_{j,k} c_{kj} e^{-\omega_k^{(G)}} - \sum_j e^{-\omega_j} \\ &= \sum_{j,k} c_{kj} \left(e^{-\omega_k^{(G)}} - e^{-\omega_j}\right) \\ &= \sum_{j,k} c_{kj} e^{-\omega_j} \left(e^{\omega_j - \omega_k^{(G)}} - 1\right) . \end{aligned} \tag{E.8}$$

Adding this last zero quantity to (E.7), we get

$$\beta\Omega[\hat{\rho}] - \beta\Omega_S(T, \mu) = \sum_{j,k} c_{kj} e^{-\omega_j} \left(e^{\omega_j - \omega_k^{(G)}} - 1 + \omega_k^{(G)} - \omega_j\right) . \tag{E.9}$$

Since $c_{kj} \geq 0$ and $e^{-\omega_j} > 0$, it remains to show that $e^{\omega_j - \omega_k^{(G)}} - 1 + \omega_k^{(G)} - \omega_j \geq 0$ to prove the part (i) of the theorem. This last task is trivial. We define

$$f(x) = e^x - (x + 1), \tag{E.10}$$

with $x = \omega_j - \omega_k^{(G)}$ and show that $f(x) \geq 0$. Since $f'(x) = e^x - 1$, for which the only zero is at $x = 0$ (where $f(0) = 0$), and $f''(x) = e^x > 0$, we readily see that $f(x) \geq 0, \forall x \in \mathbb{R}$. We have therefore proved that

$$\Omega[\hat{\rho}] \geq \Omega_S(T, \mu), \tag{E.11}$$

being equal only when $\hat{\rho} = \hat{\rho}_G$.

Corollary

Let H_{MF} be a simplified version of the Hamiltonian H, characterized by the distribution

$$\hat{\rho}_{MF} = \frac{e^{-\beta(\hat{H}_{MF} - \mu\hat{N})}}{\Theta_{MF}(T, \mu)}, \quad \Theta_{MF}(T, \mu) = \mathrm{Tr}\,\{e^{-\beta(\hat{H}_{MF} - \mu\hat{N})}\}. \tag{E.12}$$

Using the theorem, we may write

$$\begin{aligned} \Omega_S(T, \mu) \leq \Omega[\hat{\rho}_{MF}] &= \mathrm{Tr}\left\{\hat{\rho}_{MF}\left[\hat{H} - \mu\hat{N} + k_B T \log\left(\hat{\rho}_{MF}\right)\right]\right\} \\ &= \mathrm{Tr}\left\{\hat{\rho}_{MF}\left[\hat{H} - \hat{H}_{MF} - k_B T \log\left(\Theta_{MF}\right)\right]\right\} \\ &= \Omega_{S,MF}(T, \mu) + \langle \hat{H} - \hat{H}_{MF} \rangle_{MF}\,, \end{aligned} \tag{E.13}$$

where $\Omega_{S,MF}(T, \mu) = -k_B T \log\left(\Theta_{MF}\right)$ is the grand potential of the system in MF.